ROLES OF ALUMINATE SPINEL SUPPORT ON COPPER BASED CATALYST FOR HYDROGENOLYSIS OF GLYCEROL TO 1,2 PROPANEDIOL

By
MISS Charuwan POOSRI

A Thesis Submitted in Partial Fulfillment of the Requirements
for Doctor of Engineering (CHEMICAL ENGINEERING)
Department of CHEMICAL ENGINEERING
Graduate School, Silpakorn University
Academic Year 2019
Copyright of Graduate School, Silpakorn University

บทบาทของตัวรองรับอะลูมิเนตสปิเนลในตัวเร่งปฏิกิริยาทองแดงสำหรับปฏิกิริยาไฮโดรจีโนลิซิสของกลีเซอรอลไปเป็น 1, 2 โพรเพนไดออล

โดย

นางสาวจารุวรรณ ภูศรี

วิทยานิพนธ์นี้เป็นส่วนหนึ่งของการศึกษาตามหลักสูตรวิศวกรรมศาสตรดุษฎีบัณฑิต

สาขาวิชาวิศวกรรมเคมี แบบ 1.1 ระดับปริญญาดุษฎีบัณฑิต

ภาควิชาวิศวกรรมเคมี

บัณฑิตวิทยาลัย มหาวิทยาลัยศิลปากร

ปีการศึกษา 2562

ลิขสิทธิ์ของบัณฑิตวิทยาลัย มหาวิทยาลัยศิลปากร

ROLES OF ALUMINATE SPINEL SUPPORT ON COPPER BASED CATALYST FOR HYDROGENOLYSIS OF GLYCEROL TO 1,2 PROPANEDIOL

By

MISS Charuwan POOSRI

A Thesis Submitted in Partial Fulfillment of the Requirements
for Doctor of Engineering (CHEMICAL ENGINEERING)
Department of CHEMICAL ENGINEERING
Graduate School, Silpakorn University
Academic Year 2019
Copyright of Graduate School, Silpakorn University

Title	Roles of aluminate spinel support on copper based catalyst for hydrogenolysis of glycerol to 1,2 propanediol
By	Charuwan POOSRI
Field of Study	(CHEMICAL ENGINEERING)
Advisor	Choowong Chaisuk

Graduate School Silpakorn University in Partial Fulfillment of the Requirements for the Doctor of Engineering

.....Dean of graduate school
(Associate Professor Jurairat Nunthanid, Ph.D.)

Approved by

.....Chair person
(Assistant Professor Okorn Mekasuwandumrong , D.Eng.)

.....Advisor
(Assistant Professor Choowong Chaisuk , D.Eng.)

.....Committee
(Assistant Professor Worapon Kiatkitipong , D.Eng.)

.....Committee
(Assistant Professor Sirirat Wacharawichanant , D.Eng.)

.....External Examiner
(Dr. Kajornsak Faungnawakij , D.Eng.)

56404803 : Major (CHEMICAL ENGINEERING)
Keyword : Aluminate Spinel, Flame Spray Pyrolysis, Copper, Alumina, Glycerol Hydrogenolysis

MISS CHARUWAN POOSRI : ROLES OF ALUMINATE SPINEL SUPPORT ON COPPER BASED CATALYST FOR HYDROGENOLYSIS OF GLYCEROL TO 1,2 PROPANEDIOL THESIS ADVISOR : ASSISTANT PROFESSOR CHOOWONG CHAISUK, D.Eng.

In this work, we prepared aluminate spinel modified Al_2O_3 support on Cu based catalysts, which is various type of metal aluminate spinel (M= Cu, Zn, Fe and Co) and amount of metal incorporated with Al_2O_3 (10 to 40 wt.% of metal) were synthesized by flame spray pyrolysis (FSP). The catalysts were characterized using X-ray diffraction (XRD), N_2 physisorption, N_2O decomosition and temperature programmed reduction (TPR). The XRD results confirmed the crystal structure of copper aluminate ($CuAl_2O_4$), zinc aluminate ($ZnAl_2O_4$), iron aluminate ($FeAl_2O_4$), and cobalt aluminate ($CoAl_2O_4$) formation, The incorporation of copper, zinc iron or cobalt with aluminum precursor during FSP step can be inhibit growth of Al_2O_3 particles resulting in the increasing BET surface and smaller particle size than pure Al_2O_3 support. For catalytic performance of glycerol hydrogenolysis reaction, the Cu/Al_2O_3 catalysts have a copper content of 10 wt%, zinc and an iron content of 30 wt%, and a cobalt content of 40 wt % with alumina presented high activity and the improved selectivity to 1,2-propanediol. The appearance of metal aluminate spinel ($CuAl_2O_4$, $ZnAl_2O_4$, and $FeAl_2O_4$) on catalyst also relates to a high selectivity of 1,2-propanediol and the decreased decomposition of 1,2-propanediol to propanal. While the presence of $CoAl_2O_4$ promoted acetol production.

มหาวิทยาลัยศิลปากร

ACKNOWLEDGEMENTS

This work was supported by Department of Chemical Engineering, Faculty of Engineering and Industrial Technology, Silpakorn University and Graduate School for financial support. The authors would like to thank my advisor, Assistant Professor Dr. Choowong Chaisuk, for invaluable suggestions and knowledge. I would like to thank Assistant Professor Dr.Okorn Mekasuwandumrong for encouragement and friendship that we have received. Another would like to tank Dr. Kajornsak Faungnawakij (Director of Nanomaterials and Nanosystems Engineering Research Unit, National Nanotechnology Center), Assistant Professor Worapon Kiatkitipong, Assistant Professor Sirirat Wacharawichanant, who have been members of the committee.

In addition, I wish to thank my family, my friends, Ms. Wanwipa leangsiri and the member of chemical engineering laboratory at Silpakorn university, for the furtherance, financial support challenging atmosphere. Finally, I would like to thank Mr. Ekanun Loedphonganukun for release stress.

Charuwan POOSRI

มหาวิทยาลัยศิลปากร

TABLE OF CONTENTS

Page

ABSTRACT ..... D

ACKNOWLEDGEMENTS ..... E

TABLE OF CONTENTS ..... F

List of table I

List of figure ..... K

CHAPTER I 1

INTRODUCTION 1

1.1 Objectives of the Research 3

CHAPTER II 5

GLYCEROL HYDROGENOLYSIS TO 1,2 PROPANEDIOL 5

2.1 Process of glycerol hydrogenolysis 5

2.2 Glycerol hydrogenolysis to 1,2-PDO over Cu-based catalysts 9

CHAPTER III 14

FLAME SPRAY PYROLYSIS 14

CHAPTER IV 23

EXPERIMENTAL SECTION 23

4.1 Catalyst preparation 23

4.2 Catalyst characterization 25

4.3 Glycerol hydrogenolysis activity measurement 26

CHAPTER V 27

ROLE OF COPPER ALUMINATE SPINEL SUPPORT ON COPPER-BASED CATALYST FOR HYDROGENOLYSIS OF GLYCEROL TO 1,2 PROPANEDIOL 27

5.1 The physical properties of Cu inserted on copper-based catalysts 27

5.2 The chemical properties of Cu inserted on copper-based catalysts 32

5.3 Catalytic performance of Cu inserted on copper-based catalysts in glycerol hydrogenolysis 39
5.4 Conclusions 42
CHAPTER VI 43
ROLE OF ZINC ALUMINATE SPINEL SUPPORT ON COPPER-BASED CATALYST FOR HYDROGENOLYSIS OF GLYCEROL TO 1,2 PROPANEDIOL 43
6.1 The physical properties of Zn inserted on copper-based catalysts 43
6.2 The chemical properties of Zn inserted on copper-based catalysts 47
6.3 Catalytic performance of Zn inserted on copper-based catalysts 51
6.4 Conclusions 54
CHAPTER VII 55
ROLE OF IRON ALUMINATE SPINEL SUPPORT ON COPPER-BASED CATALYST FOR HYDROGENOLYSIS OF GLYCEROL TO 1,2 PROPANEDIOL 55
7.1 The physical properties of Fe inserted on copper-based catalysts 55
7.2 The chemical properties of Fe inserted on copper-based catalysts 60
7.3 Catalytic performance of Fe inserted on copper-based catalysts 64
7. 4 Conclusions 65
CHAPTER VIII 66
ROLE OF COBALT ALUMINATE SPINEL SUPPORT ON COPPER-BASED CATALYST FOR HYDROGENOLYSIS OF GLYCEROL TO 1,2 PROPANEDIOL 66
8.1 The physical properties of Co inserted on copper-based catalysts 66
8.2 The chemical properties of Co inserted on copper-based catalysts 71
8.3 Catalytic performance of Co inserted on copper-based catalysts 76
8.4 Conclusions 77
CHAPTER IX 78
COMPARISION OF METAL SPINEL SUPPORT ON COPPER-BASED CATALYSTS FOR GLYCEROL HYDROGENOLYSIS TO 1,2 PROPANEDIOL 78
CHAPTER X 82

SUMMARY.....82
REFERENCES 83
APPENDIXS.....93
VITA 110

List of table

Page

Table 1 The metal oxide support on performance of Cu-based catalyst. 12

Table 2 The chemicals used in the preparation of catalysts. 23

Table 3 The symbol of the catalysts. 24

Table 4 The crystalline size of copper oxide from XRD results. 29

Table 5 The BET surface area and total pore volume of catalyst. 32

Table 6 Results form H_2-TPR profiles. 35

Table 7 The crystalline size of copper oxide on the FSP-made Zn-Al_2O_3 from XRD results. 45

Table 8 The BET surface area and total pore volume of catalyst. 47

Table 9 The crystalline size of copper oxide on the FSP-made Fe-Al_2O_3 from XRD results. 57

Table 10 The BET surface area and total pore volume of catalyst. 60

Table 11 The crystalline size of copper oxide on the FSP-made Co-Al_2O_3 from XRD results. 68

Table 12 The BET surface area and total pore volume of catalyst. 69

Table 13 XPS data for Co 2p, O 1s, and Al 2p of the xCo-Al_2O_3 (x=10, 20, 30, and 40 wt% Co). 74

Table 14 ICP data of metal (M-Al_2O_3, M= Cu, Zn, Fe, and Co). 98

Table 15 The activity and selectivity of the 30Cu/xCu-Al_2O_3 (x = 0, 10, 20, 30, and 40 wt% Cu). 102

Table 16 The activity and selectivity of the of the aCu/bCu-Al_2O_3 (a+b = 30 wt% Cu) catalyst. 103

Table 17 The activity and selectivity of the of the 30Cu/Al_2O_3 catalyst with different reaction time. 104

Table 18 The activity and selectivity of the 30Cu/xZn-Al_2O_3 (x = 0, 10, 20, 30, and 40 wt% Zn). 105

Table 19 The activity and selectivity of the 30Cu/30Zn-Al_2O_3 with different 106

Table 20 The activity and selectivity of the 30Cu/xFe-Al_2O_3 (x = 0, 10, 20, 30, and 40 wt% Fe). 107

Table 21 The activity and selectivity of the 30Cu/xCo-Al_2O_3 (x = 0, 10, 20, 30, and 40 wt% Co). 108

Table 22 The activity and selectivity of the 40Co-Al_2O_3 and 10Co/30Co-Al_2O_3 catalysts. 109

List of figure

Page

Figure 1 The Cu/Cu-Al_2O_3 catalysts.....4

Figure 2 The 30Cu/xM-Al_2O_3 catalysts.....4

Figure 3 Possible reaction of selective hydrogenolysis of glycerol (57).....6

Figure 4 Mechanism of glycerol dehydration on Lewis acid sites (64).....7

Figure 5 Mechanism of glycerol dehydration on Brønsted acid sites.....8

Figure 6 Glycerol hydrogenolysis pathway to 1, 2-propanediol (68).....9

Figure 7 Proposed reaction pathway for hydrogenolysis of glycerol to 1,2-propanediol with aqueous phase reforming over Cu–Ni/Al_2O_3 catalyst (72).....11

Figure 8 XRD patterns of samples after calcined at different temperatures and different ratio C_M : C_{cit} at calcined 800 °C : $CuAl_2O_4$ (●), CuO (◊), Al_2O_3 (■) (42)..13

Figure 9 Schematic of the FSP experimental set up and the particle formation process (83).....15

Figure 10 The XRD crystallite (d_{XRD}, □) , particle size from TEM (d_{TEM}, ●), and particle size from BET (d_{BET}, ○) as a function of cobalt loading (a) and precursor feed rate (b) (52).....16

Figure 11 (a) the specific surface areas and average particle sizes of silica particles produced from TEOS precursor as a function of various concentrations. TEM image of silica particles for (b) 0.1, (c) 0.3, and (d) 0.5 M (85).....17

Figure 12 (a) the specific surface areas and average particle sizes of silica particles produced from silicic acid precursor as a function of various concentrations. TEM image of silica particles for (b) 0.1, (c) 0.3, and (d) 0.5 M (85).....18

Figure 13 (a) SEM, (b,c) TEM and (d) HRTEM image of $CuFe_2O_4$ nanoaggregates (86). 19

Figure 14 Schematics of (a and b) two nozzle flame spray pyrolysis (2-FSP) and (c) one-nozzle flame spray pyrolysis (1-FSP) (87).....20

Figure 15 Schematic diagram of formation mechanism of core-shell structure $AgBaTiO_3$ composite powders in the flame spray pyrolysis.....21

Figure 16 TEM images of the pure $BaTiO_3$and $AgBaTiO_3$ composite powders prepared directly by flame spray pyrolysis.....21

Figure 17 (a) TEM image of nanorods made from zinc nitrate/ethanol precursor solutions (b) SEM image revealing the presence of tetrapods (circle) in the product powders, (c) TEM image of nanorods made from zinc nitrate/methanol precursor solutions (90). 22

Figure 18 Scheme of Flame spray pyrolysis.....23

Figure 19 The XRD pattern of the FSP-inserted Cu (xCu-Al_2O_3, x=0, 10, 20, 30, and 40 wt% Cu). 28

Figure 20 The XRD pattern of 30Cu/xCu-Al_2O_3 (x = 0, 10, 20, 30, and 40 wt% Cu) catalyst. 29

Figure 21 The N_2 adsorption/desorption isotherms: (a) the FSP-made xCu-Al_2O_3, (x = 0, 10, 20, 30, and 40 wt% Cu), (b) 30Cu/xCu-Al_2O_3 (x = 0, 10, 20, 30, and 40 wt% Cu) catalyst. 31

Figure 22 H_2-TPR patterns of the copper oxide bulk. 33

Figure 23 H_2-TPR patterns of the FSP-made xCu-Al_2O_3, (x = 0, 10, 20, 30, and 40 wt% Cu). 34

Figure 24 H_2-TPR patterns of the 30Cu/xCu-Al_2O_3 (x= 0, 10, 20, 30, and 40 wt%.36

Figure 25 TPR patterns of the 30Cu/xCu-Al_2O_3 (x= 0, 10, 20, 30, and 40 wt% Cu) at temperature in a range 400 to 800 ºC.....36

Figure 26 Comparison of the TPR profiles of fresh and pretreated catalyst in H_2, 300 ºC, 3 h for 30Cu/40Cu-Al_2O_3 catalyst. 38

Figure 27 (a) N_2O decomposition results of 30Cu/xCu-Al_2O_3 (x = 0, 10, 20, 30, and 40 wt%), (b) crystallite size of CuO of 30Cu/xCu-Al_2O_3 (x = 0, 10, 20, 30, and 40 wt%). 39

Figure 28 The activity and selectivity of the 30Cu/xCu-Al_2O_3, (x= 0, 10, 20, 30, and 40 wt% Cu) catalyst. 41

Figure 29 The activity and selectivity of the aCu/bCu-Al_2O_3 (a+b = 30 wt% Cu) catalyst. 41

Figure 30 The XRD pattern of the FSP-inserted Zn (xZn-Al_2O_3, x = 0, 10, 20, 30, and 40 wt% Zn).....44

Figure 31 The XRD pattern of 30Cu/xZn-Al_2O_3 (x = 0, 10, 20, 30, and 40 wt% Zn) catalyst. 44

Figure 32 The N_2 adsorption/desorption isotherms: (a) the FSP-made xZn-Al_2O_3, (x = 0, 10, 20, 30, and 40 wt% Zn), (b) 30Cu/xZn-Al_2O_3 (x = 0, 10, 20, 30, and 40 wt% Zn) catalyst.....46

Figure 33 H_2-TPR patterns of the copper oxide and zinc oxide bulk. 48

Figure 34 H_2-TPR patterns of the 30Cu/xZn-Al_2O_3 (x= 0, 10, 20, 30, and 40 wt% Zn) catalyst.....48

Figure 35 Total reducibility of 30Cu/xZn-Al_2O_3 (x = 0, 10, 20, 30, and 40 wt% Zn) catalyst. 49

Figure 36 (a) N_2O decomposition results of 30Cu/xZn-Al_2O_3 (x = 0, 10, 20, 30, and 40 wt% Zn), (b) diameter of copper metallic size of 30Cu/xZn-Al_2O_3 (x = 0, 10, 20, 30, and 40 wt% Zn) catalyst. 50

Figure 37 The activity and selectivity of the 30Cu/xZn-Al_2O_3, (x= 0, 10, 20, 30, and 40 wt% Zn) catalyst. 52

Figure 38 Effect of reaction time during the glycerol hydrogenolysis on 30Cu/30Zn-Al_2O_3 catalyst. 53

Figure 39 Effect of reaction time during the glycerol hydrogenolysis on 30Cu/Al_2O_3 catalyst. 54

Figure 40 The XRD pattern of the FSP-inserted Fe (xFe-Al_2O_3, x = 0, 10, 20, 30, and 40 wt% Fe). 56

Figure 41 The XRD pattern of 30Cu/xFe-Al_2O_3 (x = 0, 10, 20, 30, and 40 wt% Fe) catalyst. 57

Figure 42 The N_2 adsorption/desorption isotherms: (a) the FSP-made xFe-Al_2O_3, (x = 0, 10, 20, 30, and 40 wt% Fe), (b) 30Cu/xFe-Al_2O_3 (x = 0, 10, 20, 30, and 40 wt% Fe) catalyst. 59

Figure 43 H_2-TPR patterns of the iron oxide and copper oxide bulk 61

Figure 44 H_2-TPR patterns of the FSP-made xFe-Al_2O_3 (x= 0, 10, 20, 30, and 40 wt% Fe). 62

Figure 45 H_2-TPR patterns of the 30Cu/xFe-Al_2O_3 (x= 0, 10, 20, 30, and 40 wt% Fe) catalysts. 63

Figure 46 N_2O decomposition results of 30Cu/xFe-Al_2O_3 (x = 0, 10, 20, 30, and 40 wt% Fe). 64

Figure 47 The activity and selectivity of the 30Cu/xFe-Al_2O_3, (x= 0, 10, 20, 30, and 40 wt% Fe) catalyst.....65

Figure 48 The XRD pattern of the FSP-inserted Co (xCo-Al_2O_3, x = 0, 10, 20, 30, and 40 wt% Co). 67

Figure 49 The XRD pattern of 30Cu/xCo-Al_2O_3 (x = 0, 10, 20, 30, and 40 wt% Co) catalyst. 67

Figure 50 The N_2 adsorption/desorption isotherms: (a) the FSP-made xCo-Al_2O_3, (x = 0, 10, 20, 30, and 40 wt% Co), (b) 30Cu/xCo-Al_2O_3 (x = 0, 10, 20, 30, and 40 wt% Co) catalyst. 70

Figure 51 H_2-TPR patterns of the copper oxide and cobalt oxide bulk. 71

Figure 52 H_2-TPR patterns of the xCo-Al_2O_3 (x= 0, 10, 20, 30, and 40 wt% Co). ..72

Figure 53 H_2-TPR patterns of the 30Cu/xCo-Al_2O_3 (x= 0, 10, 20, 30, and 40 wt% Co) catalysts. 73

Figure 54 XPS spectra of Co 2p of the xCo-Al_2O_3 (x=10, 20, 30, and 40 wt%).....75

Figure 55 (a) N_2O chemisorption results of 30Cu/xCo-Al_2O_3 (x = 0, 10, 20, 30, and 40 wt% Co), (b) diameter of copper metallic size of 30Cu/xCo-Al_2O_3 (x = 0, 10, 20, 30, and 40 wt% Co) catalyst 76

Figure 56 The activity and selectivity of the 30Cu/xCo-Al_2O_3, (x= 0, 10, 20, 30, and 40 wt% Co). 77

Figure 57 The activity and selectivity of 30Cu/10M-Al_2O_3, (M= Cu, Zn, Fe and Co). 79

Figure 58 The activity and selectivity of 30Cu/20M-Al_2O_3, (M= Cu, Zn, Fe and Co). 80

Figure 59 The activity and selectivity of 30Cu/30M-Al_2O_3, (M= Cu, Zn, Fe and Co). 80

Figure 60 The activity and selectivity of 30Cu/40M-Al_2O_3, (M= Cu, Zn, Fe and Co) 81

Figure 61 The half-height width of CuO at 48.804º of 40Cu-Al_2O_3 sample. 94

Figure 62 TPR pattern of xCu-Al_2O_3 and 30Cu/xCu-Al_2O_3 (x = 10, 20, 30, and 40 wt% Cu. 99

Figure 63 TPR pattern of xCo-Al_2O_3 and 30Cu/xCo-Al_2O_3 (x = 10, 20, 30, and 40 wt% Co). 99

Figure 64 TPR pattern of xFe-Al_2O_3 and 30Cu/xFe-Al_2O_3 (x = 10, 20, 30, and 40 wt% Fe). 100

Figure 65 TPR pattern of aCu/bCu-Al_2O_3 catalyst (a+b = 30 wt% Cu). 100

Figure 66 TPR pattern of 10Co/30Co-Al_2O_3 40Co-Al_2O_3 catalysts. 101

Figure 67 The activity and selectivity of the 30Cu/xCu-Al_2O_3 (x = 0, 10, 20, 30, and 40 wt% Cu). 102

Figure 68 The activity and selectivity of the aCu/bCu-Al_2O_3 (a+b = 30 wt% Cu) catalyst. 103

Figure 69 The activity and selectivity of the 30Cu/Al_2O_3 catalyst with different ..104

Figure 70 The activity and selectivity of the 30Cu/xZn-Al_2O_3 (x = 0, 10, 20, 30, and 40 wt% Zn). 105

Figure 71 The activity and selectivity of the 30Cu/30Zn-Al_2O_3 with different 106

Figure 72 The activity and selectivity of the 30Cu/xFe-Al_2O_3 (x = 0, 10, 20, 30, and 40 wt% Fe).....107

Figure 73 The activity and selectivity of the 30Cu/xCo-Al_2O_3 (x = 0, 10, 20, 30, and 40 wt% Co). 108

Figure 74 The activity and selectivity of the 40Co-Al_2O_3 and 10Co/30Co-Al_2O_3 catalysts. 109

มหาวิทยาลัยศิลปากร

CHAPTER I

INTRODUCTION

Biomass has been aiming as a renewable energy source for sustainable production of liquid fuels and chemical products due to the dwindling fossil fuel and concerning environmental. Biodiesel was one typical instance of biomass utilization that was commonly made from the transesterification of triglycerides in vegetable or waste oil. The biodiesel production in 2012 is 22.7 million metric tons and was estimated growing to 36.9 million metric tons in 2020 (1). Increasing of biodiesel production will generate a large amount of crude glycerol as side product (100 Kg of biodiesel produces 10 kg of crude glycerol), leading to plummet in the price of glycerol. Several catalytic processes can be upgraded glycerol into high-value product that oxidation, reduction, halogenated, etherification, esterification, and dehydration of glycerol for instance dihydroxyacetone (2-4) , glyceric acid (5-7), 1, 2-propanediol (8-11), glycerol carbonate (12-14) ,glyceryl ethers (15-17), and acrylic acid (18-20). One of the promising processes was glycerol hydrogenolysis to 1, 2-propanediol, also called propylene glycol because of its use as monomer of polyester resins, solvent in paints, cosmetics, and medicine etc. Presently, 1, 2-propanediol was mainly produced through hydrolysis of hazardous propylene oxide that is converted from oxidation of propylene, which its follow the route of petrochemical route (21). Thus, the production of 1, 2-propanediol from biomass-derived glycerol was encouraging processes that substitute for petroleum-derived, environmentally friendly, substantially improving the process economics.

Glycerol hydrogenolysis has been investigated over various metal catalysts as noble metal (Pt, Ru, Rh) (22-24) and transition metal group (Ni, Cu) (25-27). These catalysts are dispersed on metal oxide supported such as Al_2O_3 , SiO_2, TiO_2, ZrO_2 (22-24), (27-29). The activity and selectivity of reaction mainly depend on the environmental of process and nature of based-catalyst. Among of noble metals, Ru-based catalyst has been presented higher activity for the glycerol hydrogenolysis but low selectivity to 1, 2-propanediol. It was well known for higher ability of C-C bond cleavage, resulting in poor propanediol selectivity (29-31), when as Cu-based catalyst

often promoted C-O bond cleavage as a consequence excellent selectivity toward 1, 2-propanediol (26, 27, 32). Hence, the copper catalyst is interesting for glycerol hydrogenolysis reaction. The Cu-based catalyst have been widely studied over various supports like Al_2O_3 (33-35), SiO_2 (27, 36), ZnO (21, 37), ZrO_2 (10), TiO_2 (38) Cr_2O_3(39, 40). M.A. Dasari et al. reported that the Cu-Cr catalysts ($CuCr_2O_4$) shown good activity (55%) and high selectivity of 1, 2-propanediol (85%) under mild reaction conditions of 200° C and 200 psi hydrogen pressure for 24 h (39). Z. Xiao et al. also suggested that the Cu-Cr catalyst presented $CuCr_2O_4$ and Cr_2O_3 phases which showed better activity for glycerol catalytic conversion than those with Cu and Cr_2O_3 phases. However, there are concerns on health and environment due to the poison related to chromium content of such catalysts(41).

Recently, B. K. Kwak et al. investigated the use of Cu/Al_2O_3 catalysts that appeared copper aluminate spinel ($CuAl_2O_4$). These were prepared by sol-gel-method as they show the high catalytic performance with glycerol conversion of 90% and 90 % selectivity of 1, 2-propanediol at 220° C under 5.0MPa H_2 pressure for 12 h (42). A. Wolosiak-Hnat and coworker also found that the copper aluminate phase gave good catalytic activity in glycerol hydrogenolysis to 1, 2-propanediol (79 % glycerol conversion , 96% selectivity) (43). The Copper aluminate spinel ($CuAl_2O_4$) have high thermal stability, high mechanical resistance, hydrophobicity and low surface acidity(42), (44). Many methods were studied over prepared $CuAl_2O_4$ spinel, e.g. co-precipitation, so-gel method, sonochemical method and microwave combustion (42-47). Nevertheless, the copper aluminate is generally required high calcination temperature about 1000 ° C several days in order that the complete formation of spinel phase which is difficult to scaling up of synthesis and economic perspective. The flame spray pyrolysis (FSP) is an established commercial process to prepare metal-oxide spinels in a single step (48, 49). The FSP products were made high temperature during FSP process (up to 3000 K) as a result low contaminated compound (50). Moreover, FSP-made can be controlled characteristic by various fuel composition, precursor feed rate, precursor concentration and type of precursor etc. (51, 52).

Although, the Cu-based catalysts have been studied broadly in the literature but there are almost no reported about Cu species (Cu^0,Cu^+,Cu^{2+}) and copper aluminate character on Cu/Al_2O_3 catalyst for glycerol hydrogenolysis. It was often reported that

Cu^0/Cu^+ and Cu^{2+} were active with several hydrogenation reactions like hydrogenation of dienes, and methanol synthesis and Cu^0 was active site for olefin hydrogenation (53). S. Wang et al. suggested that support as catalyst of glycerol dehydration to acetol while acetol hydrogenation occurs on Cu metal (54). Meanwhile, F. Vila reported that the presence of both species (Cu^0/Cu^+) was necessary for glycerol hydrogenation (55). The role of these different species still unclear. In addition, the Cu clusters in metal oxide matrix ($CuAl_2O_4$) after reduction process have different characteristic with Cu clusters are spread on support surface.

In this work, we have studied roles of aluminate spinel modified Al_2O_3 support on Cu based catalysts and have investigated properties of copper species (copper deposited on surface and copper incorporated with metal oxide ($CuAl_2O_4$)), which that prepared by flame spray pyrolysis method on the catalytic performance for glycerol hydrogenolysis.

1.1 Objectives of the Research

The purpose of the study, the effect of aluminate spinel support copper-based catalysts on physicochemical and catalytic properties for hydrogenolysis of glycerol to 1,2 –propanediol.

1.2 Scopes of the Research

Part 1

The *x*Cu-Al_2O_3 support was various weight percentage incorporated Al_2O_3 synthesized by flame spray pyrolysis (x = 0, 10, 20, 30, and 40 wt% of Cu). Then, *x*Cu-Al_2O_3 is impregnated by 30 wt% of Cu as 30Cu/xCu-Al_2O_3. The detail was shown in Figure 1A.

Next, the content of total copper (Cu_{IM} + Cu_{FSP}) will choose from part 1A and various ratio of Cu impregnated per Cu incorporated with Al_2O_3 are prepared by flame spray pyrolysis. Cu/Cu-Al_2O_3 was the loading of partially Cu impregnated on the partially Cu incorporated with Al_2O_3that prepared by FSP. The detail was shown in Figure 1B.

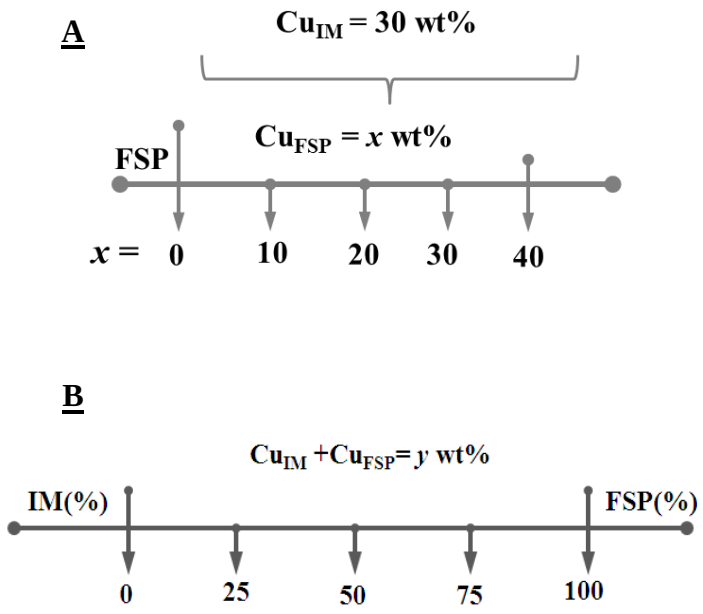

Figure 1 The Cu/Cu-Al_2O_3 catalysts.

Part 2

The xM-Al_2O_3 support was various type of metal (M=Co, Zn, and Fe) and percentage incorporated with Al_2O_3 were synthesized by flame spray pyrolysis (x = 0, 10, 20,30, and 40 wt% of metal). Then, xM-Al_2O_3 was impregnated by 30 wt% of Cu as 30Cu/xM-Al_2O_3. The detail was shown in Figure 2.

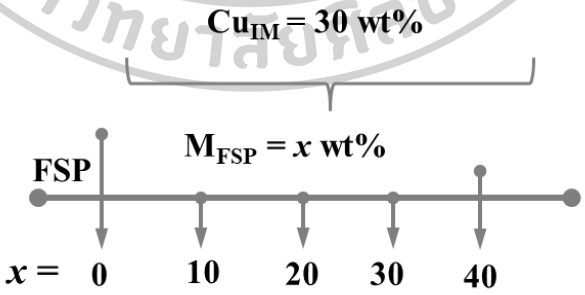

Figure 2 The 30Cu/xM-Al_2O_3 catalysts.

CHAPTER II

GLYCEROL HYDROGENOLYSIS TO 1,2 PROPANEDIOL

Hydrogenolysis of glycerol was an important process to convert crude glycerol to propanediol which valuable chemical products and environmentally friendly. Its reaction produces various products for instance 1, 2-propanediol (propylene glycol), 1, 3-propanediol, ethylene glycol, 1-propanol, 2-propanol, lactic acid. The 1, 2-propanediol is promising chemical product inasmuch as its application is widely used in pharmaceutical, cosmetic, emulsifier/co- surfactant, anti-freeze agent, polymer industries, etc.

In 2010, The Archer Daniel Midland (ADM) Company in the US had licensed the catalytic technology developed at Pacific Northwest National Laboratory. Later in 2011, the company-initiated production 1, 2-propanediol plant at Decatur from glycerol that a capacity of 100,000 ton/years. In mid-2012, the 1, 2-propanediol plant from glycerin (in Ertvelde, Belgium) was produced by the oleochemical company Oleon using BASF catalytic technology license. Its capacity is 20,000 tonnes/years (56).

2.1 Process of glycerol hydrogenolysis

The hydrogenolysis of glycerol to 1, 2-propanediol implicates with series of chemical reactions that lead to a variety of liquid products like 1, 2-propanediol (propylene glycol), 1, 3-propanediol, ethylene glycol, 1-propanol, 2-propanol, lactic acid, etc. Moreover, it produceed gas products that both products are formed via possible reaction pathway in glycerol hydrogenolysis were shown in Figure 3 (57).

Liquid phase products

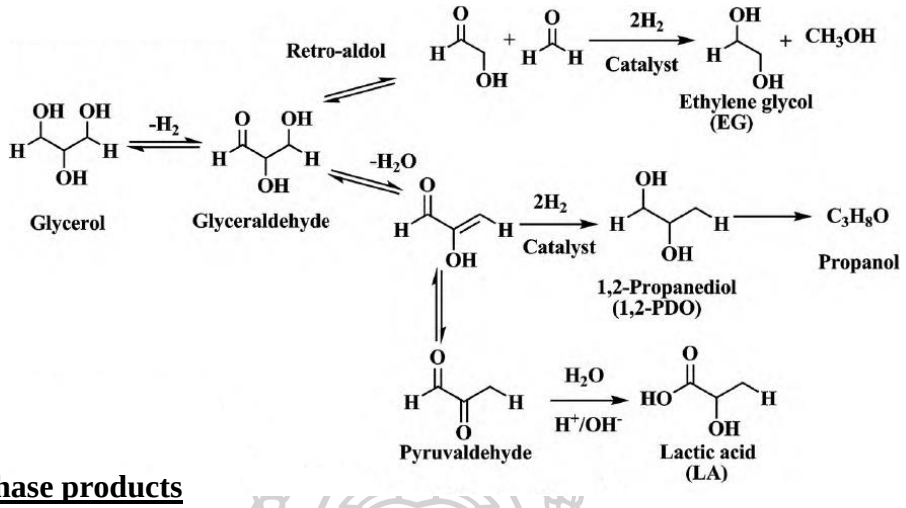

Gas phase products

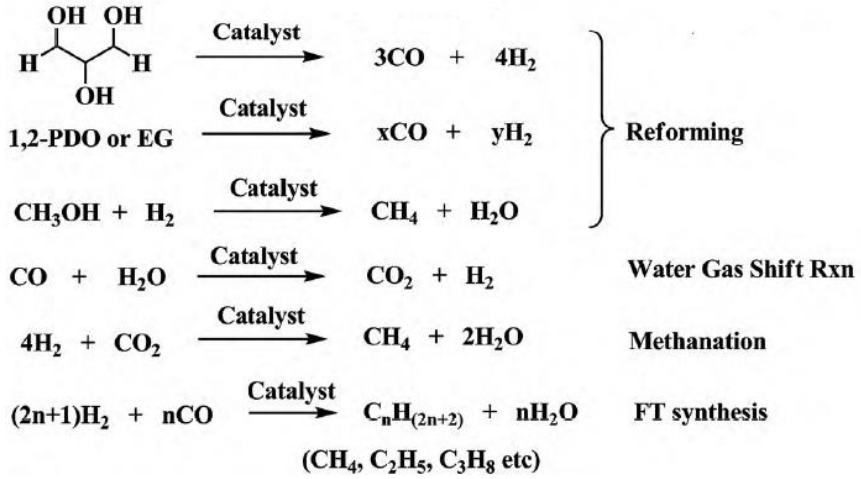

Figure 3 Possible reaction of selective hydrogenolysis of glycerol (57).

1, 2-propanediol product was proposed to be occured through two mechanisms which are (i) dehydration of glycerol to acetol over acid sites afterward acetol was hydrogenated to 1, 2-propanediol over metal sites (dehydration-hydrogenation) and (ii) dehydrogenation of glycerol to glyceraldehydes on basic sites/basic solution then glyceraldehyde was dehydrated to 2-hydroxyacroline on acid sites subsequently hydrogenation of 2-hydroxyacroline to 1,2-propanediol on meta sites (dehydrogenation-dehydration-hydrogenation) as shown in Figure 3 (58-61). The reaction as above mentioned, it is depending on the feature of based-catalyst and environmental of process. Noble catalysts were not employed for glycerol

hydrogenolysis reaction due to their poor selectivity cleavage C-O bond that low selectivity to 1, 2-propanediol and high selectivity undesired products like ethanol, methanol and ethylene glycol. Other hand transition catalysts that high selectivity cleavage C-O bond. In the liquid phase reaction, the acid sites catalyze the glycerol dehydration to acetol which is forthcoming hydrogenated to 1, 2-propanediol on metal sites. M. Balaraju et al. used Ru/C metal catalyst with different solid acid catalyst. their results showed 45 % glycerol conversion and 61 % selectivity of 1, 2-propanediol on NB_2O_5 solid acid catalyst that showed the highest of number of acid sites under reaction temperature 180 °C, 60 bar in hydrogen pressure, 8 h (62). That was similar to work of E. Gallegos-Suarez and coworker who reported that Ru/C catalyst was treated with nitric acid, which exhibited higher glycerol conversion (42%) than catalyst supported on untreated activated carbon at 178 °C under hydrogen pressure of 80 bar, 24 h. It suggested that glycerol hydrogenolysis increase with increasing concentration of surface acid groups (63). A. Alhanash et al. studied glycerol dehydration over Zn–Cr (1:1) mixed oxide catalyst, as shown 18 % of glycerol conversion and 40% selectivity of acetol who proposed reaction mechanism of glycerol dehydration on Lewis acid site was shown in Figure 4 (64).

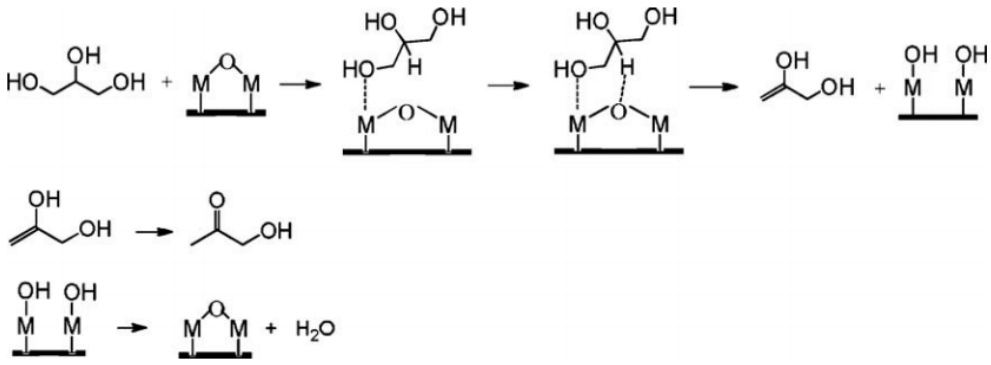

Figure 4 Mechanism of glycerol dehydration on Lewis acid sites (64).

Figure 4 shows the terminal OH group of glycerol rather than the internal one interacts more likely with Lewis acid site (M = lewis acid sites), the terminal OH group of glycerol was transferred to lewis acid site and H^+ from the internal carbon atom migrated to bridging O atom of the oxide produced 2, 3-dihydroxypropene together

with the hydrated active site in the catalyst and then 2, 3-dihydroxypropene was tautomerized to acetol, and the Lewis acid site was regenerated by dehydration of its hydrated form. On the contrary, Brønsted acid sites also proposed to catalyze glycerol dehydration into acetol, as showed in Figure 5, glycerol molecule interacted with a proton site that bring to the protonation of the internal oxygen in the glycerol molecule, which internal oxygen higher negative charge compared to the terminal oxygens. Following steps implicated elimination of H_3O^+ to produce 1, 3-dihydroxypropene and its tautomerisation to 3-hydroxypropanal. Then, 3-hydroxypropanal encountered acid-catalysed dehydration to give yield acrolein. Finally, the proton site is regenerated by interaction of its conjugate base with H_3O^+. Similar mechanism for acrolein formation has been suggested previously (64-66).

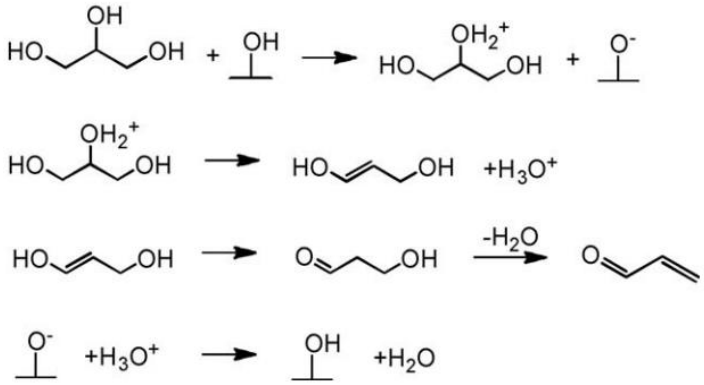

Figure 5 Mechanism of glycerol dehydration on Brønsted acid sites.

It was reported that addition of alkaline improved the glycerol hydrogenolysis reaction. E. P. Maris et al suited the addition of NaOH solution on reaction which Pt/C and Ru/C were used catalyst found that the presence of NaOH enhanced glycerol conversion in both catalysts, (13 to 92 % glycerol conversion over Pt/C, 40 to 100 % glycerol conversion over Ru/C) under reaction temperature of 200 °C, pressure 40 bar with H_2, 5 h of reaction (67) but Z. Huang et al. reported the conversion and selectivity of the catalysts in glycerol reactions decreased with increasing sodium content because sodium as s a base which weakly promoted the activity (27). Generally accepted formation route of 1, 2-propanediol under alkaline conditions. First step that occurred dehydrogenation of glycerol over metal sites assisted by the base to form

glyceraldehyde, which dehydrates to 2-hydroxy-2-propenal over base sites, and finally 1, 2-propanediol is produced from 2-hydroxy-2-propenal via a two-step hydrogenation process as shown in Figure 6 (68).

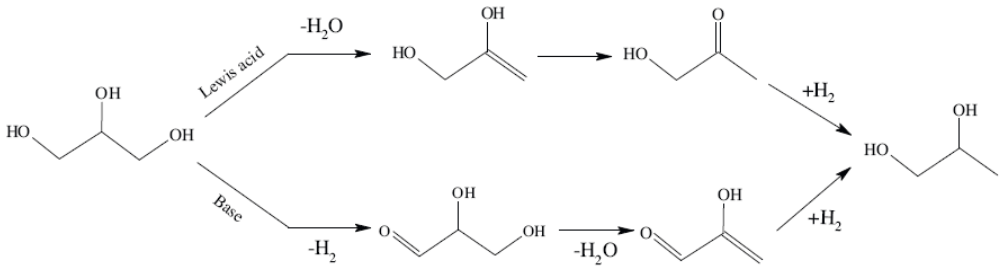

Figure 6 Glycerol hydrogenolysis pathway to 1, 2-propanediol (68).

2.2 Glycerol hydrogenolysis to 1,2-PDO over Cu-based catalysts

It was well known that copper-based catalysts offer excellent selectivity to 1, 2-propanediol because of its high C-O bond cleavage and poor C-O bond cleavage. Copper based catalysts were extensively studied on various supports for example SiO_2, TiO_2, Al_2O_3, ZnO, and Cr_2O_3. L. Guo et al. studied the effect of different supports on Cu-based catalysts who found that Cu/Al_2O_3 showed the highest of glycerol conversion and selectivity of 1, 2-propanediol who suggest that the Al_2O_3 as acidity to catalyze for the dehydration of glycerol to give acetol and thus facilitate the formation of propanediols (69). Therefore, the support also played a role in the catalysis besides immobilizing and dispersing the active Cu species. Z. Yuan et al. who investigated the CuO/MgO catalysts prepared by impregnation and coprecipitation. Found that, the CuO/MgO was prepared by coprecipitation had the best activity due to this method has the cross-linked rod outline, smaller copper particles (70). Table 1 shows the different metal oxide support on performance of Cu-based catalyst.

For the current studies, the Cu/Al_2O_3 catalyst was investigated; the activation processes of $Cu/\gamma\text{-}Al_2O_3$ for glycerol hydrogenolysis were studies by F. Vila et al. the authors reported different Cu surface species were generated during the activation process, which partially reduced Cu species (Cu^+) improve activity, Cu^{2+} species appear on calcinations process that were less active and 1, 2 - propanediol selectivity was

strongly dependent on the Cu^0/Cu^+ atomic ratio (55). This observation was consistent with the results of Z. Xiao et al. who suggested that the high glycerol conversion was obtained catalyst with optimum surface Cu^0/Cu^+ ratio (53). Moreover, the Cu/Al_2O_3 catalysts were studies via DFT in order to understanding of the copper and alumina roles which displayed the influence on the activity of acidic active on alumina support and the metallic Cu site. The results presented that Cu/Al_2O_3 catalyst was high conversion and selectivity when compared with single component of copper and alumina under reaction temperature of 220 °C, initial pressure of 5 MPa, time 6 h. For calculation results showed that the alumina surface and its hydroxylation had a significant impact on activity. The acidic sites (Al sites) on alumina support could be as active as the Cu site toward glycerol and acetol adsorption when the alumina surface is partially hydroxylated (71), while Y. S. Yun et al. who suggested reaction mechanism of glycerol dehydration on Cu/Al_2O_3 and $Cu\text{-}Ni/Al_2O_3$ for hydrogenolysis with aqueous phase reforming (APR) of glycerol. They proposed that the terminal OH group of glycerol active with Cu metal and then glycerol was dehydrated into acetol on acidic sites of alumina support, finally 1,2-propanediol is produced via hydrogenation. When presence the Ni metal, it delivered hydrogen from the APR of glycerol to the primary or terminal carbon of the glycerol which is adsorbed onto Cu metal (see in Figure 7) (72).

มหาวิทยาลัยศิลปากร

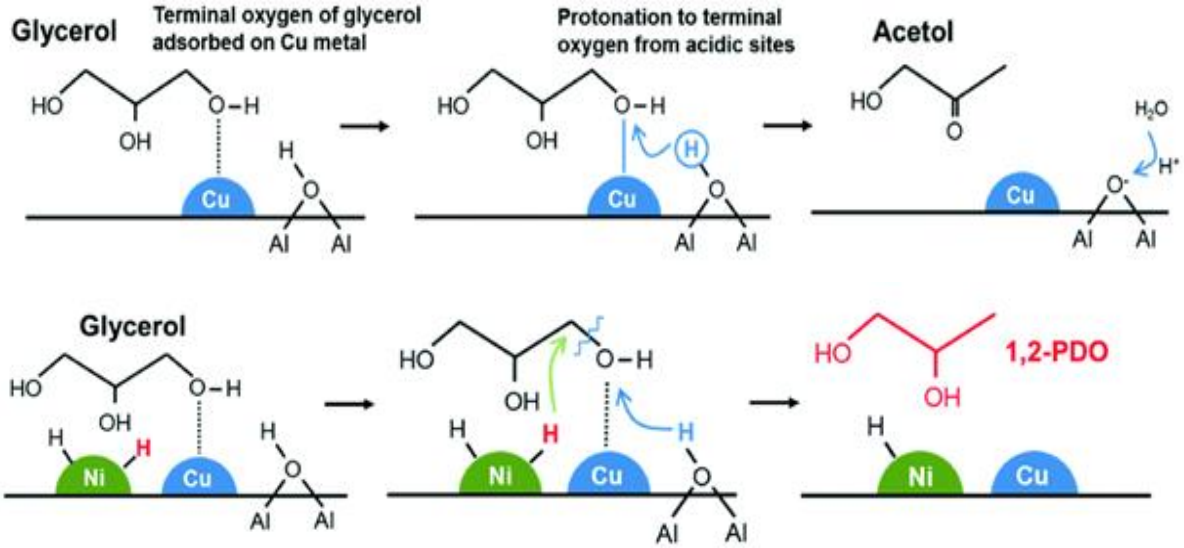

Figure 7 Proposed reaction pathway for hydrogenolysis of glycerol to 1,2-propanediol with aqueous phase reforming over Cu–Ni/Al_2O_3 catalyst (72).

Table 1 The metal oxide support on performance of Cu-based catalyst.

Ref	Catalyst	Conversion of glycerol (%)	Selectivity of 1,2-PDO (%)	Reaction condition
(69)	Cu/Al_2O_3	35	94	P_{H2}=15 bar, Temp.=200°C, Time=10 h
	Cu/HY(zeoite)	4	77	Speed = 400 rpm ,50 wt% of glycerol solution
	Cu/Hβ	4	n.d	
(73)	Cu/boehmite	78	93	P_{H2}=40 bar, Temp.=200°C, Time=10 h,
	$Cu/\gamma\text{-}Al_2O_3$	54	81	16g glycerol in 4 ml of H_2O, 5wt% of catalyst
	Cu/SiO_2	52	89	
(74)	$Cu_{10}Zn_oAl_{90}$	50	80	P_{H2}=40 bar, Temp.=180°C, Time=10 h,
	$Cu_{10}Zn_{15}Al_{75}$	71	92	80 wt% of glycerol solution,
	Cu/ZnO (1:1)	47	85	
(75)	0.2CuZr	6	3	P_{H2}=40 bar, Temp.=200°C, Time=8 h,
	0.4CuZr	10	3	Speed = 500 rpm, 40 wt% of glycerol solution
	1CuZr	8	7	catalyst 0.6 g
	2.5CuZr	12	11	
	6CuZr	12	11	
(21)	Cu-ZnO	96	97	P_{H2}=50 bar, Temp.=220°C
	Cu^{2+}:Zn^{2+}=1:1.4 molar ratio			Time=8 h, 20g gly. /lit of DI water
				cat.9 g
(76)	Cu-Cr	15	82	P_{H2}=52 bar, Temp.=220°C, Time=5 h,
	Cu-Cr (Al)	32	83	20 wt% of glycerol in 2-propanol
	Cu-Cr (Ba)	34	83	
	Cu-Cr (Zn)	30	75	
	(x)=(promoter)			
(70)	CuO-10/MgO-IM	26	93	P_{H2}=30 bar, Temp.=100°C, Time=20 h,
	CuO-10/MgO-CP	49	97	75 wt.% aqueous solution of glycerol 8.0 ml
				1.0 g of reduced catalyst

Recently, there have been reported that the copper alum inate structure ($CuAl_2O_4$) exhibited high catalytic performance. B. K. Kwak et al. explored the use of copper aluminate were prepared by different calcination temperature via sol-gel method and reported the $CuAl_2O_4$ was initailly discovered after calcination at 600 °C, only copper aluminate spinel peak were observed at 800 °C (see Figure 8A) which contains only the $CuAl_2O_4$ phase achived the highest catalytic performance of 90% glycerol conversion and selectivity (42). Besides, who investigated the effect of citric acid concentration for formation of $CuAl_2O_4$ crystalline. In case of addition a small amount citric acid (1 to 2), the $CuAl_2O_4$ crystalline size were small while increased amount of citric acid (2.5 to 3), the $CuAl_2O_4$ crystalline were larger (see Figure 8B). This indicates that the citric acid concentration has an effect on the size of $CuAl_2O_4$ produced. A. Wolosiak-Hnat et al. proposed a Cu/Al_2O_3 catalyst that prepared by coprecipitation, the Cu/Al_2O_3 catalyst consist of Cu metal, delafossite $CuAlO_2$, copper aluminate $CuAl_2O_4$ and spinel $CuAl_4O_7$ phase. It found that high catalytic activity in glycerol hydrogenolysis exhibited when Cu metal, delafossite $CuAlO_2$ and copper aluminate $CuAl_2O_4$ presenced (43).

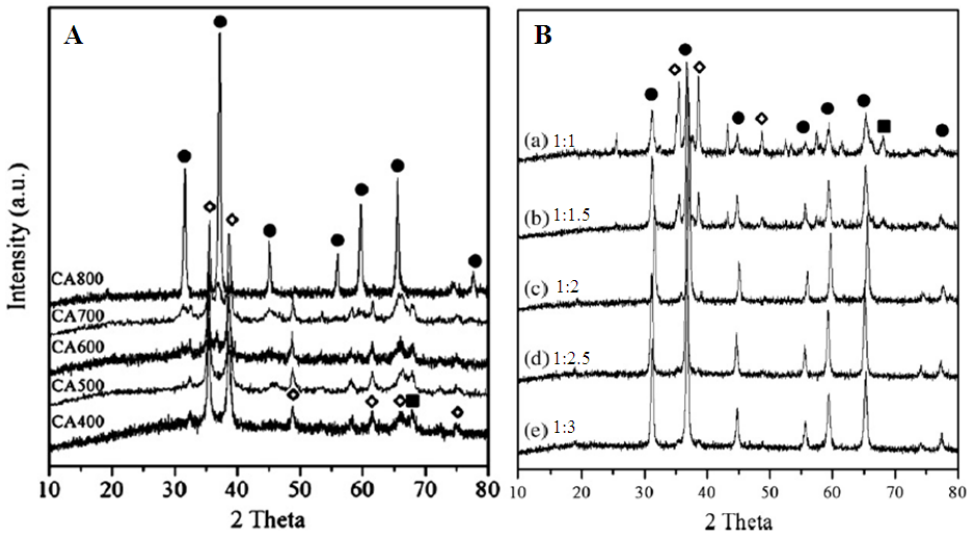

Figure 8 XRD patterns of samples after calcined at different temperatures and different ratio C_M : C_{cit} at calcined 800 °C : $CuAl_2O_4$ (●), CuO (◊), Al_2O_3 (■) (42).

CHAPTER III

FLAME SPRAY PYROLYSIS

Flame spray pyrolysis (FSP) was a conventional technique for producing nanoparticles and materials in one-step with high specific surface area, high purity and primary particle size in a range of nanometer. The FSP products include a wide variety of single-metal oxides (e.g. Al_2O_3, SiO_2, and ZrO_2) (48, 77-79), complex metal oxides (e.g. YSZ and YAG) (80-82), carbon blacks, ceramic materials, spinel structure (e.g. $CuAl_2O_4$ and $CoAl_2O_4$). In the FSP synthesis, the organometallic liquid precursor was dissolved in a fuel of solvent (e.g. xylene, toluene, ethanol, methanol, and isopropanol) and then injected through the center capillary of the nozzle-equipped burner by a syringe pump. The mixture of organometallic liquid precursor and fuel solvent was dispersed into the flame with oxygen and premixed methane/oxygen flamelet ignites. The precursor droplets were evaporated and combusted generating small clusters that grow up via the sintering and coalescence process. These processes occurred at a high temperature (up to 3000 K) and short residence time (a few milliseconds). Figure 9 shows the Schematic of the FSP experimental setup and the particle formation process (83).

มหาวิทยาลัยศิลปากร

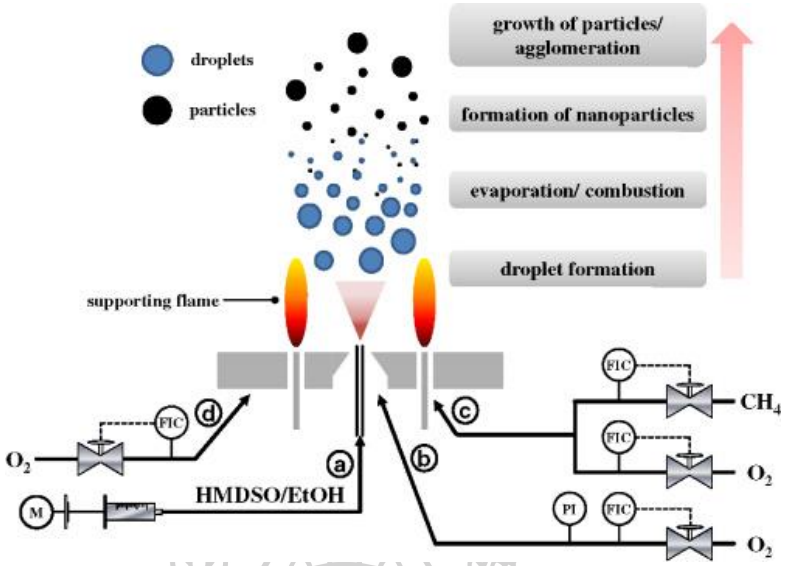

Figure 9 Schematic of the FSP experimental set up and the particle formation process (83).

The flame spray pyrolysis process can be designed character of the FSP-made particles through control of fuel solvent composition, kind of liquid precursor used, precursor concentrations, a feed rate of precursor and flame conditions. S .Lee et.al (84) studied the $Cu/ZnO/Al_2O_3$ catalysts were synthesis via flame spray pyrolysis method under various metal precursor type (nitrate and organometallic type) The nitrate source used copper (II) nitrate tri-hydrate, zinc nitrate hexa-hydrate and aluminum nitrate nona-hydrate that diluted with an ethanol solution. While copper bis-2-ethylhexanoate**,** zinc bis-2-ethylhexanoate and aluminum sec-butoxide were dissolved in xylene that were starting material of organometallic precursor type. The catalyst gave from nitrate precursor exhibited a higher reducibility, a higher metal surface area and high catalytic performance for direct DME reaction than using the organometallic precursor**.** Therefore, the precursor types have an impact on catalytic properties. The flame-made Co/ZrO_2 were preparated using FSP with different precursor feed rates (3 to 8 ml/min) and cobalt loading (5 to 10 w.t%). For FSP operation, the premixed flame gas for supporting flame ring were CH_4 (1.5 l/min) and O_2 (3.2 l/min), the metallic precursor was fed and dispersed with oxygen (5 l/min) at constant pressure of 1.5 bar. The XRD crystallite size and particle size of nanoparticle were shown in Figure 10. the increasing Co loading hardly influenced to particle size of ZrO_2 according to Figure 10a. The

resulting particle size of ZrO_2 increased with increasing precursor feed rate from 3 to 8 ml/min (Figure 10 b). It was suggested that in increasing precursor feed rate increased enthalpy of flame, residence times and flame temperature, which promoted coalescence and sintering during FSP process (52).

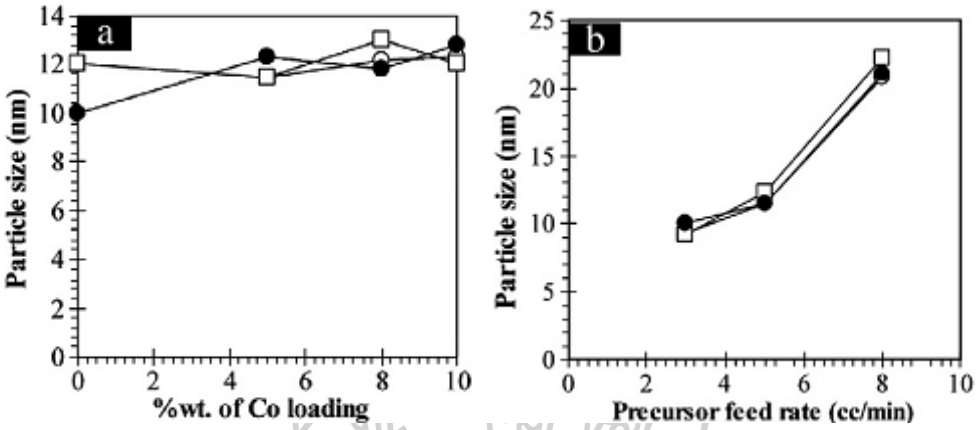

Figure 10 The XRD crystallite (d_{XRD}, □) , particle size from TEM (d_{TEM}, ●), and particle size from BET (d_{BET}, ○) as a function of cobalt loading (a) and precursor feed rate (b) (52).

The FSP made silica particles with various silicon precursors and precursor concentrations were reported by K.Cho and group (85). The silicon precursor used tetraethylorthosilicate (TEOS) and silicic acid ([SiOx(OH)4−2x]n). For the TEOS precursor, the resulting of specific surface areas decreased from 285 to 81 m^2/g with increasing precursor concentration from 0.1 to 0.5 M. while the average particle sizes of silica particles increased from 10 to 34 nm with increasing precursor concentration (Figure 11 (a)). These results indicated that the specific surface area and particle size can be controlled through an increase in the precursor concentration. TEM micrographs were of silica particles as shown in Figure 11 (b-d). The silica particles with a precursor concentration of 0.1 M produced chain-like aggregate particles. Whereas the TEOS concentration of 0.5 M obtained the dispersed particles, the aggregate particles were rarely found. There were dispersed and aggregated particles at the concentration of 0.3 M. It was proposed that the low concentration of liquid droplet was perfectly evaporated

in a short time of evaporation process during FSP, where the resulting evaporated precursor was formed silica aggregates. The silica particles prepared using silica acid ([SiOx(OH)4−2x]n). The specific surface areas decreased and the average particle sizes increased with increasing precursor concentration (Figure 12 (a)). The TEM image of the silicic acid precursor at various concentrations shown in Figure 12 (b-d). The morphologies of silica were spherical and isolate particles. The silica particle size made from silicic acid was larger than that the obtained from TEOS precursor. Owing to the volatility of silicic acid was lower, as a result, the evaporation time was infinitely long.

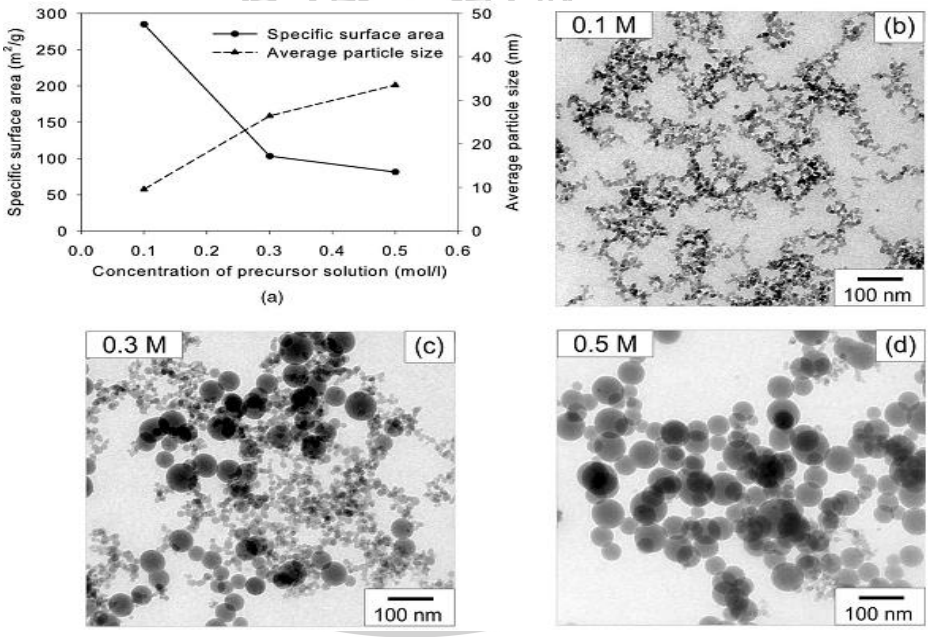

Figure 11 (a) the specific surface areas and average particle sizes of silica particles produced from TEOS precursor as a function of various concentrations. TEM image of silica particles for (b) 0.1, (c) 0.3, and (d) 0.5 M (85).

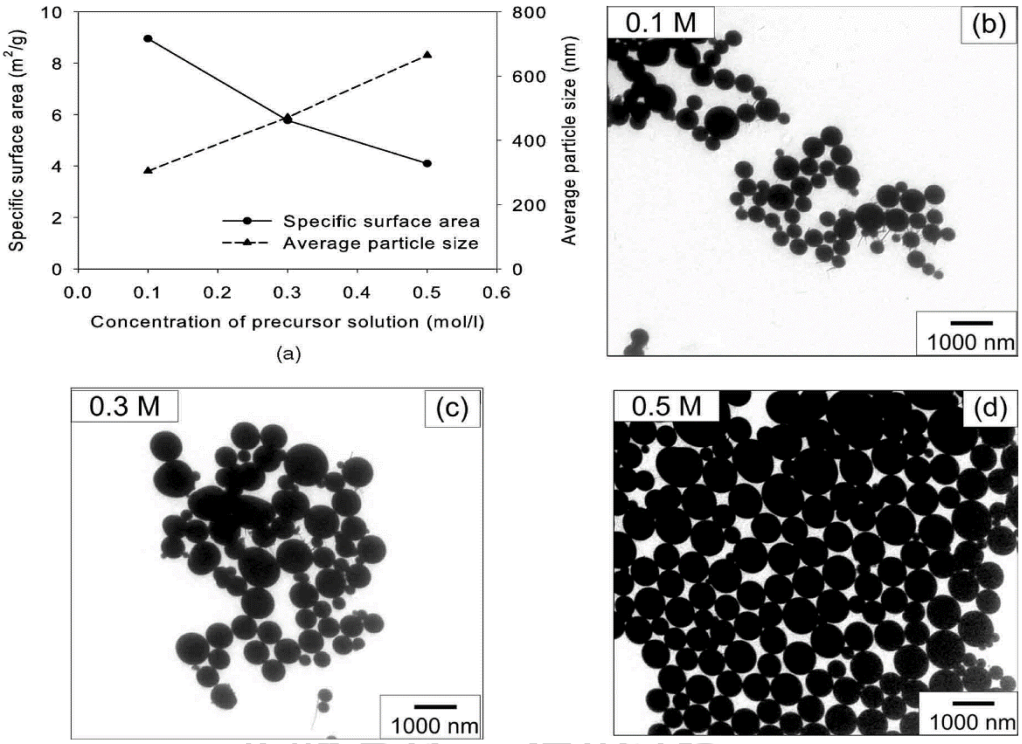

Figure 12 (a) the specific surface areas and average particle sizes of silica particles produced from silicic acid precursor as a function of various concentrations. TEM image of silica particles for (b) 0.1, (c) 0.3, and (d) 0.5 M (85).

The feed flow rate and precursor concentration for FSP production of the Pd/TiO_2 nanoparticles were investigated by O. Mekasuwandumrong and coworker (51). The precursor concentration increased from 0.3 to 0.5 M, there was an increase in particle size of Pd/TiO_2 and a correlative decrease in the percentage of the anatase phase. These results can be explained that higher precursor concentration presented longer residence times and higher flame temperature, as increased sintering and phase transformation during FSP synthesis. H.Y. Koo et al. (85) reported that the average particle size of silver-glass composite power increased with an increase in the precursor concentration. the increasing concentration of the spray solution increases the concentration of evaporating vapor inside the diffusion flame, nucleation and growth mechanism. Y. Li et al. (86) investigated the chainlike MFe_2O_4 (Cu, Ni, Co, Zn) nanoaggregates were prepared by FSP. The FSP made particle appeared metal spinel

ferrites that were $CuFe_2O_4$, $NiFe_2O_4$, $CoFe_2O_4$, and $ZnFe_2O_4$ spinel. The results from SEM showed the spherical shape of $CuFe_2O_4$ nanoaggregates. The nanocrystallite size was about 8-20 nm (Figure 13). The chainlike particle was formed by sintering of primary particle in flame taking place in the high temperature and then it cools more rapidly.

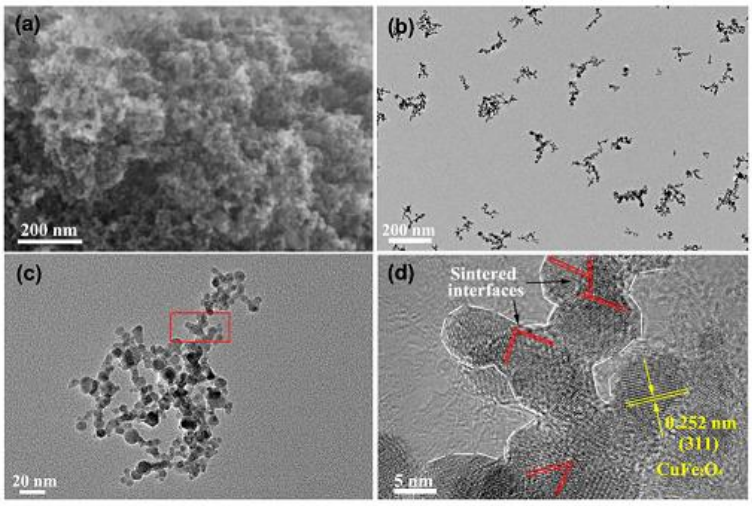

Figure 13 (a) SEM, (b,c) TEM and (d) HRTEM image of $CuFe_2O_4$ nanoaggregates (86).

The CuO-ZrO_2 particles were prepared two-nozzle flame spray pyrolysis (2-FSP). Each metal liquid precursor was diluted with mixture solution of xylene and 2-ethylhexanoic acid. After that each metal solution was injected to the center capillary of the nozzle at 5 ml/min by syringe pump, and was dispersed in to flame with 5 l/min of O_2. the premixed CH_4/O_2 for supporting flame ring and ignition was 3 l/min. This note as CuO-ZrO_2-A particle (Figure 14 (a)). The CuO-ZrO_2-B was synthesized with 10 l/min of O_2 dispersion for copper nozzle-equipped (Figure 14 (b)). The flame conditions of zirconium nozzle-equipped were kept the same. CuO and ZrO_2 were prepared by one-nozzle flame pyrolysis (1-FSP), as noted CuO (FSP) and ZrO_2 (FSP), respectively (Figure 14 (c)). The CuO clusters size decreased with a higher O_2 dispersion (10 l/min) because the quenching of the ignited spray of the copper precursor was increased and bring to a shorter residence time of CuO clusters in flame zone. The CuO size of CuO-ZrO_2-B was smaller than CuO-ZrO_2-A, leading to higher BET surface

area, metal dispersion and metallic Cu surface (87). The characteristic of FSP-made particle can be controlled by adjusting the nozzle distance of two-nozzle FSP. J.A.H. Dreyer et al. (88) found that a higher distance between the two nozzle flame resulting in a expended sintering process, an increase in particle size and thus reduced active surface.

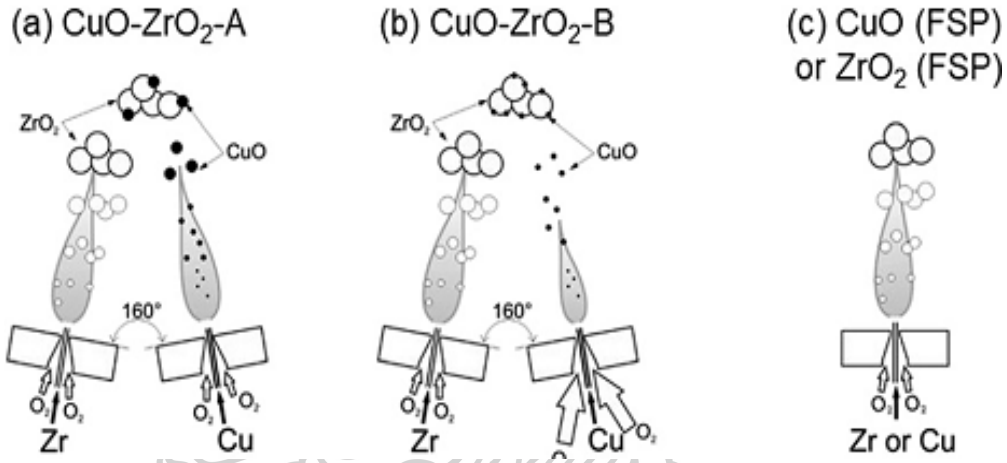

Figure 14 Schematics of (a and b) two nozzle flame spray pyrolysis (2-FSP) and (c) one-nozzle flame spray pyrolysis (1-FSP) (87).

The nanostructure with different morphologies were synthesis by FSP. For example, core-shell, nanorod, hollow sphere and nanotube. S.H. Choi et al.(89) have prepared $AgBaTiO_3$ core shell with various Ag loading (5-30 wt.%), which the single-crystalline Ag as the core part, Ba and Ti as the shell part. The formation mechanism of core shell was shown in Figure 15. The liquid precursor droplet was generated to dry droplet by ultrasonic spray generator, and then the micron-sized precursor powder of Ag, Ba and Ti were formed in flame**,** where the precursor powders were decomposed and were completely evaporated generating vapor form of BaO, TiO_2 and Ag, which grow up by nucleation and coagulation processes taking place in a high temperature of flame. The core shell was formed through the melting and crystallization of the Ag composition. The Ba and Ti composition moved out the internal part and formed to the shell part. Figure 16 shows TEM images of the pure $BaTiO_3$ and $AgBaTiO_3$ core-shell.

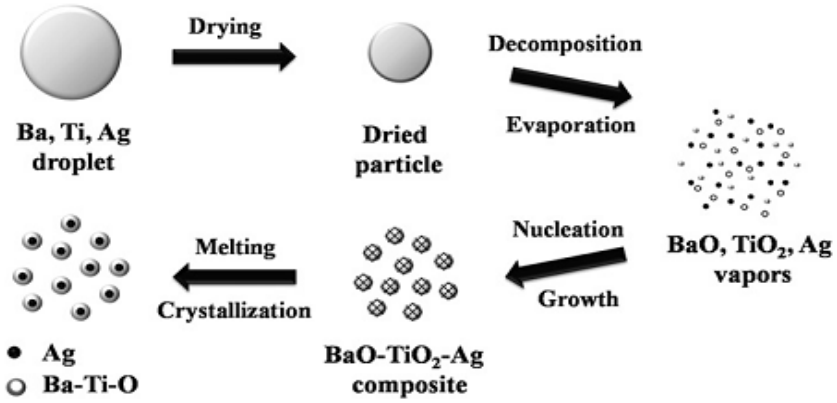

Figure 15 Schematic diagram of formation mechanism of core-shell structure $AgBaTiO_3$ composite powders in the flame spray pyrolysis.

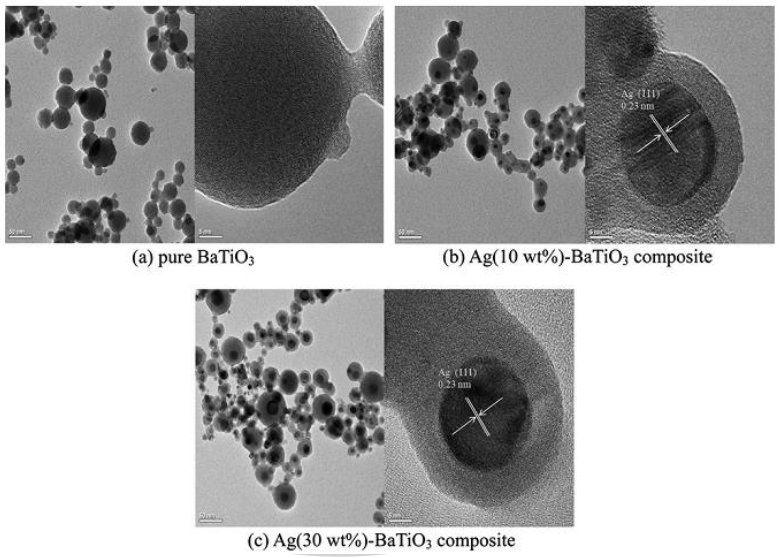

Figure 16 TEM images of the pure $BaTiO_3$and $AgBaTiO_3$ composite powders prepared directly by flame spray pyrolysis.

The ZnO nanorod with different solvent solution using the pilot-scale FSP was investigated. Zinc precursors were diluted in ethanol solvent and compare with methanol solvent. The prepared ZnO nanorod using zinc nitrate-ethanol precursor solution, the diameter and length of nanorod were 20-30 nm and 30-250 nm, respectively. The nanorod was hexagonal shape which the nanorod was assembled from two or more shorter as shown in Figure 17 (a). Addition, some nanorod assembled into

tetrapods seen in Figure 17 (b). For the ZnO nanorod synthesized from zinc nitrate-methanol precursor solution. The shape of nanorod was both spherical and hexagonal as presented in Figure 17 (c). These indicated that the types of solvent were influent for formation mechanism of ZnO nanorod in FSP (90).

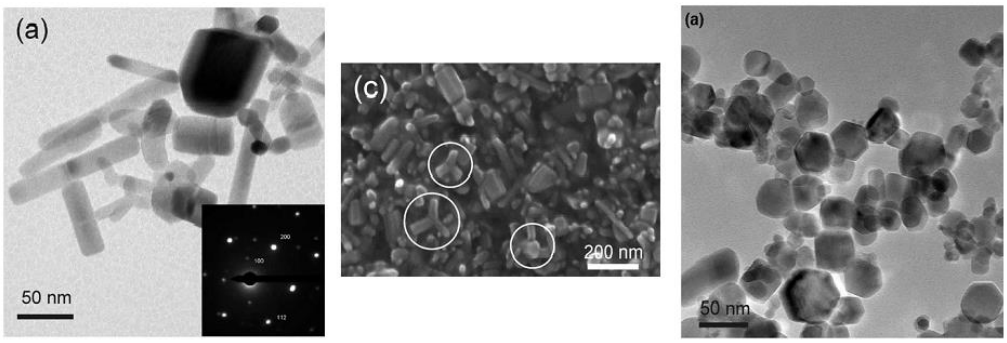

Figure 17 (a) TEM image of nanorods made from zinc nitrate/ethanol precursor solutions (b) SEM image revealing the presence of tetrapods (circle) in the product powders, (c) TEM image of nanorods made from zinc nitrate/methanol precursor solutions (90).

มหาวิทยาลัยศิลปากร

CHAPTER IV

EXPERIMENTAL SECTION

Table 2 The chemicals used in the preparation of catalysts.

Chemical material	Formula	Grade	Manufature
Aluminum tri-sec-butoxide	$Al[OCH(CH_3)C_2H_5]_3$	97%	Sigma-Aldrich chemistry
Cupric acetyacetonate	$C_{10}H_{14}CuO_4$	98%	Fluka
Iron(III) acetylacetonate	$Fe(C_5H_7O_2)_3$	97%	Sigma-Aldrich chemistry
Zinc Napthanate	$C_{22}H_{14}O_4Zn$	8% metal	Sigma-Aldrich chemistry
Cobalt Napthanate	$CoC_{22}H_{14}O_4$	6% metal	Sigma-Aldrich chemistry
Copper (II) nitrate trihydrate	$CuN_2O_6.3H_2O$	98%	Sigma-Aldrich chemistry
Xylene	C_8H_{10}	99%	Panreac

4.1 Catalyst preparation

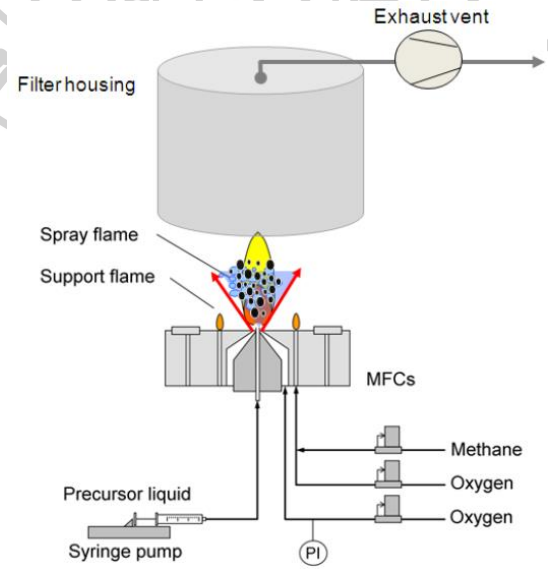

Figure 18 Scheme of Flame spray pyrolysis.

4.1.1 Preparation of catalysts by Flame Spray Pyrolysis

The FSP reactor was used for preparation of catalyst was shown in Figure 18. A cupric acetylacetonate or iron (III) acetylacetonate, zinc napthanate, cobalt napthanate, and aluminum-tri-sec-butoxide (as listed in Table 2) were used as precursor and diluted with xylene to a 0.5 M solution. The liquid precursor was fed in the center of a methane/ oxygen flame by syringe pump at 5 ml/min. Dispersed by oxygen was fed at 5 ml/min. The pressure drops at the nozzles allowed the synthesis was held constant at 1.5 bar by adjusting the orifice gap area at the nozzle. The catalyst powder was collected on a glass microfiber filter (Whatman) with the aid of a vacuum pump.

4..1.2 Preparation of catalysts by Wet Impregnation

The support Cu-Al_2O_3 and M-Al_2O_3 (M = Zn, Fe and Co) with different amount of metal loading were prepared by FSP. It was impregnated by copper (II) nitrate trihydrate 98% (Cu = 30wt %). The Cu precursor was dissolved in deionized water and the solutions were mixed the support. The mixture solutions were stirred at 70 °C for 6 h and then the sample was oven-dried at 110°C for 12 h, and finally calcined at 400°C for 3 h in 30 ml/min of airflow. The catalysts used in this research were symbolically assigned as show in Table 3.

Table 3 The symbol of the catalysts.

Symbol	Catalyst
Al_2O_3	• Al_2O_3 prepared by FSP method
30Cu/Al_2O_3	• 30 wt% Cu impregnated on Al_2O_3 prepared by FSP method
30Cu-Al_2O_3	• 30 wt% Cu incorporated with Al_2O_3 prepared by FSP method
10Zn-Al_2O_3	• 10 wt% Zn incorporated with Al_2O_3 prepared by FSP method
30Cu/10Cu-Al_2O_3	• 30 wt% Cu impregnated on 10 wt% Cu incorporated with Al_2O_3 prepared by FSP method
30Cu/10Zn-Al_2O_3	• 30 wt% Cu impregnated on 10 wt% Zn incorporated with Al_2O_3 prepared by FSP method

4.2 Catalyst characterization

4.2.1 N_2 physisorption

The BET surface areas were performed by N_2 physisorption using BET DORP mini II. First, A 0.1 g of catalysts were pretreated under helium gas flow of 50 ml/min at 200 °C for 3 h, which in order to remove water bound to the particle surface from air moisture. After that the catalyst was cooled down to the ambient temperature and weight of dried catalyst was recorded. For adsorption part, the sample cell was installed with BET DORP mini II equipment. The essential data were input to the software program. The sample cell was dipped in the dewar containing liquid nitrogen. The volume of N_2 was measured at -196 °C using the different N_2 partial pressure.

4.2.2 X-ray diffraction (XRD)

The XRD patterns were performed on X-Ray Diffractometer Bruker AXS Model D8 Discovere using CuKα radiation (λ=1.5406 Aº). The diffract grams were recorded from 10 to 80° C with scanning rate 2°/min. The crystallite size was estimated from line broadening according to the Scherrer equation. The calculation method was presented in appendix A.

$$\text{Crystalline size} = K.\lambda/B.\cos\theta$$

Where, K= 0.9 (Crystalline-shape factor), λ = 1.5418 A° for CuKα (wavelength of X-ray) and B is X-ray diffraction broadening).

4.2.3 Temperature Programmed Reduction (TPR)

The reduction behaviors of catalyst were studied by temperature programmed reduction (TPR) technique as using a Micrometritics Pulse Chemisorb 29100 instrument. A 0.1 g of catalyst samples was packed in a quartz tubular reactor and then was heated to 150 °C at a rate of 10 °C/min under 30 ml/min of nitrogen flow for 1 h, after that cooled down to room temperature under nitrogen flow. Next, the reducing gas (10% H_2 in N_2) was switched on at 30 ml/min, and the temperature was raised at a rate of 10 °C/min until it reached 800 °C.

4.2.4 N_2O Decomposition

Active sites of copper metal were measured by N_2O decomposition. A 0.1 g of a catalyst sample was packed in a quartz tubular reactor. The catalyst was heated to 300 ºC under atmosphere pressure of helium with a flow rate 30 ml/min and exchange for hydrogen gas then held at 300 ºC for 3 h. After that reactor temperature was cooled down to room temperature by helium at a flow rate of 15 ml/min. The metal active sites were measured when catalyst was heated to 90 ºC. The purity N_2O gas was injected into the injection port to adsorb on the metal surface of the catalyst sample. Injection of N_2O was continuously repeated until saturation.

4.3 Glycerol hydrogenolysis activity measurement

The hydrogenolysis of glycerol was performed in 100 ml autoclave Prior to the activity test, the catalyst sample was reduced in a flow of H_2 with flow rate of 30 ml/min at 300 °C for 3 h. In the typical reaction experiment, 40 ml of aqueous glycerol solution (20 wt% glycerol) and 1 g of reduced catalyst were loaded to the autoclave and then purged 3 times with H_2 at room temperature to remove the air in process. Afterward, the reactor was pressured in 20 bar of H_2, the reactant mixture was heated up to 220 °C under agitation. After 15 h. reaction, the liquid mixture was centrifuged for pull off the catalyst. The composition of product (1, 2 propanediol, 1, 3 propanediol, acetol, 1-propanol, 2 propanol and methanol) was analyzed by gas chromatography (Shimadzu GC14B) using capillary column (BP-210) 30mx0.32mmx0.5μm) equipped with flame ionization detector. These samples were analyzed using acetonitrile as internal standard.

$$\textbf{Conversion (\%)} = \frac{\text{initial mole of glycerol-final mole of glycerol}}{\text{initial mole of glycerol}} \times 100$$

The selectivity to each product was defined based on carbon as follows:

$$\textbf{Selectivity (\%)} = \frac{\text{mole of 1,2 PDO}}{\text{moles of glycerol (convert.)}} \times 10$$

CHAPTER V

ROLE OF COPPER ALUMINATE SPINEL SUPPORT ON COPPER-BASED CATALYST FOR HYDROGENOLYSIS OF GLYCEROL TO 1,2 PROPANEDIOL

The effect of the copper inserting on Cu/Al_2O_3 catalyst during FSP method and role of copper aluminate on the catalytic properties were discussed in this chapter. The results and discussion in this chapter are divided into two section. In the first section, the physical and chemical properties of copper aluminate and Cu-based catalysts are evidenced. This result includes the crystalline and copper aluminate phase of catalyst were examined by X-ray diffraction (XRD), The BET surface area and pore characteristics were analyzed using N_2 physisorption, the reduction behavior and the reducibility of catalyst were determined by temperature programmed reduction (TPR), and the copper metallic active sites were measured by the dissociative N_2O decomposition. The catalytic performance for glycerol hydrogenolysis reaction was evaluated in the last section.

5.1 The physical properties of Cu inserted on copper-based catalysts

5.1.1 The phase analysis by X-ray diffraction (XRD)

The XRD patterns of the FSP-inserted Cu with Al_2O_3 by (xCu-Al_2O_3) were presented in Figure 19. The XRD diffraction peak at 2θ = 32.0º, 37.0º, 45.8º, and 66.5º were observed in these sample, corresponded to the characteristic of γ-Al_2O_3. The alumina from FSP technique represented γ-Al_2O_3 phase as according to previous research (91-93). The diffraction peak at 32.5º, 35.6º, 38.8º, 48.8º,53.5º, 58.3º, 61.6º,68.1º, 72.4º, and 75.2º were assigned to CuO phase (94). The peak of copper aluminate spinel ($CuAl_2O_4$) appeared at about 2θ = 32.0º, 37.4º, 45.5º, 56.3º, 60.0º, and 65.9º. With addition of Cu in FSP step, the intensity of CuO peak increased with increasing Cu loading. It was indicated that a simple formation of large CuO particles. Moreover, the peak of CuO phase was clearly observed at higher Cu loading while the peak of $CuAl_2O_4$ phase was evidently found at lower Cu loading. This attributed that a

small amount of copper insertion can form to more $CuAl_2O_4$ phase than CuO phase. The crystalline size of CuO was determined from XRD data following to the Scherrer's equation was listed in Table 4.

Figure 20 shows the XRD pattern of 30 wt% Cu loading on the FSP-inserted Cu with Al_2O_3 catalysts (30Cu/xCu-Al_2O_3). The XRD pattern of 30Cu/Al_2O_3 catalyst exhibited diffraction peak of CuO and γ-Al_2O_3 phase, while the $CuAl_2O_4$ phase disappeared in diffraction line. In contrast, the $CuAl_2O_4$ still found on XRD pattern of the 30 wt% Cu on Cu-Al_2O_3 catalysts. It was indicated that $CuAl_2O_4$ spinel phase was formed during FSP step.

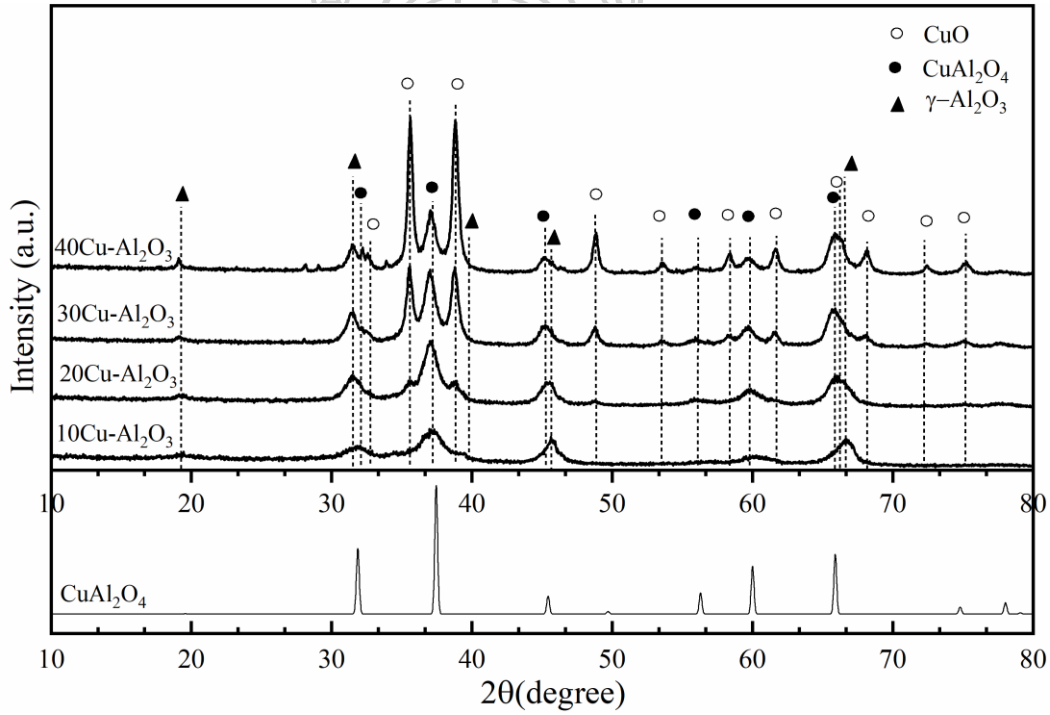

Figure 19 The XRD pattern of the FSP-inserted Cu (xCu-Al_2O_3, x=0, 10, 20, 30, and 40 wt% Cu).

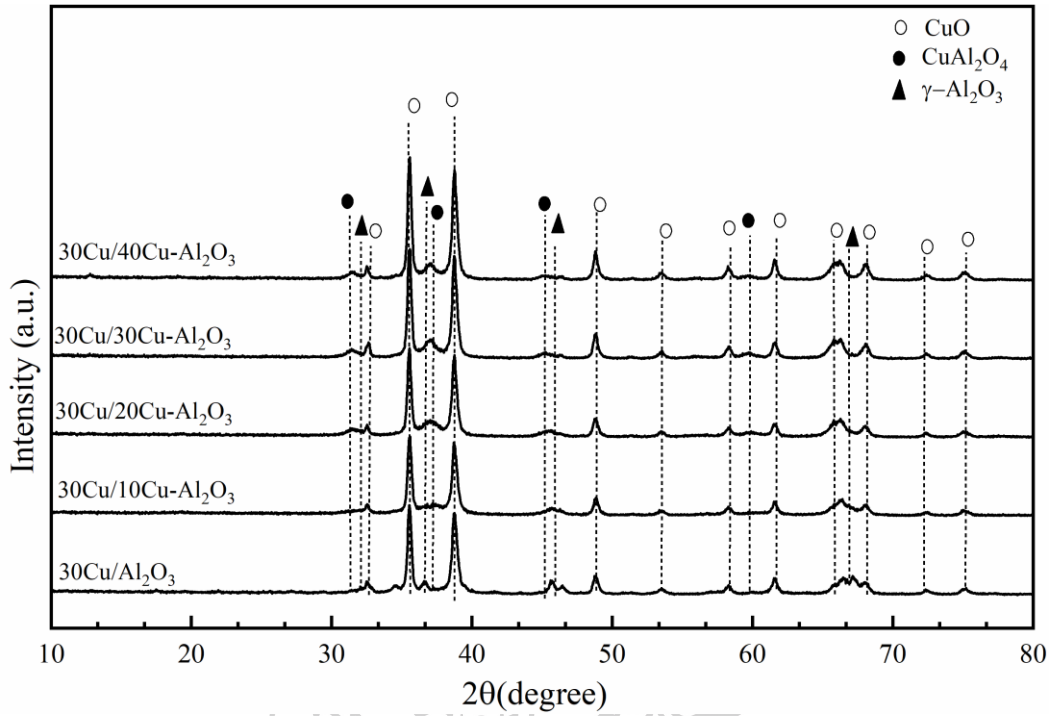

Figure 20 The XRD pattern of 30Cu/xCu-Al_2O_3 (x = 0, 10, 20, 30, and 40 wt% Cu) catalyst.

Table 4 The crystalline size of copper oxide from XRD results.

Catalysts	CuO crystalline size (nm)
10Cu-Al_2O_3	n.d.
20Cu-Al_2O_3	15.3
30Cu-Al_2O_3	15.9
40Cu-Al_2O_3	18.2
30Cu/Al_2O_3	26.2
30Cu/10Cu-Al_2O_3	23.4
30Cu/20Cu-Al_2O_3	27.0
30Cu/30Cu-Al_2O_3	29.2
30Cu/40Cu-Al_2O_3	32.6

5.1.2 The BET surface area and pore characteristics of catalyst

The BET surface area, and total pore volume of catalysts were characterized using N_2 adsorption/desorption measurement (BEL SORP MINI). These results shown in table 5. The BET surface area, and total pore volume of alumina (Al_2O_3) produced by FSP were 37 m^2/g, and 0.11 cm^3/g respectively. The BET surface area was increased when added amount of Cu (x = 10, 20, and 30 wt%) incorporated with Al_2O_3 in FSP step compare with Al_2O_3 without Cu inserting, increase to 94, 66 and 42 m^2/g for 10Cu-Al_2O_3, 20Cu-Al_2O_3 and 30Cu-Al_2O_3, respectively. These indicated that Cu incorporated during in FSP disturbed the formation of Al_2O_3 by Cu dopant might be inhibit growth of Al_2O_3 particles resulting in the increasing surface area and smaller particle size, as agreement with metal dopants of catalyst synthesis through the FSP method (92, 95, 96). However, the higher Cu inserting was lower the BET surface area than smaller Cu inserting, due to a high amount of Cu was formed into large CuO particle size in FSP that was related to poor surface area. For 40Cu-Al_2O_3 the BET surface area, and pore volume were similar Al_2O_3. Addition of 30 wt% Cu on FSP-made Cu-Al_2O_3 via incipient wetness impregnation method apparently decreased the BET surface area, and the pore volume of catalysts. It can be attributed to blocking pore of copper according with the literature (97).

The N_2 adsorption/desorption isotherm of samples were shown in Figure 21 (a and b) All of isotherms presented hysteresis loop indicating the appearance of opened or closed pores. The hysteresis loop of all samples displayed H3-type according to IUPAC classification of adsorption isotherms that were characteristic of aggregates of plate-like particles or slit-shaped pores (98, 99).

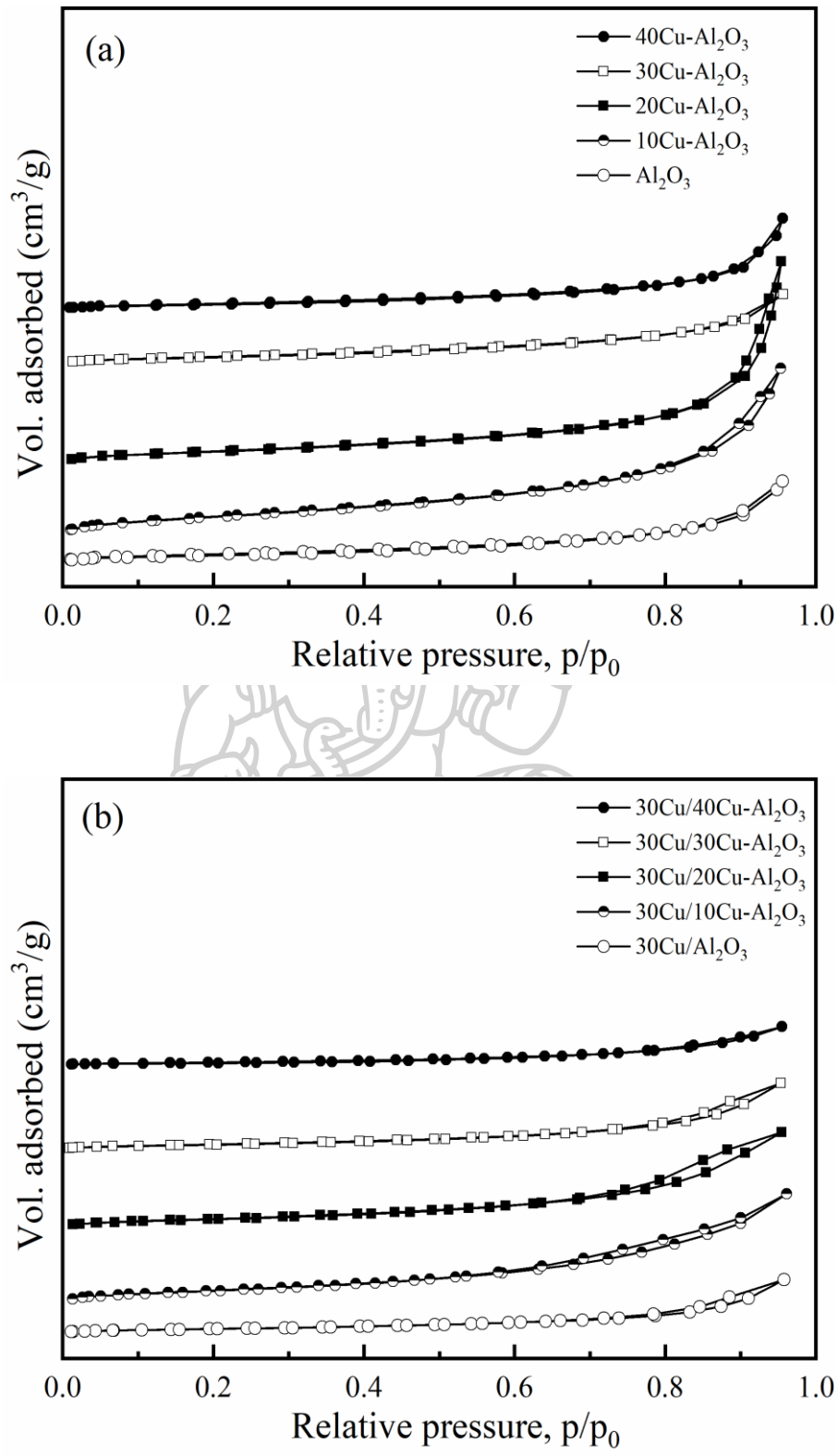

Figure 21 The N_2 adsorption/desorption isotherms: (a) the FSP-made xCu-Al_2O_3, (x = 0, 10, 20, 30, and 40 wt% Cu), (b) 30Cu/xCu-Al_2O_3 (x = 0, 10, 20, 30, and 40 wt% Cu) catalyst.

Table 5 The BET surface area and total pore volume of catalyst.

Samples	BET surface area (m^2/g)	Total pore volume(cm^3/g)
Al_2O_3	37	0.11
10Cu-Al_2O_3	94	0.24
20Cu-Al_2O_3	66	0.28
30Cu-Al_2O_3	42	0.11
40Cu-Al_2O_3	33	0.13
30Cu/Al_2O_3	19	0.07
30Cu/10Cu-Al_2O_3	56	0.14
30Cu/20Cu-Al_2O_3	41	0.12
30Cu/30Cu-Al_2O_3	25	0.09
30Cu/40Cu-Al_2O_3	17	0.05

5.2 The chemical properties of Cu inserted on copper-based catalysts

5.2.1 Reduction behavior of catalyst by temperature programed reduction (TPR)

The reduction behavior and phase species of heterogeneous catalysts were characterized by temperature programmed reduction (TPR). The TPR profile of copper oxide bulk was shown in Figure 22. The CuO bulk was reduced in the temperature range 240 to 480 ºC. The first reduction peak was 320 ºC and the second reduction peak was 445 ºC. The reduction of copper oxide has two possible hypotheses. The CuO was directly reduced by hydrogen to Cu metal without the formation of intermediate species (Cu_2O, Cu_4O_3) as follows equation 1:

Single step: $CuO+H_2 \rightarrow Cu+H_2O$ — 1

The copper oxide (CuO) was reduced via two steps of reduction from CuO to Cu_2O and Cu_2O to Cu metal. The following equations were designated:

1st step: $2CuO+H_2 \rightarrow Cu_2O+H_2O$ — 2

2nd step: $Cu_2O+H_2 \rightarrow 2Cu+H_2O$ — 3

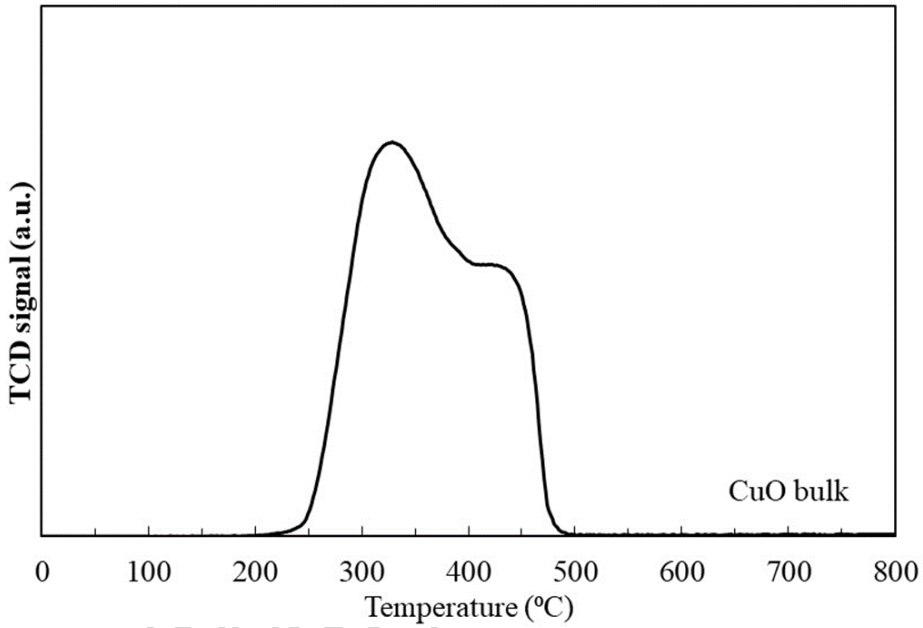

Figure 22 H_2-TPR patterns of the copper oxide bulk.

The reduction characteristics of x$Cu-Al_2O_3$ (x= 10, 20, 30, and 40 wt%) samples with different amounts of copper loading were shown in Figure 23 TPR patterns can be deconvoluted to two regions, the first region of reduction temperature peak at 150-400 ºC assigned α region. It was attributed that overlap of two reduction stages of $CuO \rightarrow Cu_2O$ and then $Cu_2O \rightarrow$Cu metal/weak interaction of copper oxide with alumina. When increasing copper loading, the hydrogen consumption in α regions increased that related to increasing the amount of copper oxide on the surface. Moreover, the α peak shifted to higher temperature with increasing copper loading due to larger copper oxide size embedded in Al_2O_3 support as showed in CuO crystalline size from XRD results. For the second region at 400-800 ºC assigned β region, the two-reduction peak can be observed. the presence of β_1 peak at 400-600 ºC, β_2 peak at 600-800 ºC indicated that there was medium/strong interaction of copper oxide particles and Al_2O_3 support. It was suggested that reduction of $CuAl_2O_4$ spinel structure which was found in XRD results (as shown in Figure 19). The $CuAl_2O_4$ species can be reduced at high

temperature range of 500-800 ºC (100). Which $CuAl_2O_4$ was formed during FSP process at high temperature. The results of reducibility and reducibility of α peak, β peak from total reducibility of all samples were exhibited in Table 6. The increasing amount of inserted copper with alumina during FSP process from 10 to 40 wt% showed a higher ratio of α/β from 0.8 to 5.4. Where the α peaks were the reduction of CuO weak interaction with Al_2O_3 and β peaks were the reduction of CuO strong interaction with Al_2O_3 like $CuAl_2O_4$. The strong interaction of CuO with a surface of Al_2O_3 ratios (etc. $CuO\text{-}Al_2O_3$, $CuAl_2O_4$) decreased with an increasing amount of copper.

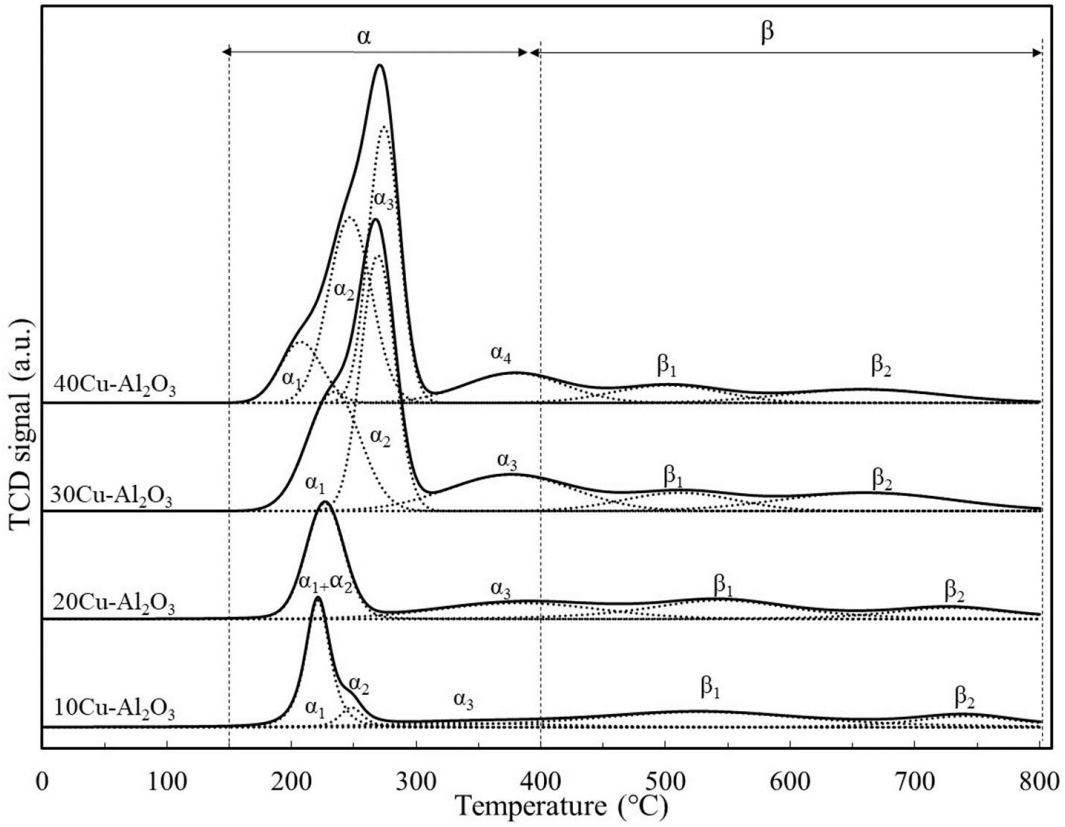

Figure 23 H_2-TPR patterns of the FSP-made $xCu\text{-}Al_2O_3$, (x = 0, 10, 20, 30, and 40 wt% Cu).

Table 6 Results form H_2-TPR profiles.

Samples	DOR of α peak (%)				Total α	DOR of β peak (%)		Total β	Ratio of α/β	Total DOR (%)
	α_1	α_2	α_3	α_4		β_1	β_2			
10Cu-Al_2O_3	30	6	0	9	45	41	15	55	0.8	71
20Cu-Al_2O_3	37	0	0	22	60	27	13	40	1.5	59
30Cu-Al_2O_3	25	35	0	18	79	8	13	21	3.7	70
40Cu-Al_2O_3	10	30	33	11	84	7	8	16	5.4	56
30Cu/Al_2O_3	7	88	5	0	100	0	0	0	-	61
30Cu/10Cu-Al_2O_3	8	31	31	13	82	14	3	18	4.6	59
30Cu/20Cu-Al_2O_3	10	29	18	22	79	16	5	21	3.8	53
30Cu/30Cu-Al_2O_3	3	70	8	0	82	11	7	18	4.6	50
30Cu/40Cu-Al_2O_3	3	15	33	36	77	4	9	13	5.9	50

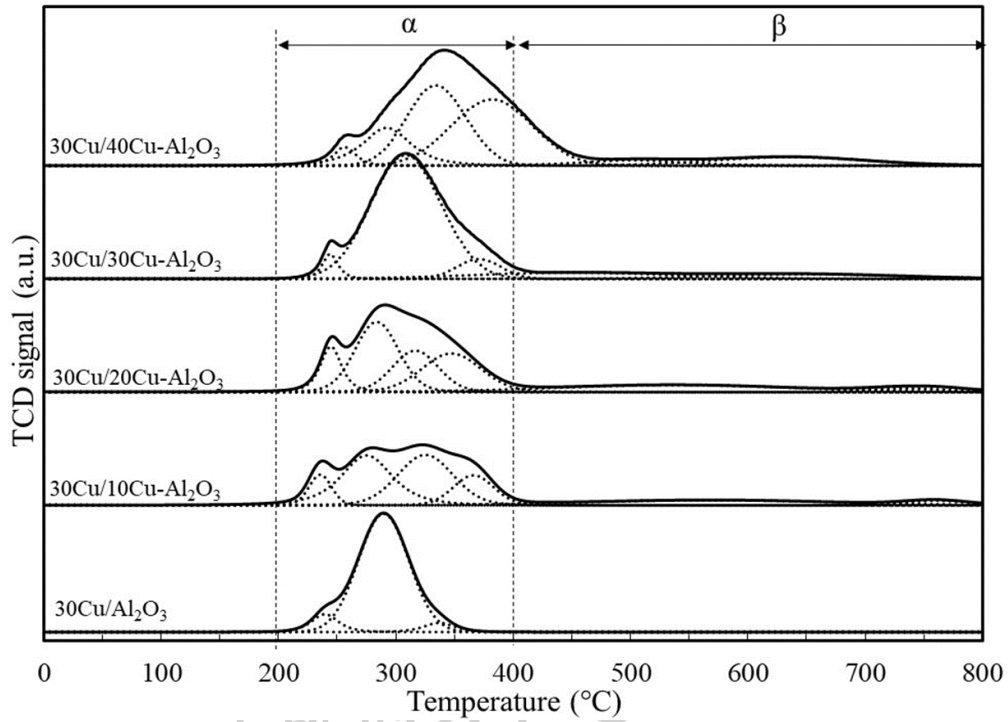

Figure 24 H_2-TPR patterns of the 30Cu/xCu-Al_2O_3 (x= 0, 10, 20, 30, and 40 wt% Cu) catalysts.

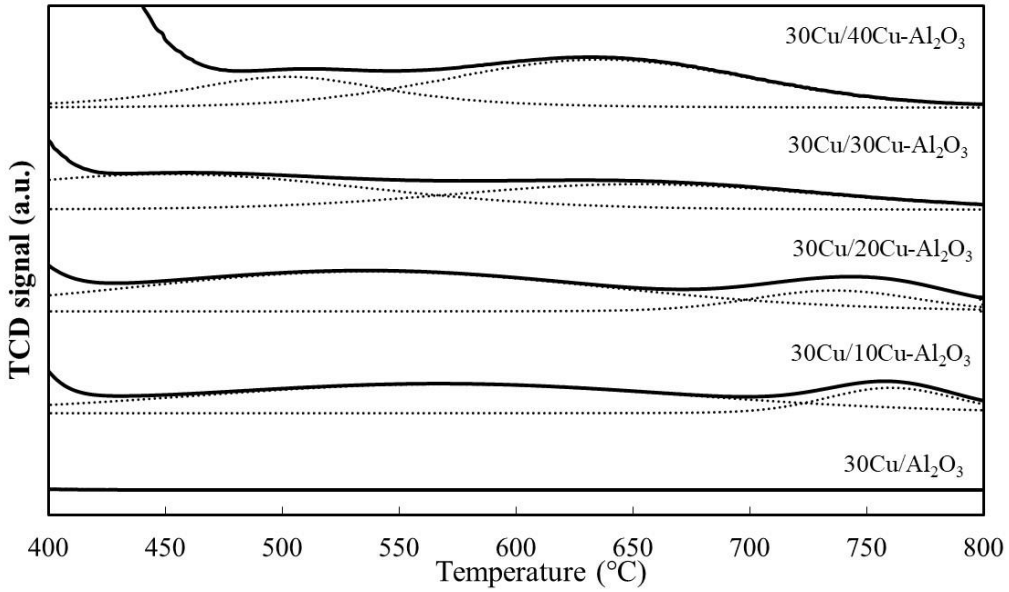

Figure 25 TPR patterns of the 30Cu/xCu-Al_2O_3 (x= 0, 10, 20, 30, and 40 wt% Cu) at temperature in a range 400 to 800 ºC.

Figure 24 shows the TPR profiles of the 30Cu/xCu-Al_2O_3 (x = 0, 10, 20, 30, and 40 wt%) catalysts prepared by FSP. The 30Cu/Al_2O_3 catalyst presented the main reduction peak at about 290 ºC and small reduction peak at about 240 ºC, which were attributed to the reduction of CuO to metallic copper (CuO→Cu_2O→Cu). When the addition of 10 wt% Cu incorporated with Al_2O_3 in FSP step, the TPR profiles showed board reduction temperature peaks in a range 220-400 ºC. It can be suggested that there were many particle sizes of CuO on support. The main reduction peak shifted to a higher temperature. The results were possible that the reduction of the strong interaction between CuO and Al_2O_3 from FSP preparing process. For addition 20 wt% of Cu, the position of α_3 peak shifted toward lower temperature as compared to addition 10wt% of Cu. The TPR profiles of 30 and 40 wt% of Cu incorporated with Al_2O_3 were rather similar that appear two main peaks. When increasing Cu with Al_2O_3 during FSP step, the area of H_2 consumption increased which relate to the amount of CuO reduction on Al_2O_3. And the positions of reduction peak were shifted towards higher temperature with increasing copper loading. It was indicated that the copper particle sizes were larger. The large copper particle sizes were more difficult to reduce than smaller copper particle size. Furthermore, the reduction peak at high temperature in a range of 400-800 ºC was still remaining observed for addition of Cu in FSP catalysts as presented Figure 25, while these peaks disappear in TPR profile of 30Cu/Al_2O_3

The comparison of TPR profiles of 30Cu/40Cu-Al_2O_3 fresh catalyst and pretreated catalyst at 300 ºC under H_2 ambient flow for 3 h were shown in Figure 26. The reduction peak starts 320 ºC to 800 ºC and hydrogen consumption peaks were invisible below 320 ºC. These results show that at reduction temperature of 300 ºC, 3 h was enough to assure copper oxide could be reduced to their metallic.

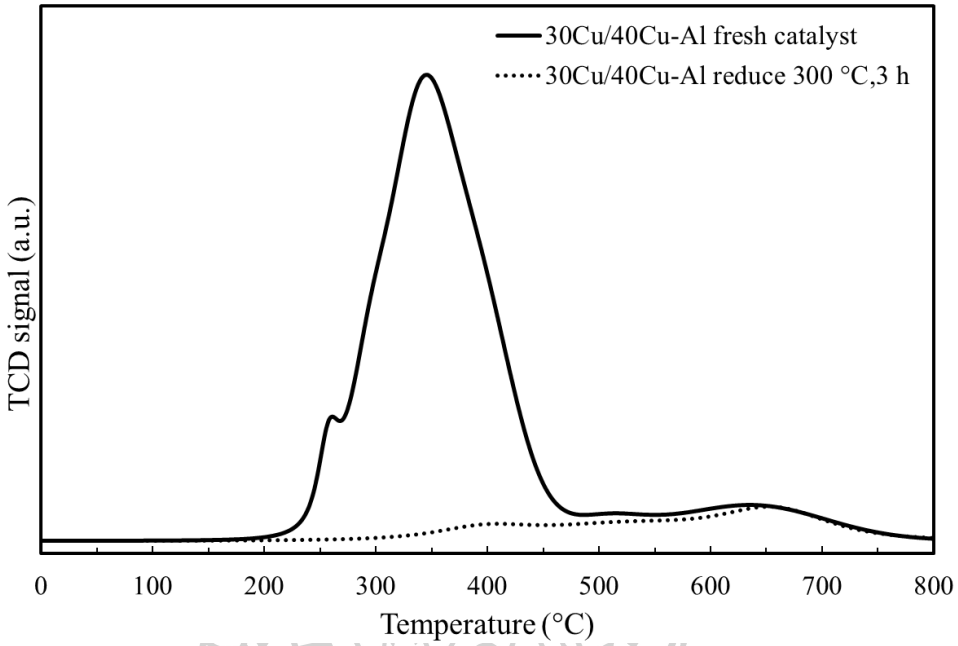

Figure 26 Comparison of the TPR profiles of fresh and pretreated catalyst in H_2, 300 ºC, 3 h for 30Cu/40Cu-Al_2O_3 catalyst.

5.2.2 The copper metallic sites by N_2O decomposition

The copper surface area on catalyst was measured by N_2O decomposition as a probe molecule. The molecules of N_2O adsorbed on copper surface was decomposed to nitrogen and chemisorbed oxygen atom, and then the copper surface was covered with oxygen species according to reaction ($N_2O+2Cu_s \rightarrow (Cu_s - O - Cu_s) + N_2$). The Cu_s is a declarative copper surface atom and assumption adsorption stoichiometry is 2 :1 for $Cu_s : O_{ads}$. (101).

The N_2O decomposition result of 30Cu/xAl_2O_3 with difference amount of Cu inserted in FSP step were shown in Figure 27 (a). For the 30Cu/Al_2O3 as without Cu inserting displayed the lowest copper active site. While the 30Cu/10Cu-Al_2O_3 exhibited the highest copper active site. Because the copper particles were easily reconstruction and well dispersed to small copper metallic size on 10Cu-Al_2O_3 support, as the 10Cu-Al_2O_3 show the highest BET surface area and the smallest CuO crystalline size (as shown in Figure 27 (b)). With increasing Cu inserted, the copper active site decreased due to the large CuO particle size.

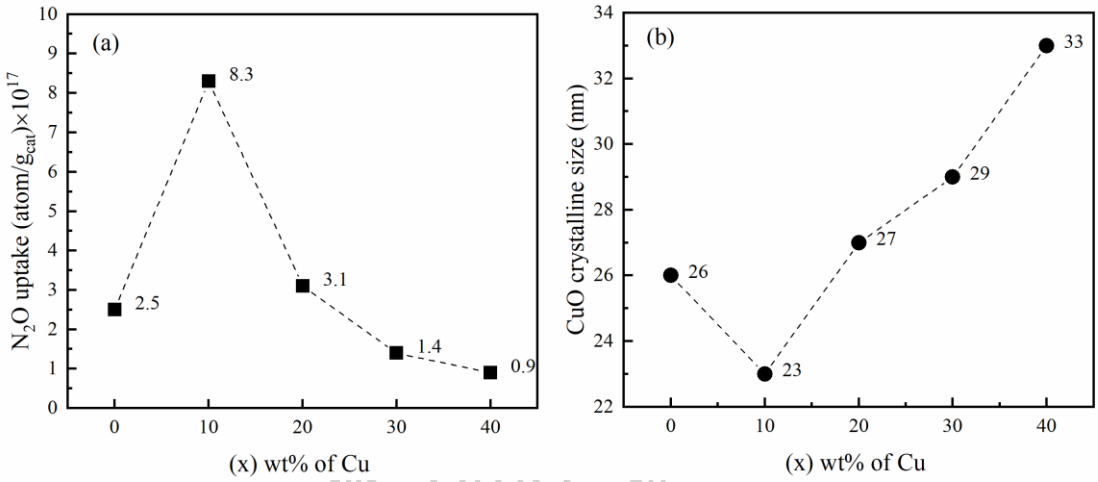

Figure 27 (a) N_2O decomposition results of 30Cu/xCu-Al_2O_3 (x = 0, 10, 20, 30, and 40 wt%), (b) crystallite size of CuO of 30Cu/xCu-Al_2O_3 (x = 0, 10, 20, 30, and 40 wt%).

5.3 Catalytic performance of Cu inserted on copper-based catalysts in glycerol hydrogenolysis

Activity and selectivity of catalysts were tested by glycerol hydrogenolysis reaction. The results and discussion consist two pasts. First, the effect of Cu inserted on Cu/Al_2O_3 (30Cu/xCu-Al_2O_3, x= 10, 20, 30, and 40 wt% Cu) by FSP method and the effect of Cu content between impregnation and incorporation with Al_2O_3 (total copper loading on catalyst as 30 wt% Cu).

5.3.1 Activity and selectivity of 30Cu/xCu-Al_2O_3 x= 10, 20, 30, and 40 wt% Cu)

Figure 28 shows the activity of 30Cu/xCu-Al_2O_3 (x= 10, 20, 30, and 40 wt% Cu) catalyst. The glycerol conversion based on total liquid phase products. In this work, all of the catalysts used presented low conversion. The 30Cu/Al_2O_3 showed 7% of glycerol conversion and 42 % of 1,2-PDO. With inserting of 10 to 30 wt% of Cu by FSP method, the glycerol conversion hardly changed. While inserting of 40 wt% of Cu showed the lowest glycerol conversion because of larger copper particle. The glycerol

adsorption can occur on metal surface, alloy surface and metal oxide surface. This was possible that the glycerol molecules liked to adsorb on metal surface than $CuAl_2O_4$ surface. Therefore, the metal surface was covered by glycerol molecules, there was not enough metal surface to hydrogen adsorption resulting in a high acetol and low 1,2-PDO selectivity. Considering the obtained product, the 30Cu/10Cu-Al_2O_3 exhibited the highest selectivity of 1,2-PDO (62%) due to was high metallic Cu active sites that the Cu metal was selective cleavage between C-O bonds. However, the role of copper aluminate ($CuAl_2O_4$) on 30Cu/xCu-Al_2O_3 is unclear, owing to the total amount of Cu content in catalyst also affect to activity for glycerol hydrogenolysis reaction. Then, the aCu/bCu-Al_2O_3 (a+b = 30 wt% Cu) catalysts were investigated, which the Cu supported on Al_2O_3 catalysts were synthesized by merging of two techniques. There are impregnation and flame spray pyrolysis (FSP).

The activity and selectivity for aCu/bCu-Al_2O_3 catalysts were shown in Figure 29. The addition of incorporated copper with alumina increased the glycerol conversion and the selectivity of acetol, which the 15Cu/15Cu-Al_2O_3 presented the highest selectivity of acetol. It well know that the acid surface responsible for glycerol dehydration into acetol, and metal surface responsible for hydrogenation into 1,2-PDO (102). Therefore, the FSP-inserted Cu on Al_2O_3 exhibited a key in glycerol dehydration step, which generated acetol.

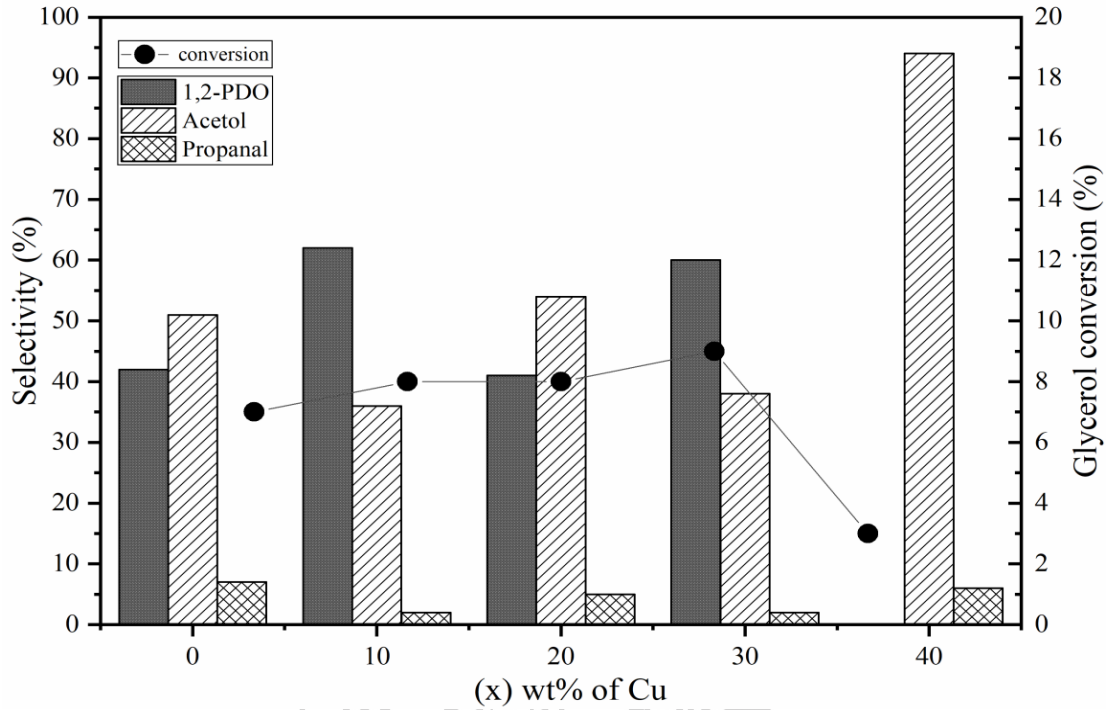

Figure 28 The activity and selectivity of the 30Cu/xCu-Al_2O_3, (x= 0, 10, 20, 30, and 40 wt% Cu) catalyst.

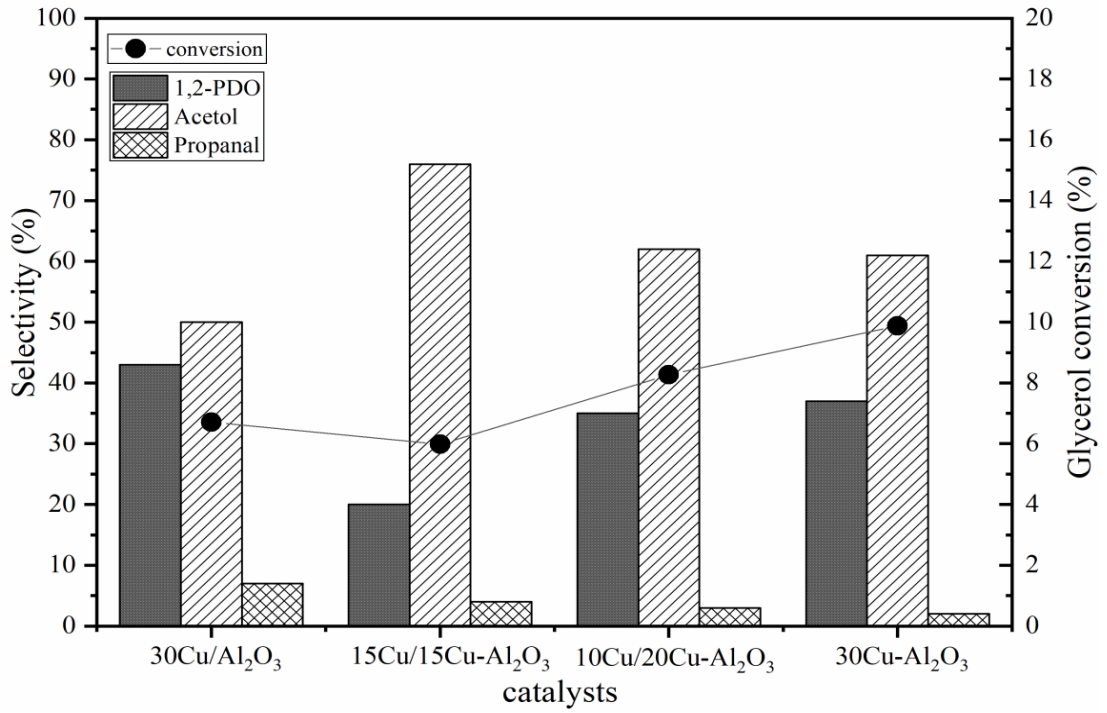

Figure 29 The activity and selectivity of the aCu/bCu-Al_2O_3 (a+b = 30 wt% Cu) catalyst.

5.4 Conclusions

The inserting Cu on 30Cu/Al_2O_3 via FSP method with different Cu loading for glycerol hydrogenolysis reaction was studied. The incorporation of Cu and Al_2O_3 (Cu-Al_2O_3) during the FSP process produced both CuO and $CuAl_2O_4$ spinel phase. The impregnated Cu on the FSP-made Al_2O_3 only observed the CuO phase. Therefore, the $CuAl_2O_4$ was especially found FSP catalyst. In addition, addition Cu with Al_2O_3 during FSP can be inhibited the growth of Al_2O_3 particle as a result high BET surface area. A high amount of Cu loading in FSP has significantly the decreasing interaction between copper oxide and alumina support. The 30Cu/10Cu-Al_2O_3 showed the highest selectivity of 1,2-PDO due to a high active site and the presence of small metallic copper. The 30Cu/40Cu-Al_2O_3 did not detected 1,2 PDO product because of the lowest metal surface to hydrogenation step. The Cu metal was an important factor to produced 1,2-PDO.

มหาวิทยาลัยศิลปากร

CHAPTER VI

ROLE OF ZINC ALUMINATE SPINEL SUPPORT ON COPPER-BASED CATALYST FOR HYDROGENOLYSIS OF GLYCEROL TO 1,2 PROPANEDIOL

6.1 The physical properties of Zn inserted on copper-based catalysts

6.1.1 The phase analysis by X-ray diffraction (XRD)

The XRD diffraction patterns of the FSP-made Zn-Al_2O_3 with different amount of Zn loading were presented in Figure 30. All the diffraction peak of FSP-made Zn-Al_2O_3 exhibited $ZnAl_2O_4$ spinel phase, the diffraction peak at 2θ of 31.36º, 36.83º, 44.85º, 48.97º, 55,52º, and 59.38º according to the characteristic reflection (220), (311), (400), (311), (422), (511), and (440) planes of cubic $ZnAl_2O_4$ spinel structure (103). The diffraction peak at 31.80º, 34.45º, 36.30º, 47.58º, 56.63º, 62.83º, 67.98º, and 69.10º assigned to ZnO, which corresponding to the reflection forms (100), (002), (101), (102), (110), (103), (112), and (201) diffraction planes(104, 105). The diffraction peaks of γ-Al_2O_3 were also found, the peak at 2θ of 32.0º, 37.0º, 45.8º, and 66.5º. The diffraction peak of $ZnAl_2O_4$ spinel and ZnO were shaper and higher intensity with increasing amount of Zn. This indicated that obtained $ZnAl_2O_4$ and ZnO have high crystallinity, and large crystallite size.

Figure 31 presents the XRD pattern of 30Cu/Al_2O_3 and 30Cu/xZn-Al_2O_3 (x= 0, 10, 20, 30, and 40 wt% Zn) catalysts. The diffraction peaks of CuO were observed on all of catalyst. The CuO crystallite size of catalyst were in range of 23-26 nm. Adding of Zn in FSP do not significantly affect crystallite size of CuO**.** The crystalline size of CuO was determined from XRD data following to the Scherrer's equation was listed in Table 7

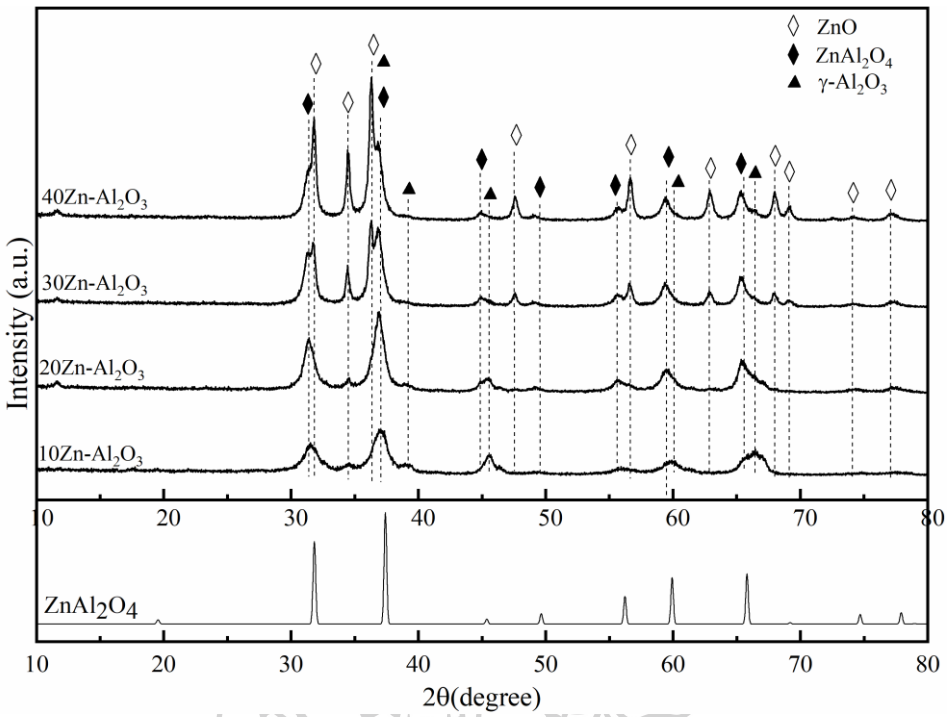

Figure 30 The XRD pattern of the FSP-inserted Zn (xZn-Al_2O_3, x = 0, 10, 20, 30, and 40 wt% Zn).

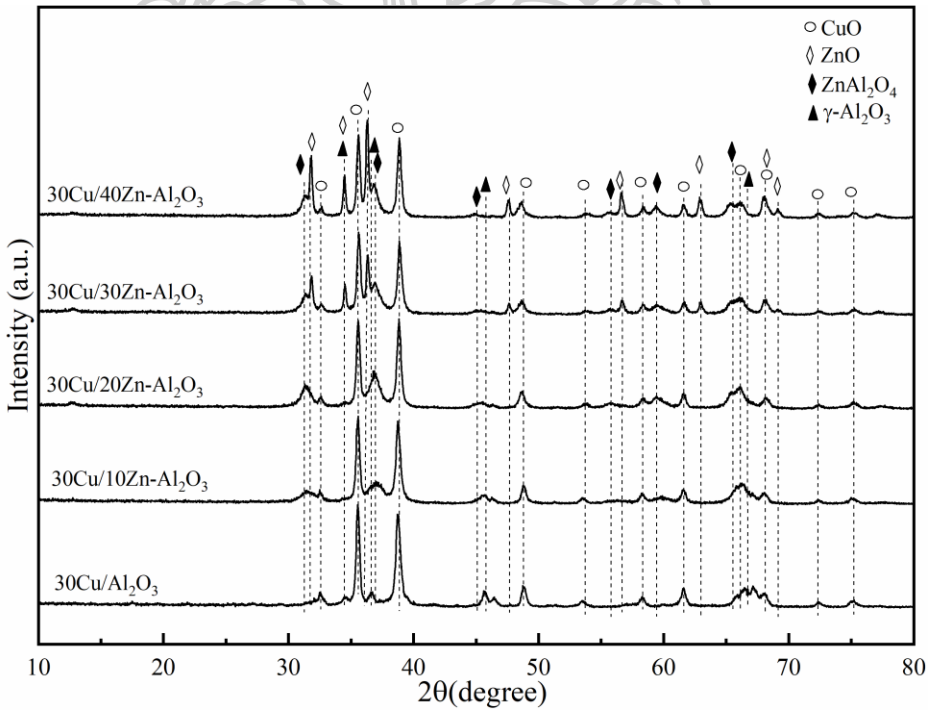

Figure 31 The XRD pattern of 30Cu/xZn-Al_2O_3 (x = 0, 10, 20, 30, and 40 wt% Zn) catalyst.

Table 7 The crystalline size of copper oxide on the FSP-made Zn-Al_2O_3 from XRD results.

Catalysts	CuO crystalline size (nm)
30Cu/Al_2O_3	26.2
30Cu/10Zn-Al_2O_3	23.4
30Cu/20Zn-Al_2O_3	24.3
30Cu/30Zn-Al_2O_3	25.8
30Cu/40Zn-Al_2O_3	24.0

6.1.2 The BET surface area and pore characteristics of catalyst

The BET surface area, and total pore volume of xZn-Al_2O_3 and 30Cu/xZn-Al_2O_3 (x= 10, 20, 30, 40 wt%) catalysts were shown in table 8. The BET surface area and total pore volume of alumina flame made were 37 m^2/g and 0.11 cm^3/g, respectively. The BET surface area of addition Zn with Al_2O_3 in FSP process, increases to 68, 70, 66 and 50 m^2/g for 10Zn-Al_2O_3, 20Zn-Al_2O_3, 30Zn-Al_2O_3 and 40Zn-Al_2O_3, respectively, compared with pure Al_2O_3. It suggested that Zn incorporated during in FSP disturbed the formation of Al_2O_3 by Zn dopant might be inhibit growth of Al_2O_3 particles, which is same case inserted Cu. However, the increasing amount of Zn influences the decreased BET surface area.

The N_2 adsorption/desorption isotherm of catalyst were shown in Figure 32 (a and b). All of catalyst presented H3-type of hysteresis loop, this hysteresis loop type was characteristic of aggregates of plate-like particles or slit-shaped pores. Moreover, the closure point of hysteresis loop was appeared at the relative pressure about 0.87 for all of catalysts, which was the presence mesoporous materials.

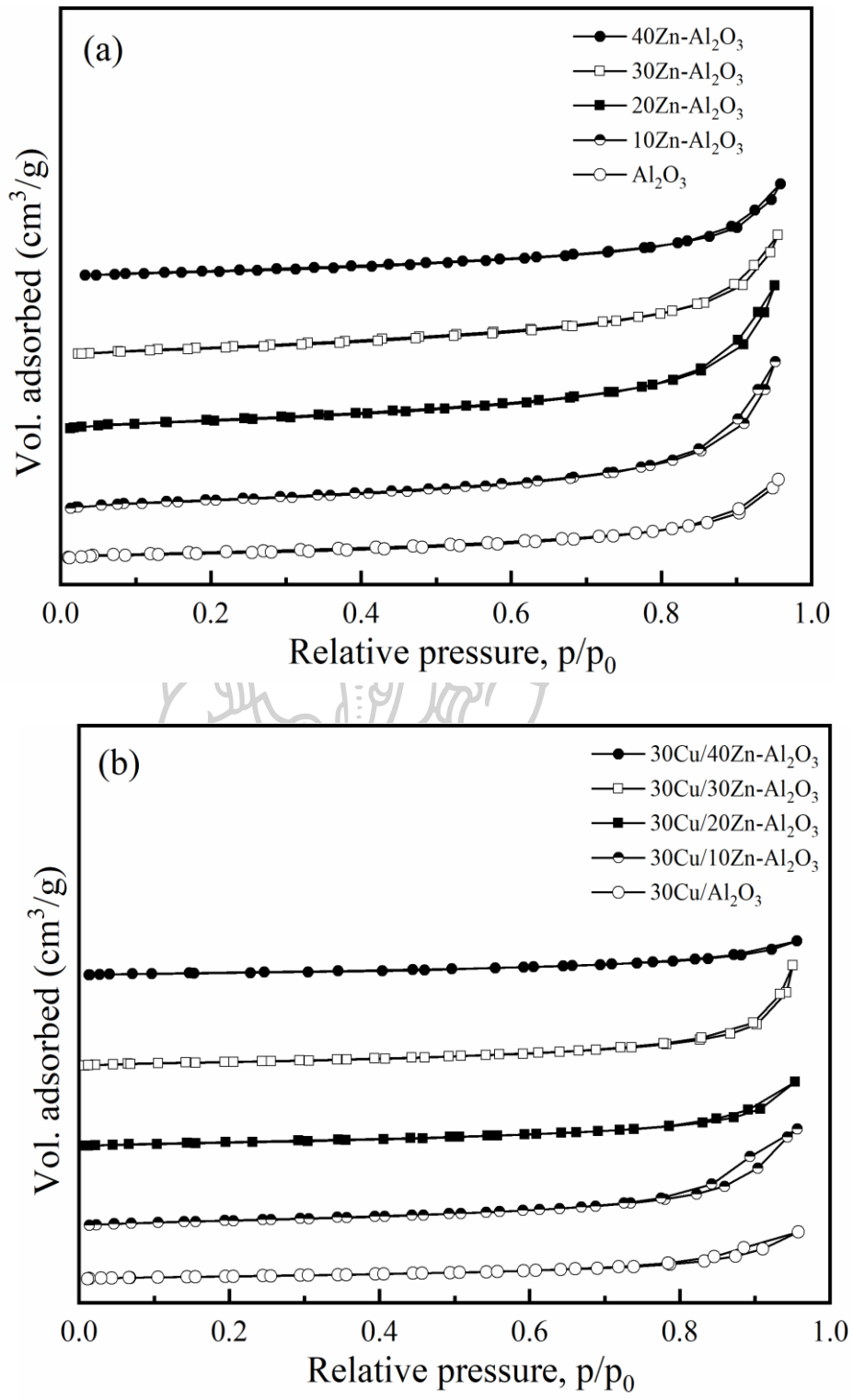

Figure 32 The N_2 adsorption/desorption isotherms: (a) the FSP-made xZn-Al_2O_3, (x = 0, 10, 20, 30, and 40 wt% Zn), (b) 30Cu/xZn-Al_2O_3 (x = 0, 10, 20, 30, and 40 wt% Zn) catalyst.

Table 8 The BET surface area and total pore volume of catalyst.

Samples	BET surface area (m^2/g)	Total pore volume(cm^3/g)
Al_2O_3	37	0.11
10Zn-Al_2O_3	68	0.22
20Zn-Al_2O_3	70	0.21
30Zn-Al_2O_3	66	0.18
40Zn-Al_2O_3	50	0.14
30Cu/Al_2O_3	19	0.07
30Cu/10Zn-Al_2O_3	37	0.14
30Cu/20Zn-Al_2O_3	29	0.10
30Cu/30Zn-Al_2O_3	29	0.14
30Cu/40Zn-Al_2O_3	19	0.05

6.2 The chemical properties of Zn inserted on copper-based catalysts

6.2.1 Reduction behavior of catalyst by temperature programed reduction (TPR)

The reduction characteristics of the copper oxide bulk, zinc oxide bulk, and 30Cu/xZn-Al_2O_3 catalysts were shown in Figure 33 and Figure 34, respectively. The CuO bulk was reduced in the temperature range 250-480ºC which related two stages of the CuO reduction process ($CuO \rightarrow Cu_2O \rightarrow Cu^0$). The reduction peak of ZnO bulk appeared the tiny hill peak of hydrogen consumption in TPR profile. This was indicated that the ZnO was a disabled reduction to zinc metal at temperature below 800 ºC. Then, the reduction of ZnO can be ignored compared with reduction of CuO.

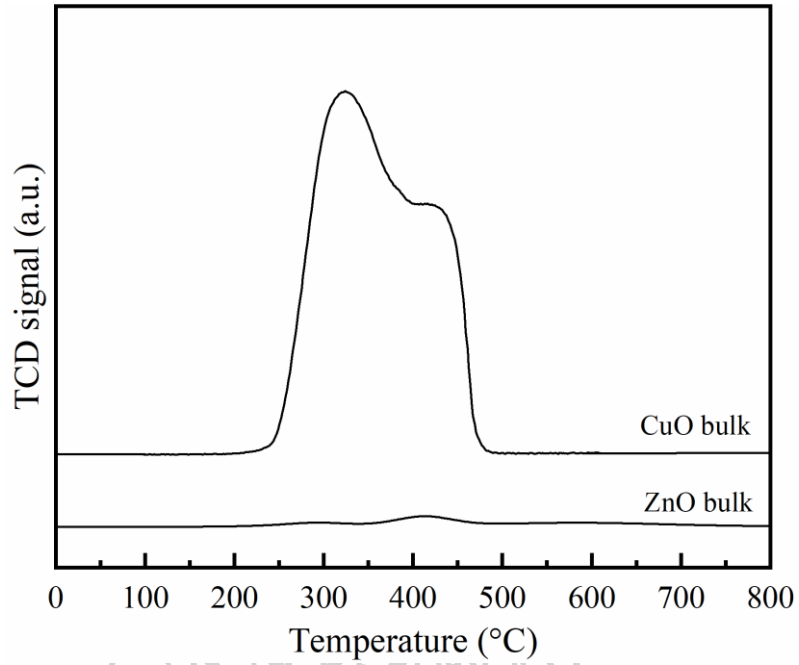

Figure 33 H_2-TPR patterns of the copper oxide and zinc oxide bulk.

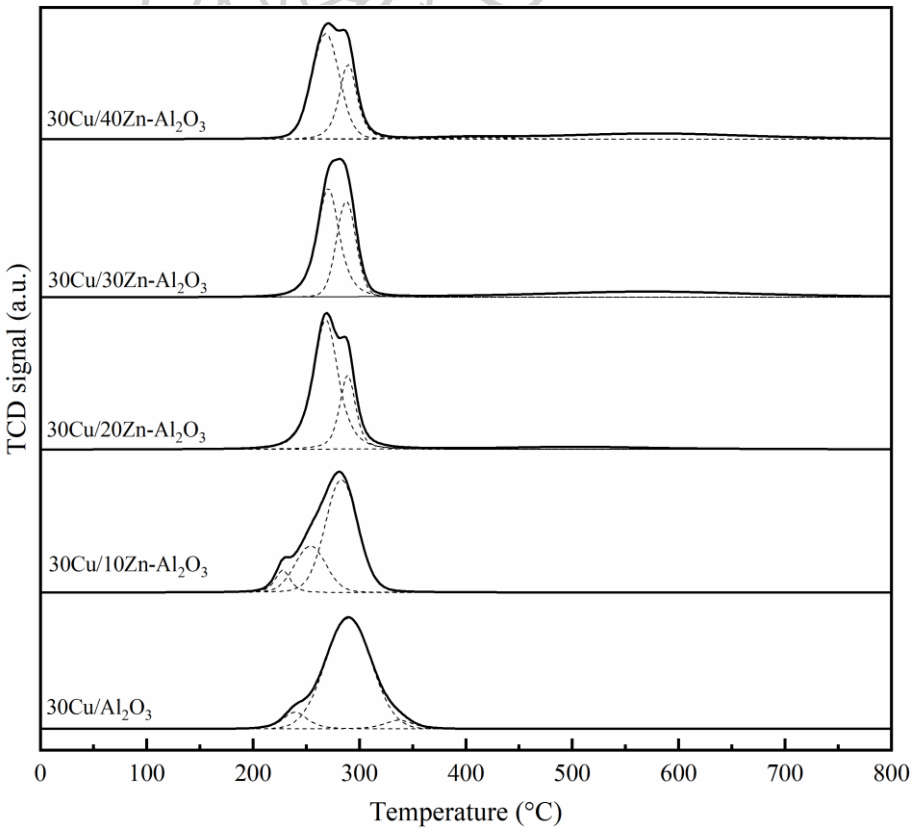

Figure 34 H_2-TPR patterns of the 30Cu/xZn-Al_2O_3 (x= 0, 10, 20, 30, and 40 wt% Zn) catalyst.

The reduction temperature peaks of 30Cu/Al_2O_3 and 30Cu/10Zn-Al_2O_3 catalysts were rather similar trends that two peaks were observed. The small reduction peak in a range of 220 ºC to 250 ºC. it can be assigned to the reduction of a small CuO size on the surface. The second peak at about 280 ºC assigned to the reduction peak of larger CuO particle size on support. When increasing Zn with Al_2O_3 during FSP step (Zn = 20, 30 and 40 wt %). It was found that the first reduction peak shifted to higher temperature from 250 to 270 ºC. while the position of the second peak hardly changed. This result can be suggested that the copper oxide particle was homogeneous surface like uniform particle sizes. The total reducibility of all catalyst estimated by the TPR data were shown in Figure 35. It is can be clearly observed that increasing the amount of zinc (20, 30 and 40 wt %) increased the reducibility of catalysts. This indicated that the presence Zn can improve CuO reducibility at the CuO/Zn-Al_2O_3 interface.

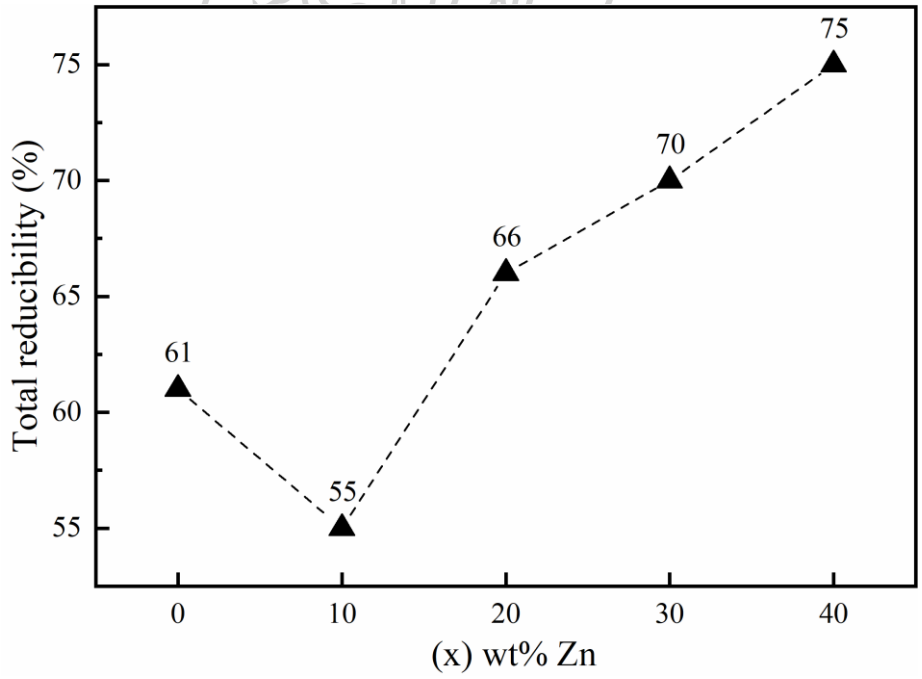

Figure 35 Total reducibility of 30Cu/xZn-Al_2O_3 (x = 0, 10, 20, 30, and 40 wt% Zn) catalyst.

6.2.2 The copper metallic sites by N_2O decomposition

The N_2O decomposition results of inserted Zn on Cu/Al_2O_3 catalyst were shown in Figure 36**.** For the catalyst without Zn, it found that the $30Cu/Al_2O_3$ presented the largest metallic copper diameter (37 nm), related to low copper active site. The inserting Zn of on Cu/Al_2O_3 catalyst can be increased the copper active site which the inserting Zn of 30 wt% exhibited the highest copper metal surface area due to the presence small copper metal size on catalyst. The obtained copper metal from reduction was smaller than the cobalt oxide size, this was implicit that the copper particles were facilely reconstruction and well dispersed on $ZnO\text{-}Al_2O_3$ surface during reduction process. The metallic copper was in a range of 2 to 8 nm 9 (as shown in Figure 36 (b)). For the $30Cu/Al_2O_3$ catalyst, the copper particles poor dispersed on low Al_2O_3 surface and reconstructed to large copper metal size. It should be noted that addition of Zn increased copper metal active sites.

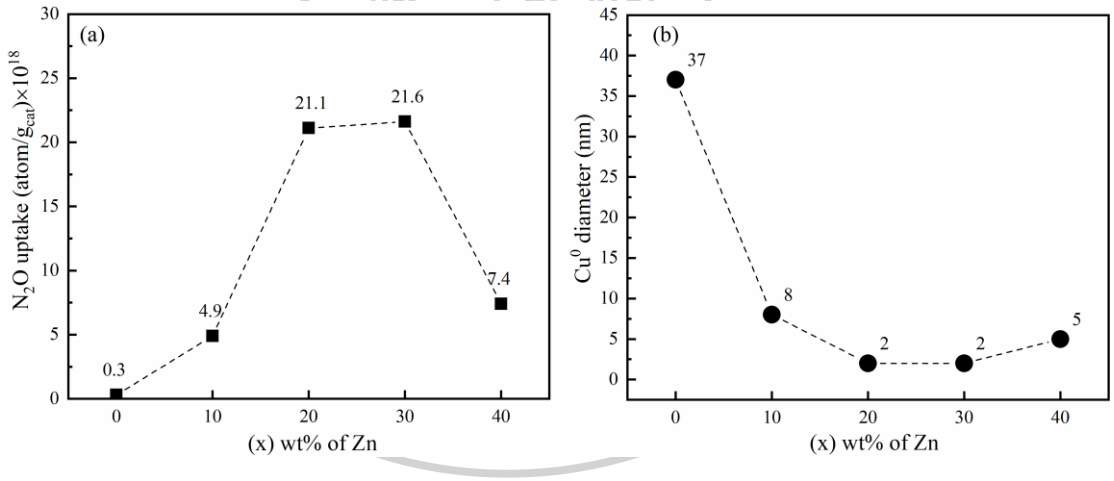

Figure 36 (a) N_2O decomposition results of $30Cu/xZn\text{-}Al_2O_3$ (x = 0, 10, 20, 30, and 40 wt% Zn), (b) diameter of copper metallic size of $30Cu/xZn\text{-}Al_2O_3$ (x = 0, 10, 20, 30, and 40 wt% Zn) catalyst.

6.3 Catalytic performance of Zn inserted on copper-based catalysts

Activity and selectivity of catalysts were test by glycerol hydrogenolysis reaction. The results and discussion consist two pasts. First, the effect of Zn inserted on Cu/Al_2O_3 ($30Cu/xZn\text{-}Al_2O_3$, x= 10, 20, 30, and 40 wt% Zn) by FSP method and the effect of reaction time at 3-12 h for glycerol hydrogenolysis.

6.3.1 Activity and selectivity of $30Cu/xZn\text{-}Al_2O_3$ x= 10, 20, 30, and 40 wt% Zn)

Figure 37 shows the glycerol hydrogenolysis activity and selectivity for $30Cu/xZn\text{-}Al_2O_3$, (x = 10, 20, 30, and 40 wt% Zn) catalysts. The inserting Zn can be slightly increased glycerol conversion and selectivity of 1,2-PDO, which the inserting Zn of 30 wt % displayed the highest for both glycerol conversion and 1,2-PDO selectivity. This result related to a high metallic copper active site on catalyst promoted catalytic activity and selectivity. The result was in agreement with Jiye Hu et al. (106) who reported that the activity and selectivity for glycerol hydrogenolysis were extremely relate to the particle size of Cu and Zn. These catalysts are bifunctional for glycerol selective hydrogenation to 1,2-PDO, the dehydration of glycerol to acetol over acid sites of ZnO, Al_2O_3, afterward acetol was hydrogenated to 1, 2-propanediol over Cu metal sites (dehydration-hydrogenation). Moreover, the inserting Zn can be decreased decomposition of 1,2-PDO to propanal. Nilsson M and coworker reported that the presence of $ZnAl_2O_4$ on catalyst decreased amount of acidity, which decreased Lewis acid sites on surface (107), leading to decreased active surface for decomposition of 1,2-PDO to propanal via dehydration step. Form glycerol hydrogenolysis result, the presence $ZnAl_2O_4$ on catalysts has a significantly positive effect on activity and selectivity of 1,2-PDO. Moreover, It well knows the $ZnAl_2O_4$ as a semiconductor that beneficial to transportation electron, resulting in high activity for adsorption of donor-type of H_2 (53).

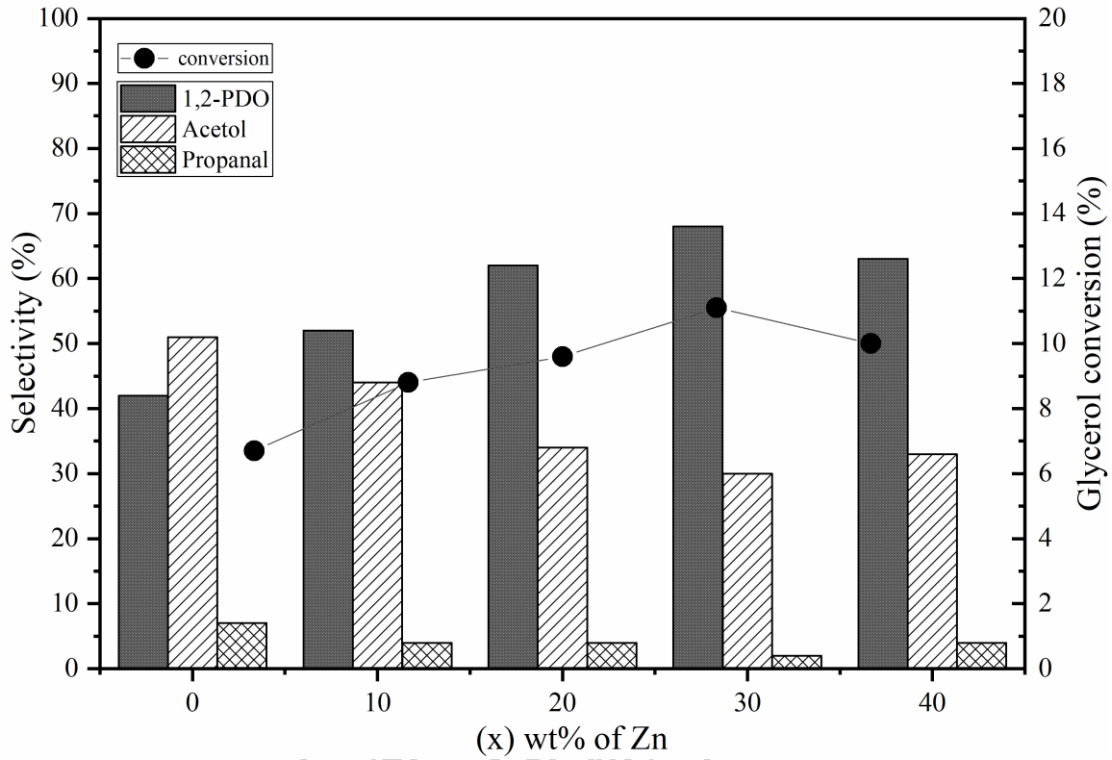

Figure 37 The activity and selectivity of the 30Cu/xZn-Al_2O_3, (x= 0, 10, 20, 30, and 40 wt% Zn) catalyst.

6.3.1 Effect of reaction time during the glycerol hydrogenolysis on 30Cu/30Zn-Al_2O_3 catalyst

The activity and selectivity of 30Cu/30Zn-Al_2O_3 with different reaction time from 1 to 9 h were shown Figure 38 and 30Cu/Al_2O_3 in reaction time 3 to 12 h showed in Figure 39 catalysts. For 30Cu/30Zn-Al_2O_3 catalyst, increasing the reaction time from 1 to 9 h resulted in increased glycerol conversion from 6 to 13%. The glycerol conversions were rather unchanged during 3 to 9 h, which indicated the obvious deactivation of catalyst. Previous work (21) reported that the Cu and ZnO crystallites can aggregated to large crystallites size during the reaction, leading to the loss in catalytic active site and glycerol conversion. The selectivity of 1,2PDO remain stable for a long time. C wang and coworker (108) noted that the 1,2-PDO was main product in glycerol hydrogenolysis on Cu-ZnO catalyst for water solvent. Because the water was easy the removal of 1,2-propanediol from catalyst surface, resulting in high selectivity of 1,2-PDO. In addition, the selectivity of propanal was 2 to 4 % during long

time. This result noted that the product is not decomposed during the long reaction time. Meanwhile, the $30Cu/Al_2O_3$ catalyst exhibit the decomposed product from 1,2-PDO during the long reaction time (as presented in Figure 39). This result confirmed that the presence of $ZnAl_2O_4$ can be reduce the decomposition of 1,2-PDO.

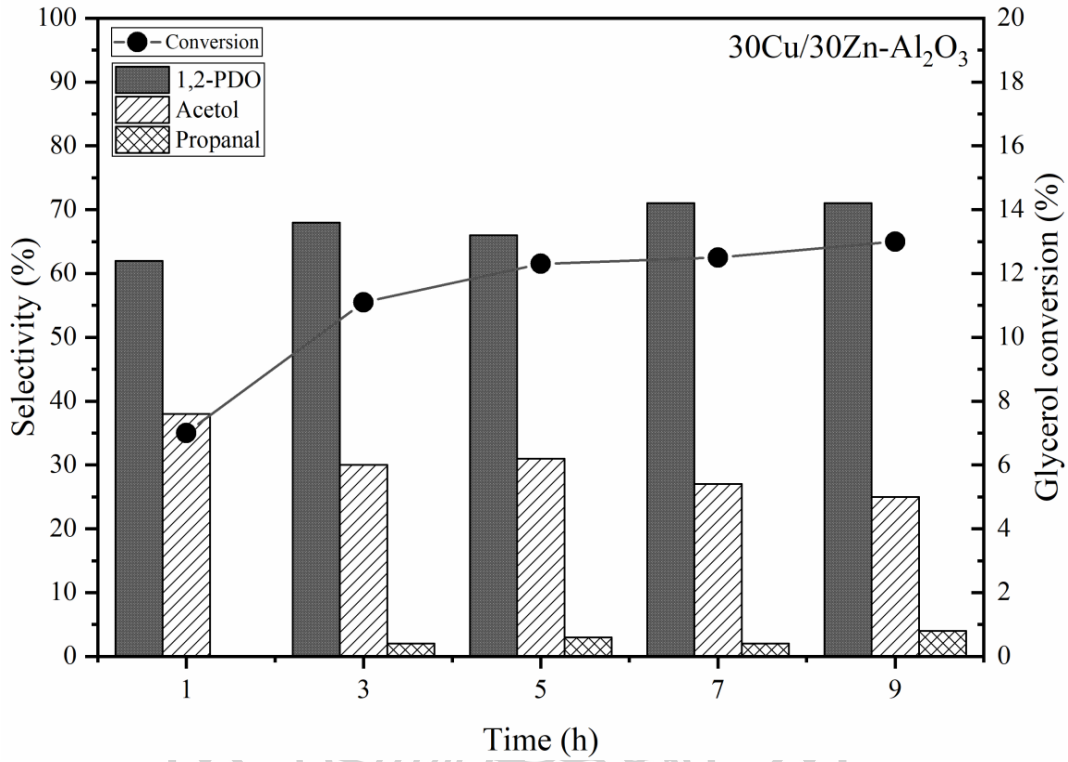

Figure 38 Effect of reaction time during the glycerol hydrogenolysis on $30Cu/30Zn-Al_2O_3$ catalyst.

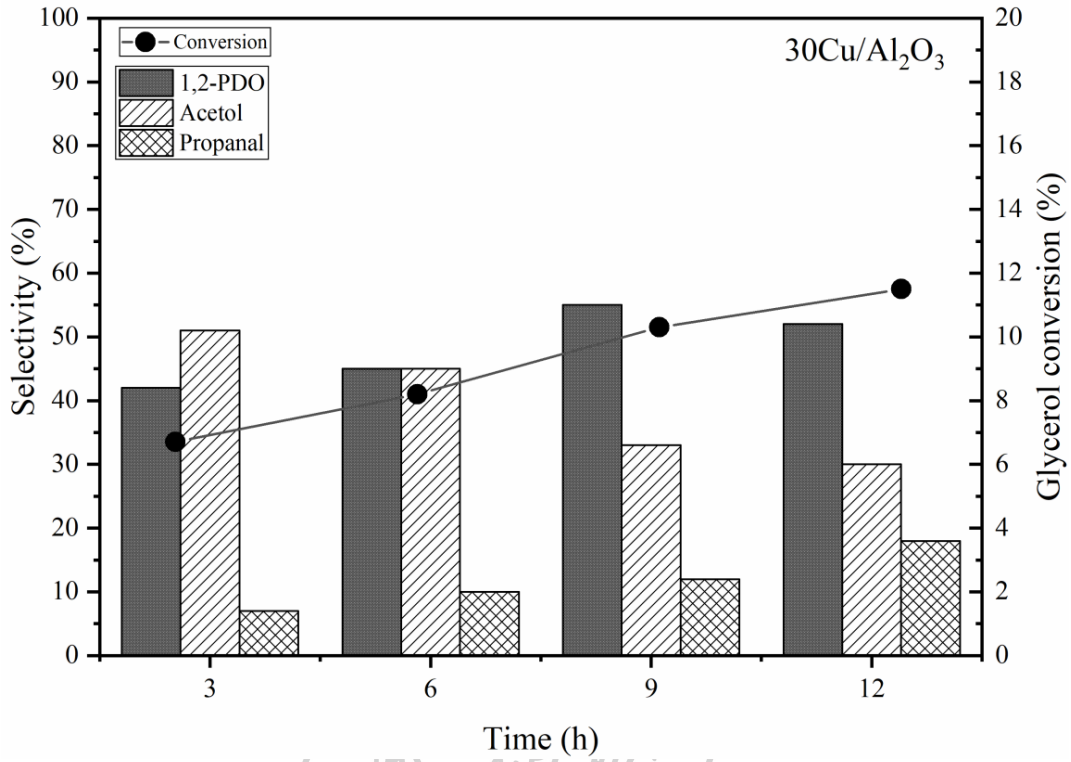

Figure 39 Effect of reaction time during the glycerol hydrogenolysis on $30Cu/Al_2O_3$ catalyst.

6.4 Conclusions

The $ZnAl_2O_4$ spinel phase was synthesis by FSP method which was confirmed by XRD results. The impregnated Cu on the FSP-made $Zn\text{-}Al_2O_3$ support, the CuO crystallite size of all catalyst were in range of 23-26 nm. Adding of Zn in FSP do not significantly affect crystallite size of CuO but can be improved the metal surface. A high selectivity of 1,2-PDO was obtained $30Cu/Zn\text{-}Al_2O_3$ catalysts, which the optimum Zn loading was 30 wt% of Zn ($30Cu/30Zn\text{-}Al_2O_3$). It was found that the formation of $ZnAl_2O_4$ on $30Cu/Zn\text{-}Al_2O_3$ decreased Lewis acid sites, leading to inhibit the decomposition of 1,2-propanediol forward to propanal.

.

CHAPTER VII

ROLE OF IRON ALUMINATE SPINEL SUPPORT ON COPPER-BASED CATALYST FOR HYDROGENOLYSIS OF GLYCEROL TO 1,2 PROPANEDIOL

7.1 The physical properties of Fe inserted on copper-based catalysts

7.1.1 The phase analysis by X-ray diffraction (XRD)

The X-ray diffraction peak of the FSP-made Fe-Al_2O_3 support were shown in Figure 40. The preparation of Fe-Al_2O_3 support by FSP gave hercynite phase or $FeAl_2O_4$ spinel phase as main phase. This phase was indicated by the notable peaks at 31.6º, 37.1º, 59.38º, and 65.2º. Hercynite structure ($FeAl_2O_4$) is a spinel structure that Fe^{2+} cations were located in tetrahedral sites and Al^{3+} cations are placed on in the octahedral sites in the nanocrystal (106). $FeAl_2O_4$ was synthesized via FSP method in previous work (48), Mainly $FeAl_2O_4$ phase was found at iron and alumina molar concentration of 0.2 and 0.2 mol. L^{-1}, respectively. The diffraction peak for Fe_2O_3 was observed in a high Fe addition (30 and 40 wt% Fe) at $2\theta = 33.03º$. With increasing Fe loading in FSP (10 to 40 wt% Fe), the linear diffraction peaks shift from γ-Al_2O_3 position to γ-$FeAl_2O_4$ position. It means the formation of a solid solution ($Fe_xAl_2O_{3+x}$) at intermediated concentrations (48).

Figure 41 shows the XRD pattern of 30Cu/Al_2O_3 and 30Cu/xFe-Al_2O_3 (x= 0, 10, 20, 30, and 40 wt% Fe) catalysts. The diffraction peak at 32.5º, 35.6º, 38.8º, 48.8º,53.5º, 58.3º, 61.6º,68.1º, 72.4º, and 75.2º were assigned to CuO phase. was low intensity with increasing Fe loading. It was indicated that the obtained CuO has low crystallinity. The CuO crystallite size can be calculate from diffraction peak of CuO (as calculation method showed in App. A). The CuO crystallite size of the inserted Fe catalyst was in range 19-21 nm as present in table 9, The CuO crystallite size for without Fe catalyst (30Cu/Al_2O_3) was larger than the inserted Fe catalyst because of the weak interaction between impregnated Cu and the Al_2O_3 support that easy to agglomeration of CuO and the large CuO particle was formed. On the other, addition of Cu on the Fe-

Al_2O_3 support exhibited strong interaction between impregnated Cu and the Fe-Al_2O_3 support, which was difficult to CuO agglomeration.

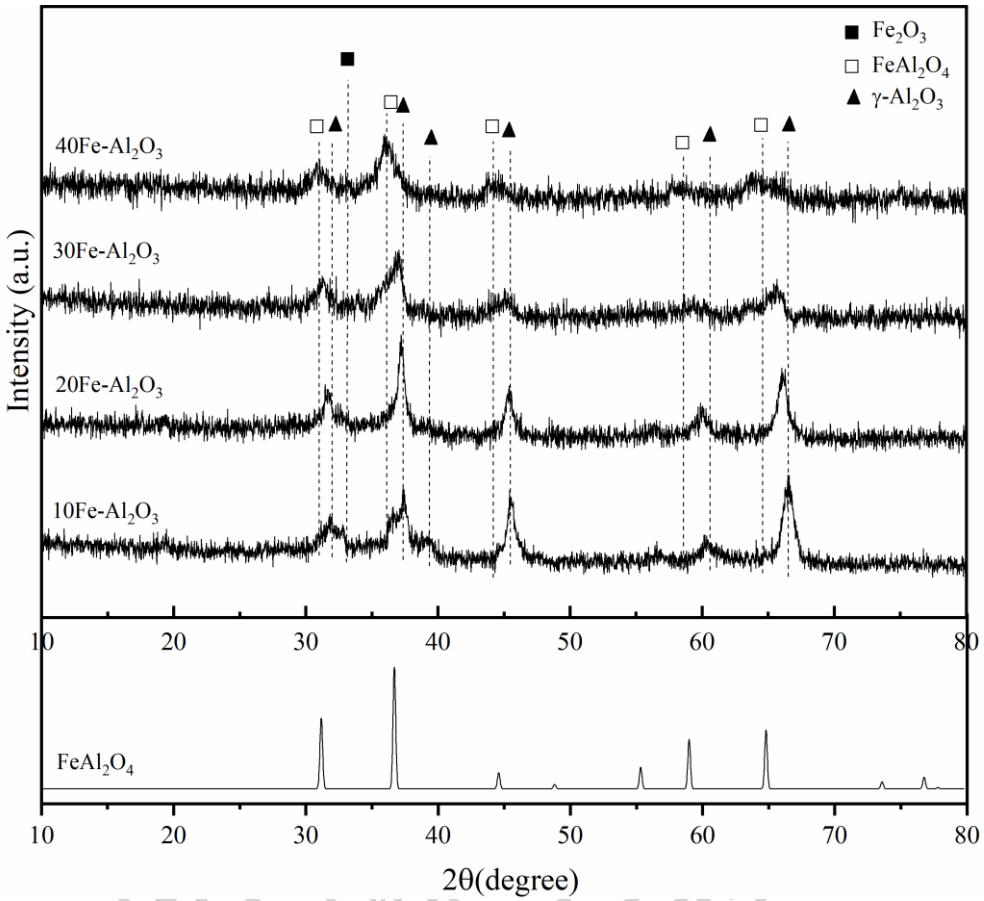

Figure 40 The XRD pattern of the FSP-inserted Fe (x Fe-Al_2O_3, x = 0, 10, 20, 30, and 40 wt% Fe).

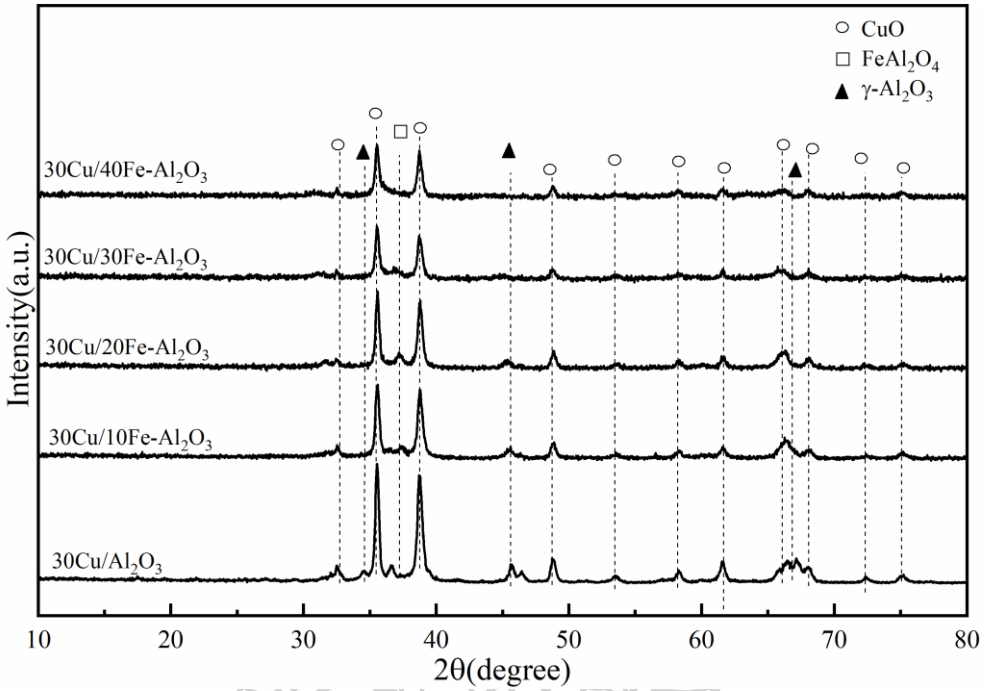

Figure 41 The XRD pattern of 30Cu/xFe-Al_2O_3 (x = 0, 10, 20, 30, and 40 wt% Fe) catalyst.

Table 9 The crystalline size of copper oxide on the FSP-made Fe-Al_2O_3 from XRD results.

Catalysts	**CuO crystalline size (nm)**
30Cu/Al_2O_3	26.2
30Cu/10Fe-Al_2O_3	21.9
30Cu/20Fe-Al_2O_3	21.1
30Cu/30Fe-Al_2O_3	19.0
30Cu/40Fe-Al_2O_3	19.3

7.1.2 The BET surface area and pore characteristics of catalyst

The BET surface area, and total pore volume were shown in Table 10. The BET surface area was increased slightly in the xFe-Al_2O_3 (x=10, 20, 30, and 40 wt%) support (A_s = 43-48 m^2/g) as compared with Al_2O_3 support (A_s = 37 m^2/g). In addition, the increased amount of iron with alumina during in FSP were not affect to the BET surface area, this attributed that the Fe incorporated during FSP did not disturb the formation of Al_2O_3 particles resulting in the same characteristics of support. Figure 42 (a**)** and (b) show the N_2 adsorption/desorption isotherm of Fe-Al_2O_3 supports and 30Cu/xFe-Al_2O_3 catalyst, respectively. All of them were H3-type in relation to IUPAC classification isotherm which presented characteristic of aggregates of plate-like particles or slit-shaped pores.

มหาวิทยาลัยศิลปากร

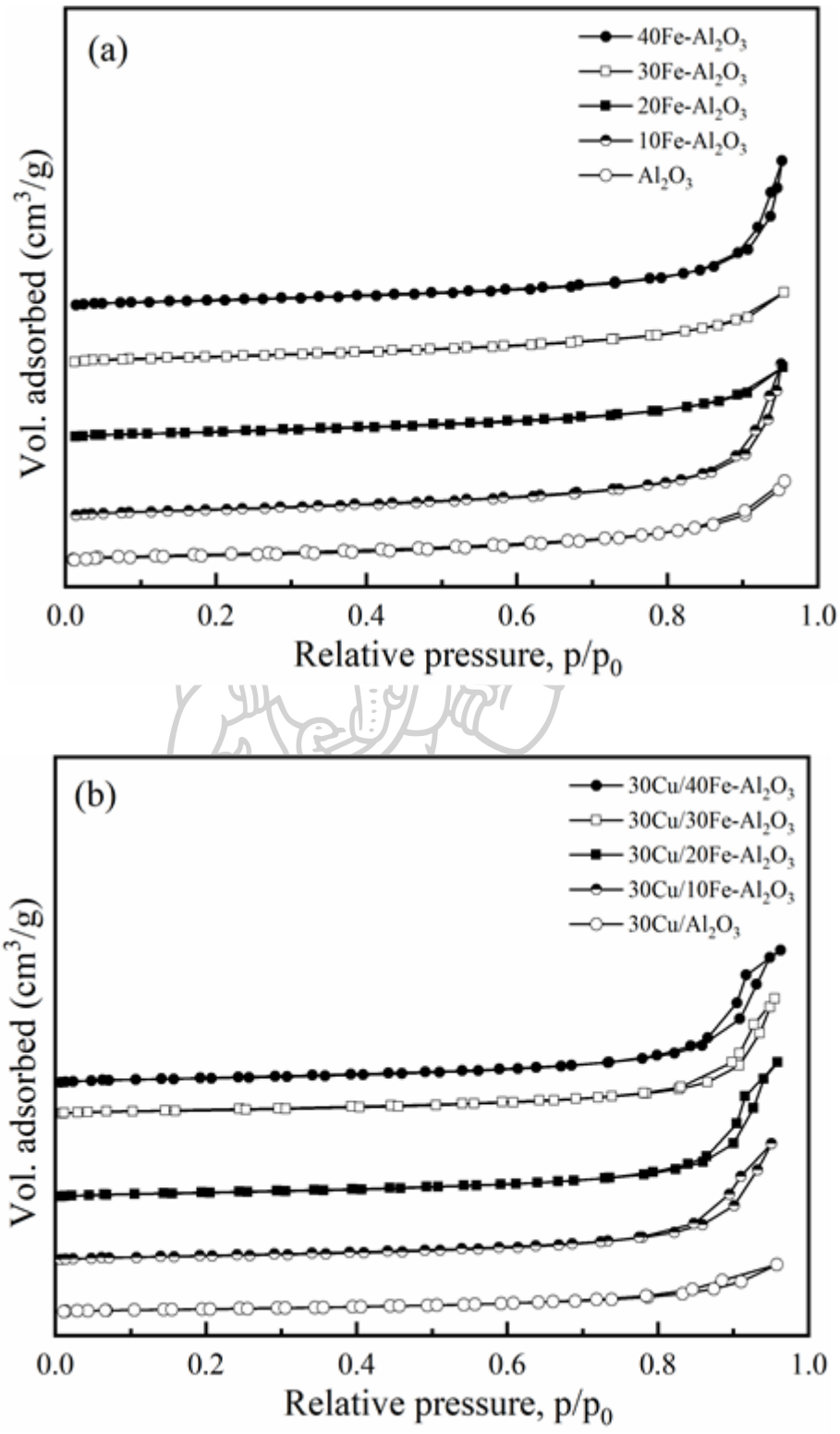

Figure 42 The N_2 adsorption/desorption isotherms: (a) the FSP-made xFe-Al_2O_3, (x = 0, 10, 20, 30, and 40 wt% Fe), (b) 30Cu/xFe-Al_2O_3 (x = 0, 10, 20, 30, and 40 wt% Fe) catalyst.

Table 10 The BET surface area and total pore volume of catalyst.

Samples	BET surface area (m^2/g)	Total pore volume(cm^3/g)
Al_2O_3	37	0.11
10Fe-Al_2O_3	48	0.22
20Fe-Al_2O_3	43	0.10
30Fe-Al_2O_3	44	0.11
40Fe-Al_2O_3	43	0.21
30Cu/Al_2O_3	19	0.07
30Cu/10Fe-Al_2O_3	30	0.16
30Cu/20Fe-Al_2O_3	29	0.19
30Cu/30Fe-Al_2O_3	27	0.16
30Cu/40Fe-Al_2O_3	30	0.18

7.2 The chemical properties of Fe inserted on copper-based catalysts

7.2.1 Reduction behavior of catalyst by temperature programed reduction (TPR)

The TPR profile of the Fe_2O_3 bulk were shown in Figure 43. The reduction peaks of Fe_2O_3 bulk displayed two main reduction peaks. The first reduction peak in a range 220-410 ºC assigned to the reduction of Fe_2O_3 to Fe_3O_4 species. The second reduction peak at a temperature above 410 ºC that the reduction of Fe_3O_4 and FeO to Fe metallic species. The Fe_2O_3 reduction with hydrogen to Fe occurred two-step process were reported, as two-step mechanisms were the reduction of Fe_2O_3 to Fe_3O_4 and then Fe_3O_4 to Fe metal (equation 1-1 and 1-2) (109-111). Moreover, the three-step reduction of Fe_2O_3 was possible. The Fe_2O_3 was reduced to Fe_3O_4 , Fe_3O_4 was subsequently reduced to FeO and then FeO to Fe metal (equation 2-1 ,2-2 and 2-3) (112). The following equations were designated in the below equation. The literature noted that H_2 and H_2O concentration affect the reduction behavior. Jerzy Zieliński and coworkers

(109) found that the Fe_2O_3 reduction was three-step at $xH_2O/_xH_2$ ratio upper 0.35, while the two-step reduction below that value.

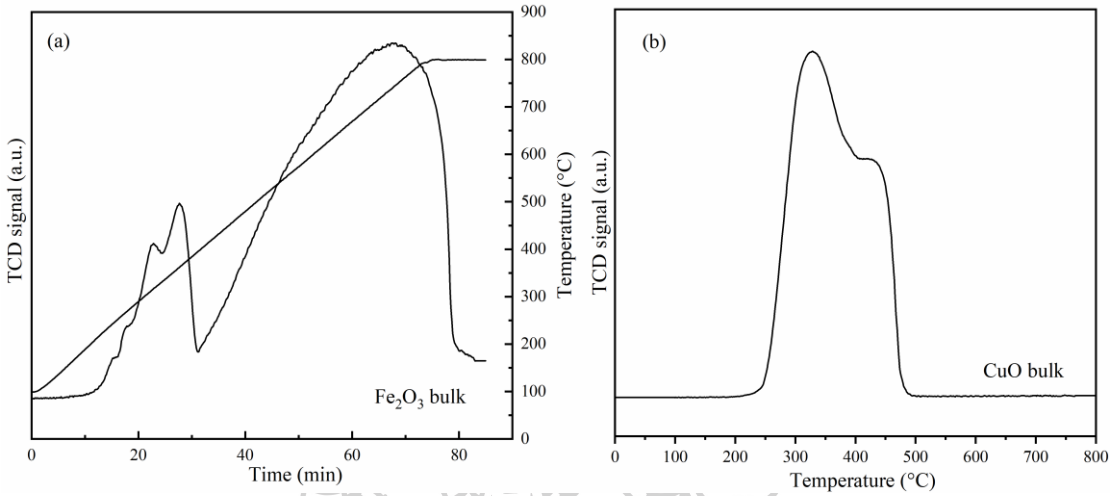

Figure 43 H_2-TPR patterns of the iron oxide and copper oxide bulk

The two-step mechanism

$$1^{st}\text{ step:} \quad 3Fe_2O_3+H_2 \rightarrow 2Fe_3O_4+H_2O \quad \text{—1-1}$$

$$2^{nd}\text{ step:} \quad Fe_3O_4+4H_2 \rightarrow 3Fe+4H_2O \quad \text{—1-2}$$

The three-step mechanism

$$1^{st}\text{ step:} \quad 3Fe_2O_3+H_2 \rightarrow 2Fe_3O_4+H_2O \quad \text{—2-1}$$

$$2^{nd}\text{ step:} \quad 2Fe_3O_4+2H_2 \rightarrow 6FeO+2H_2O \quad \text{—2-2}$$

$$3^{rd}\text{ step:} \quad 6FeO+6H_2 \rightarrow 6Fe^0+6H_2O \quad \text{—2-3}$$

The H_2-TPR patterns of the xFe-Al_2O_3 (x= 0, 10, 20, 30, and 40 wt% Fe) were shown in Figure 44. The TPR result of 10Fe-Al_2O_3 support showed the main reduction peak at 400 C^o and wide shoulder peak at 480 to 700 C^o, which assigned to the reduction of Fe_2O_3 to Fe_3O_4 and Fe_3O_4 to FeO + Fe, respectively. The reduction behavior of

10Fe-Al_2O_3 and 20Fe-Al_2O_3 were rather silimar. The high reduction temperature peaks in a range of 600 to 800 Cº were cearly seen in the TPR profiles of 30Fe-Al_2O_3 and 40Fe-Al_2O_3. This was suggested that the large iron oxides species were reduced.

Figure 45 present the H_2-TPR patterns of the 30Cu/*x*Fe-Al_2O_3 (x= 0, 10, 20, 30, and 40 wt % Fe) catalysts. The TPR profile of 30Cu/Al_2O_3 presented reduction temperature in a range 220 to 370 Cº assigned to the two-step reduction of copper oxide ($CuO \rightarrow Cu_2O \rightarrow Cu^0$). With addition Fe on Cu/Al_2O_3 catalyst, the positions of the reduction peak were shifted to lower temperature with increasing Fe loading. It was speculated that the small CuO crystallite well dispersed on Fe-Al_2O_3 support, the small metal oxide particles size can result in faster reduction because greater surface area per volume ratio (113).

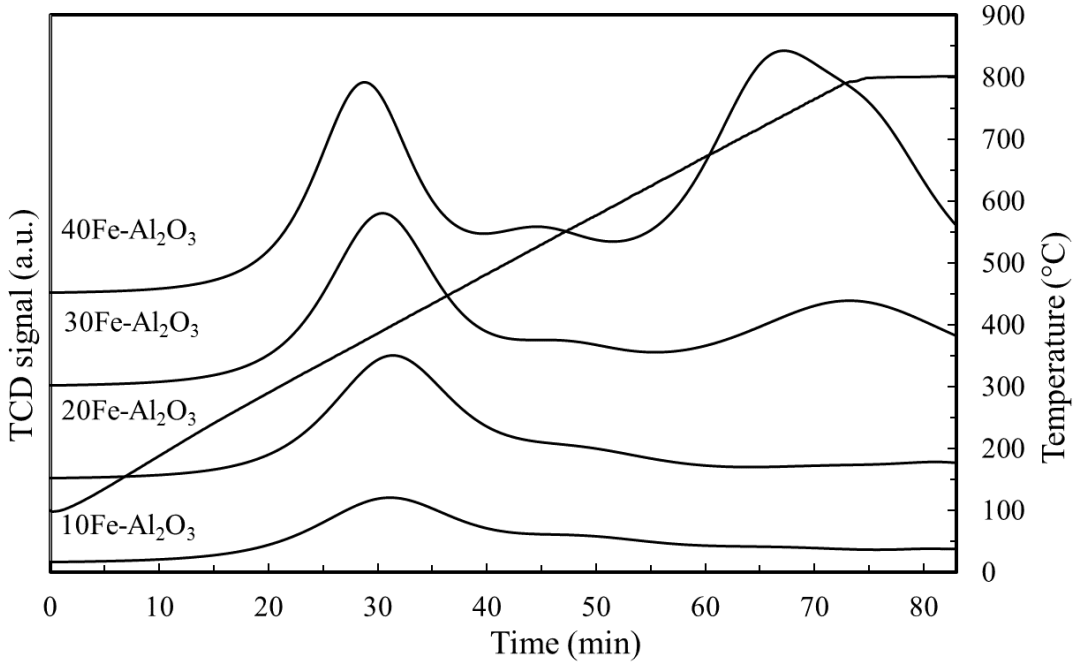

Figure 44 H_2-TPR patterns of the FSP-made xFe-Al_2O_3 (x= 0, 10, 20, 30, and 40 wt% Fe).

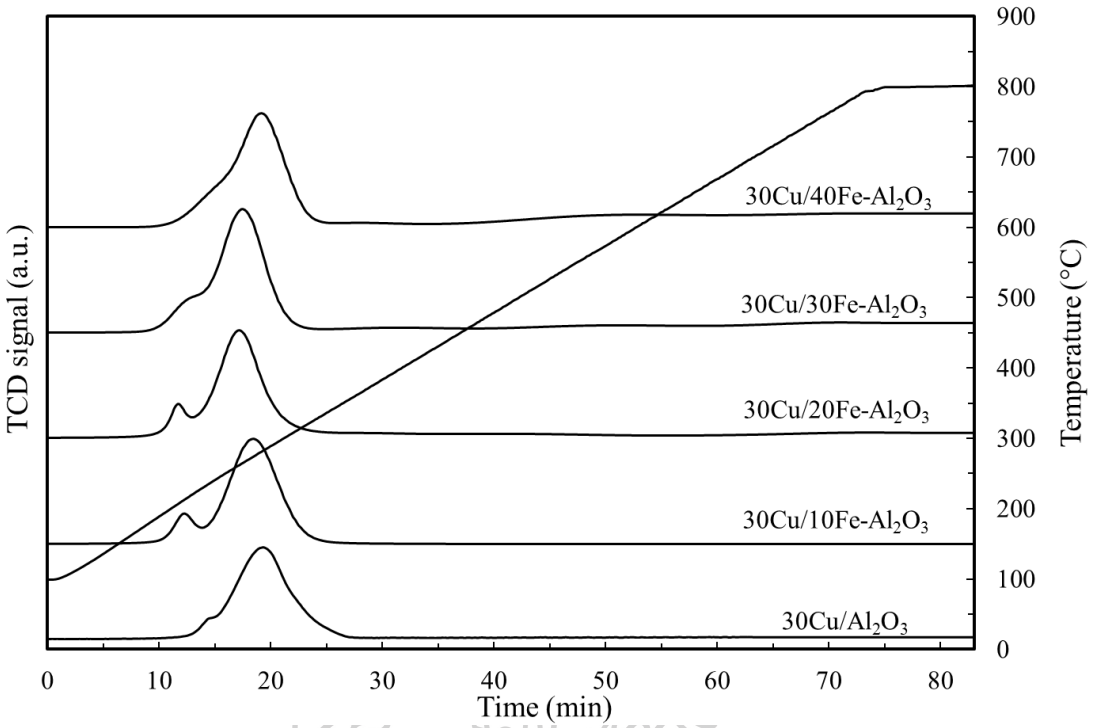

Figure 45 H_2-TPR patterns of the 30Cu/xFe-Al_2O_3 (x= 0, 10, 20, 30, and 40 wt% Fe) catalysts.

7.2.2 The copper metallic sites by N_2O decomposition

The results of N_2O decomposition of 30Cu/xFe-Al_2O_3 (x = 0, 10, 20, 30, and 40 wt% Fe) were shown in Figure 46. The 30Cu/Al_2O_3 displayed the lowest copper active site due to the dispersed large copper particle on catalyst surface, as the CuO crystallite size were 26 nm following to the XRD result. The presence of Fe on catalyst increased the copper metal active site because of the existence of small copper particle size and good dispersed on support. Moreover, the copper active site increased with increasing Fe loading**.** The addition of 30 and 40 wt % Fe gave the equivalent number of active sites**.** This result was possible to influence the same characteristic of catalyst. Which the reduction behavior of the both catalysts were resembling (as shown in Figure 45) and the crystallite size of CuO was about 19 nm (as listed in Table 9).

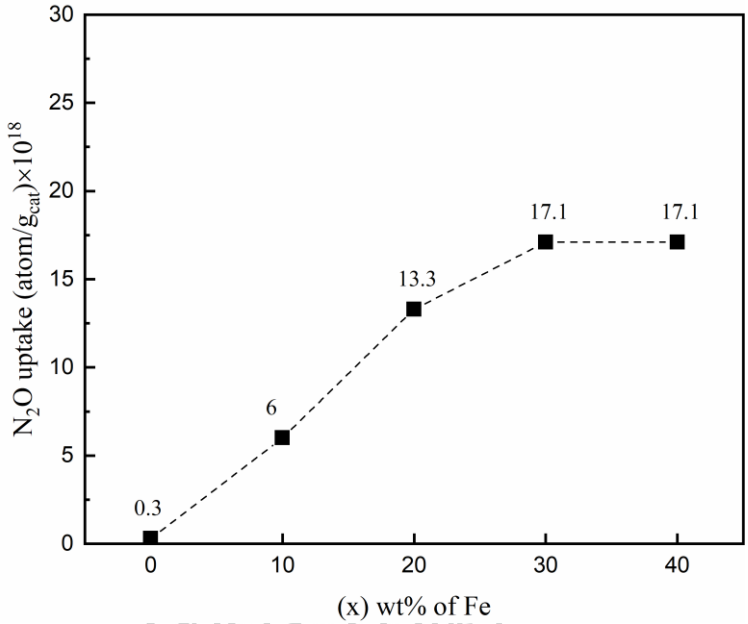

Figure 46 N_2O decomposition results of 30Cu/xFe-Al_2O_3 (x = 0, 10, 20, 30, and 40 wt% Fe).

7.3 Catalytic performance of Fe inserted on copper-based catalysts

Catalytic performance of glycerol hydrogenolysis was carried out using reduced 30Cu/xFe-Al_2O_3 with different Fe loading. The glycerol conversion and product selectivity were shown in Figure 47. The 30Cu/Al_2O_3 displayed 7% of glycerol conversion and 42 % of 1,2-PDO selectivity. When small amount of Fe was loaded (10 wt %), the glycerol conversion and product selectivity were scarcely unchanged compared to 30Cu/Al_2O_3. With addition of 20 to 40 wt% Fe on Cu/Al_2O_3 catalysts, the activity and product selectivity were close and high selectivity of 1,2-PDO, which the 30Cu/30Fe-Al_2O_3 exhibited the highest selectivity of 1,2PDO (65%) due to a high active surface. This indicated that the presence Fe can be promote the utilization of active H_2 for hydrogenation of acetol to 1,2-PDO step (114). It speculated that the catalyst presented two active sites species, there are Cu metal and Fe metal, which the both metals was active for H_2 adsorption. According to the result, the appearance of $FeAl_2O_4$ phase on catalyst relate to the enhanced selectivity of 1,2-PDO, although the

reason is still unclear. While Francesco Mauriello et al. (115) reported that pure Fe_3O_4 does not give glycerol conversion for glycerol hydrogenolysis reaction.

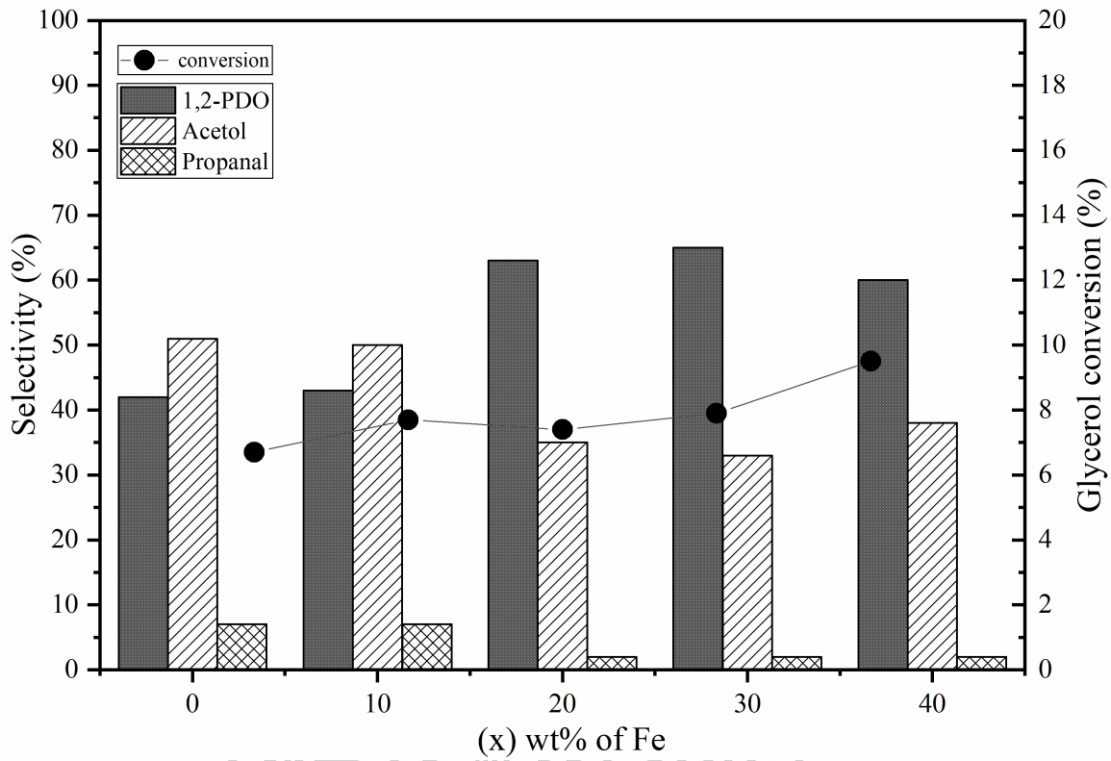

Figure 47 The activity and selectivity of the 30Cu/xFe-Al_2O_3, (x= 0, 10, 20, 30, and 40 wt% Fe) catalyst.

7. 4 Conclusions

The catalytic performance of inserting Fe on 30Cu/Al_2O_3 by FSP method with different Fe loading was investigated. The FSP-made Fe-Al_2O_3 presented hercynite phase ($FeAl_2O_4$) and iron oxide (Fe_2O_3). The incorporation of Fe and Al_2O_3 precursor during FSP can be inhibited the growth of Al_2O_3 particle leading to a higher BET surface area than pure Al_2O_3 precursor. The CuO crystallite size of 30Cu/Fe-Al_2O_3 catalysts were in a range 19-21, that lower than 30Cu/Al_2O_3 catalyst. However, the increasing amount of Fe loading did not affect to CuO crystallite size but decreased CuO crystallinity. The Fe content of 20 to 40 wt% on catalysts enhanced 1,2-PDO selectivity, even though the glycerol conversion hardly changed. The coexistence of Cu, Fe and $FeAl_2O_4$ phases can enhance selectivity of 1,2-PDO.

CHAPTER VIII

ROLE OF COBALT ALUMINATE SPINEL SUPPORT ON COPPER-BASED CATALYST FOR HYDROGENOLYSIS OF GLYCEROL TO 1,2 PROPANEDIOL

8.1 The physical properties of Co inserted on copper-based catalysts

8.1.1 The phase analysis by X-ray diffraction (XRD)

The X-ray diffraction patterns of *x*Co-Al_2O_3 supports (x= 10, 20, 30 and 40 wt.% Co) were shown in Figure 48. The XRD peak approved the appearance of γ-Al_2O_3 phase at 2θ = 31.98º, 37.67º, 45.77º and 66.52º. The diffraction pattern display characteristic of Co_3O_4 and $CoAl_2O_4$ are overlap at 31.48º, 37.11º, 45.01º, 59.62º, and 65.43º, the formation cobalt aluminate ($CoAl_2O_4$) can be formed at high temperature of preparation which FSP catalysts were made at high temperature up to 3000 K (116) during FSP process. The $CoAl_2O_4$ diffraction peak clearly seen at 2θ=55.86º for all *x*Co-Al_2O_3 (*x* = 10, 20, 30 and 40 wt.% Co). The sharp peak of Co_3O_4 and $CoAl_2O_4$ were clearly found with increasing Co loading. This show a formation of large Co_3O_4 particles. The XRD patterns of 30Cu/xCo-Al_2O_3 catalysts were presented in Figure 49**.** The diffraction peak of CuO phase were observed at 2θ =32.5º, 35.6º, 38.8º, 48.8º, 53.5º, 58.3º, 61.6º, 68.1º, 72.4º, and 75.2º. The intensity of CuO decreased with increasing Co loading, indicating that the high Co loading catalyst have a lower crystallinity. The crystallite of CuO of the inserted Co catalyst was in range 21-23 nm which lower than CuO crystallite of 30Cu/Al_2O_3 catalyst as listed in Table 1

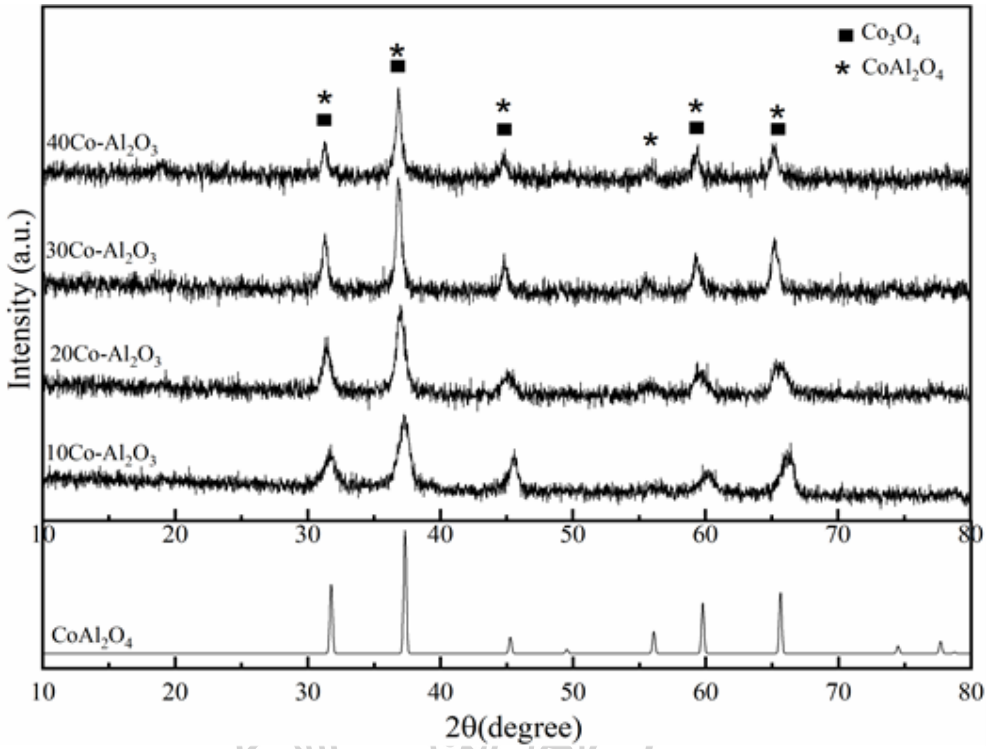

Figure 48 The XRD pattern of the FSP-inserted Co (xCo-Al_2O_3, x = 0, 10, 20, 30, and 40 wt% Co).

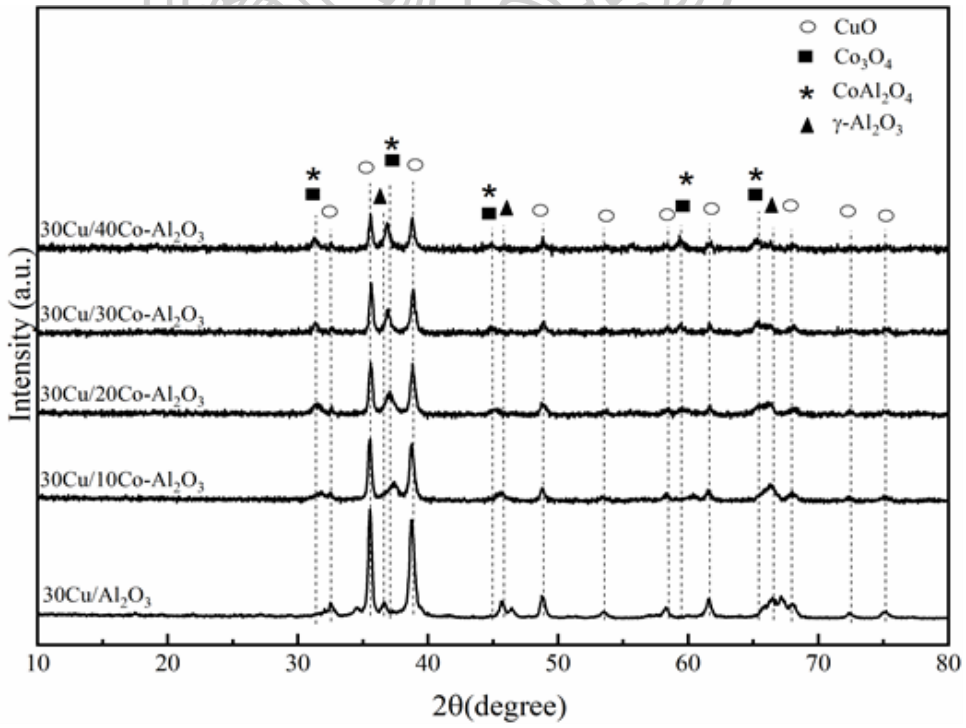

Figure 49 The XRD pattern of 30Cu/xCo-Al_2O_3 (x = 0, 10, 20, 30, and 40 wt% Co) catalyst.

Table 11 The crystalline size of copper oxide on the FSP-made Co-Al_2O_3 from XRD results.

Catalysts	CuO crystalline size (nm)
30Cu/Al_2O_3	26.2
30Cu/10Co-Al_2O_3	23.4
30Cu/20Co-Al_2O_3	22.8
30Cu/30Co-Al_2O_3	22.2
30Cu/40Co-Al_2O_3	21.1

8.1.2 The BET surface area and pore characteristics of catalyst

The BET surface area, and total pore volume of catalysts were characterize using N_2 adsorption/desorption measurement (BEL SORP MINI). The textural properties were shown in Table 12. The BET surface area and total pore volume of Al_2O_3 were 37 m^2/g and 0.11 cm^3/g. the addition 10 wt.% of Co with Al_2O_3 in FSP process (10Co-Al_2O_3), BET surface area increase to 59 m^2/g. It was suggested that growth of Al_2O_3 particles was inhibited by Co during in FSP process, leading to an increase in surface area and smaller particle size. When addition larger amount of Co (20, 30 and 40 wt.% of Co), the BET surface area decreases to 41, 36 and 42 m^2/g. However, it was greater than pure Al_2O_3. For 30Cu/Co-Al_2O_3. The 30Cu/10Co-Al_2O_3 showed the highest surface area as 45 m^2/g. The N_2 adsorption/desorption isotherm of samples were shown in Figure 50. All of them were H3-type in relation to IUPAC classification isotherm which presented characteristic of aggregates of plate-like particles or slit-shaped pores.

Table **12** The BET surface area and total pore volume of catalyst.

Samples	BET surface area (m^2/g)	Total pore volume(cm^3/g)
Al_2O_3	37	0.11
10Co-Al_2O_3	59	0.19
20Co-Al_2O_3	41	0.10
30Co-Al_2O_3	36	0.10
40Co-Al_2O_3	42	0.07
30Cu/Al_2O_3	19	0.07
30Cu/10Co-Al_2O_3	45	0.13
30Cu/20Co-Al_2O_3	28	0.09
30Cu/30Co-Al_2O_3	25	0.09
30Cu/40Co-Al_2O_3	30	0.07

มหาวิทยาลัยศิลปากร

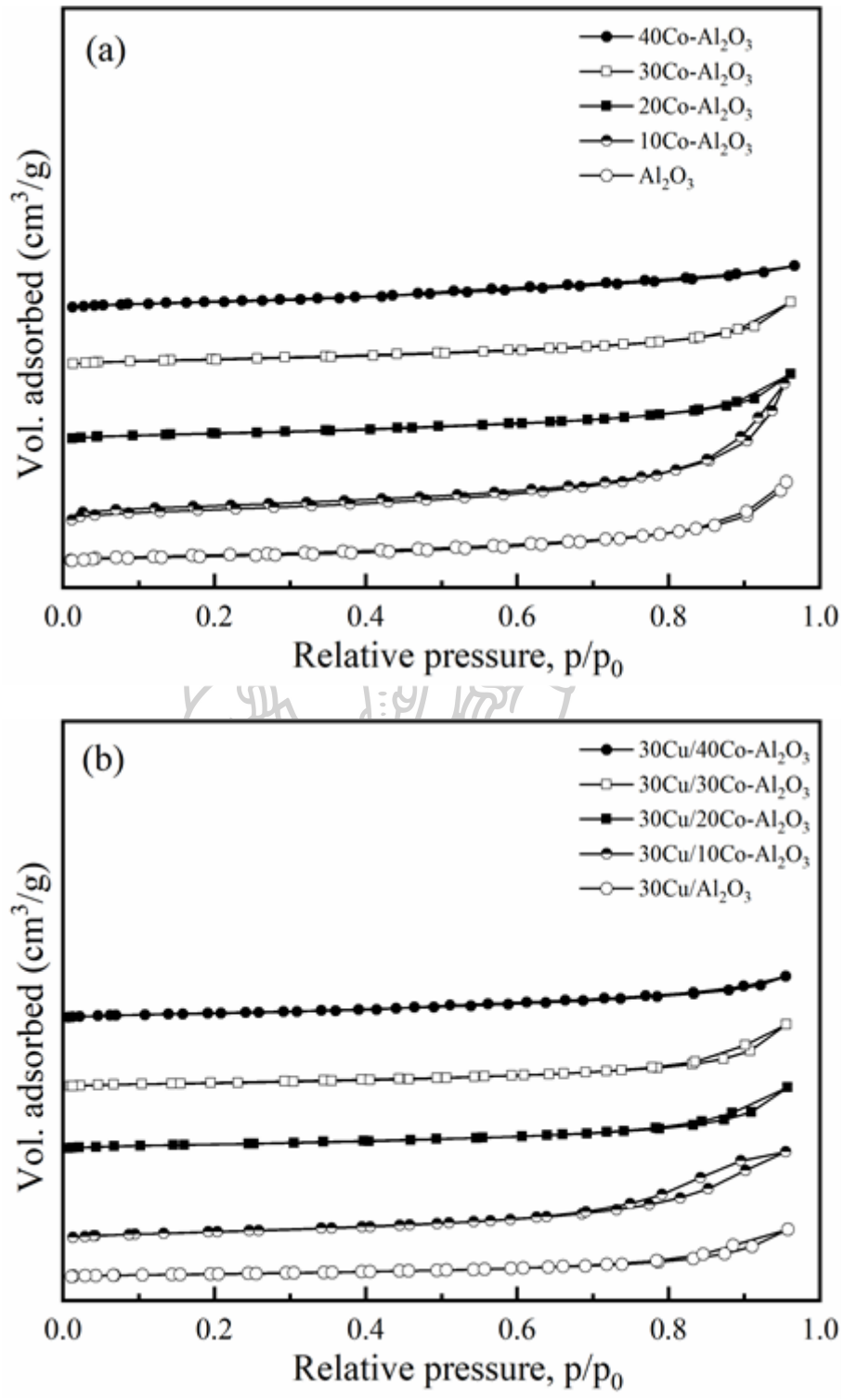

Figure 50 The N_2 adsorption/desorption isotherms: (a) the FSP-made x$Co\text{-}Al_2O_3$, (x = 0, 10, 20, 30, and 40 wt% Co), (b) 30Cu/x$Co\text{-}Al_2O_3$ (x = 0, 10, 20, 30, and 40 wt% Co) catalyst.

8.2 The chemical properties of Co inserted on copper-based catalysts

8.2.1 Reduction behavior of catalyst by temperature programed reduction (TPR)

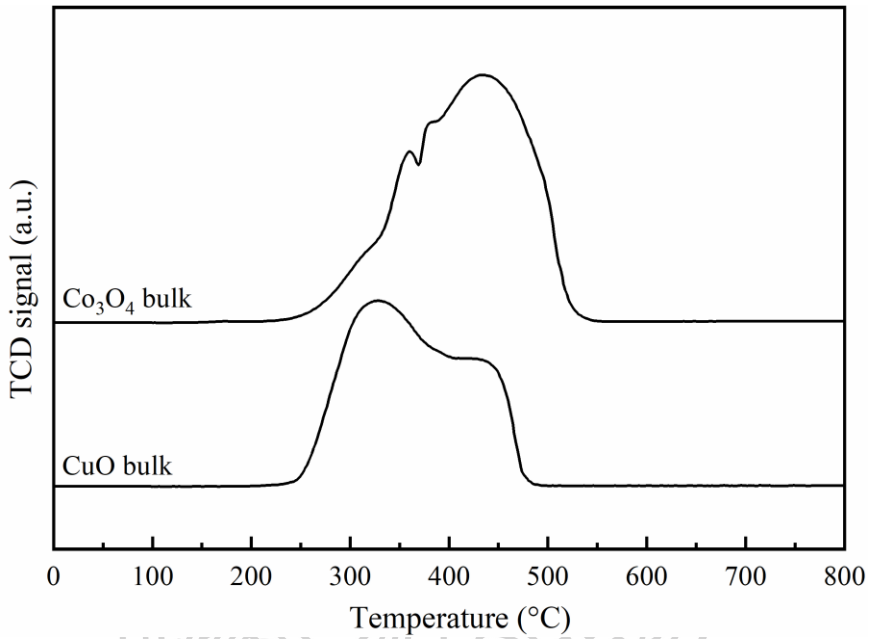

Figure 51 H_2-TPR patterns of the copper oxide and cobalt oxide bulk.

The H_2-TPR patterns for CuO and Co_3O_4 bulk were shown in Figure 51. The Co_3O_4 bulk was reduced at temperature range 250 to 550 ºC, assigned to the two-reduction steps of cobalt oxide. These were the reduction of Co_3O_4 to CoO and then CoO to Co metal (as showed in equation 8-1 and 8-2). For the reduction of CuO bulk was mentioned in previously chapter.

$$Co_3O_4 + H_2 \rightarrow 3CoO + H_2O \qquad \text{— 8-1}$$

$$3CoO + 3H_2 \rightarrow 3Co + 3H_2O \qquad \text{— 8-2}$$

Figure 52 presents the H_2-TPR profiles of the of the xCo-Al_2O_3 (x= 0, 10, 20, 30, and 40 wt% Co). The FSP-made Co-Al_2O_3 support presented the two main peaks. The first peak attributed to the reduction processes of Co_3O_4 to CoO and CoO to Co

metal (α region). The seconded peak in high temperature range assigned to the embedded small cobalt size and strong interaction of cobalt with alumina matrix like Co-Al_2O_3, $CoAl_2O_4$ species (β region) (117, 118), which the reduction of bulk $CoAl_2O_4$ can completely reduce at temperature above 1273 K (119). The reduction of Co/Al_2O_3 catalyst was explained by Jacob et.al (120) there are three possible cases Case1, the two-step reduction of Co_3O_4 to CoO and CoO to metallic Co occurred in temperature range 200 to 400 ºC (Co_3O_4→CoO), and 400 to 800 ºC (CoO→Co), respectively. In case 2, the one-step reduction of Co_3O_4 to Co metal occurred in the range 277 to 377 ºC. and then the dispersed Co^{3+} and Co^{2+} species on surface were reduced in the range 450 to 600 ºC and 600 to 650 ºC. Case 3 the one-step reduction of Co_3O_4 to Co metal was identical with case 2, and the mixed oxide (CoO-Al_2O_3) was reduced. It can be observed that the two main peak (α and β region) was shifted to lower temperature with increasing Co loading. This was suggested that the interaction of cobalt oxide species with alumina became weaken. It was possible that a higher Co loading in FSP process can be formed to more Co_3O_4 phase than Co-Al_2O_3 mixed oxide phase in short resident time process during FSP process.

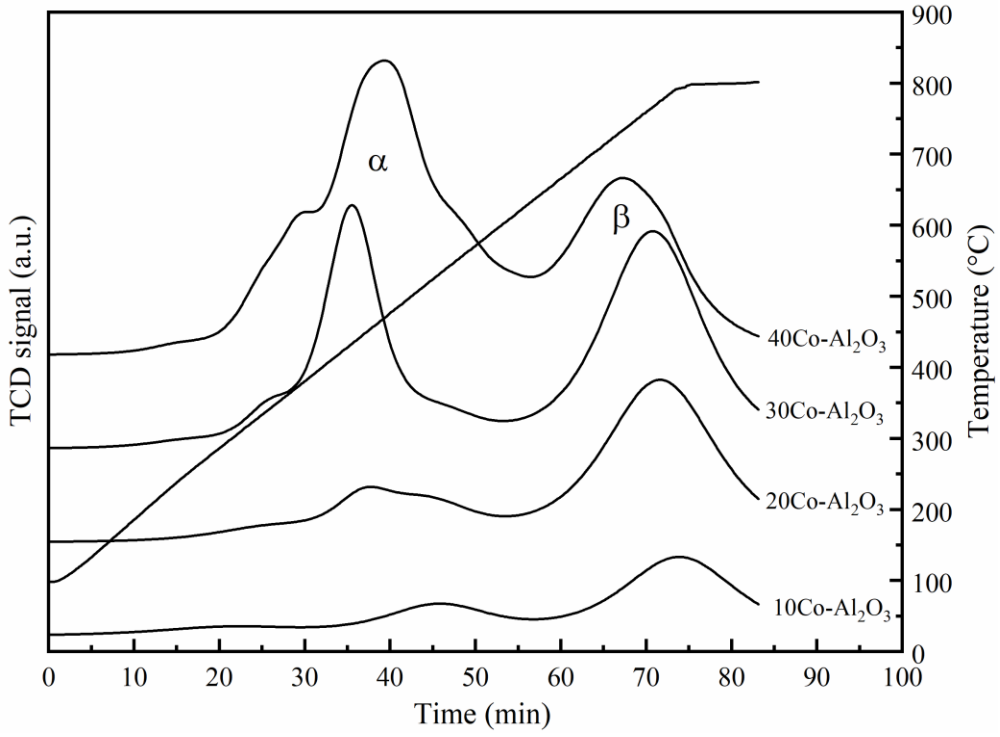

Figure 52 H_2-TPR patterns of the xCo-Al_2O_3 (x= 0, 10, 20, 30, and 40 wt% Co).

The addition of impregnated copper (30wt % Cu) on FSP-made Co-Al_2O_3 was displayed in Figure 53. The reduction peaks can be explained two temperature range, The first temperature range at 100 to 350 Cº assignted to reduction of CuO particle ($CuO \rightarrow Cu_2O \rightarrow Cu$) and interaction between copper oxide and cobalt oxide surface. X. Mo et al. (121) reported that the TPR profile of CoCu presented the main reduction peak at temperature 100 to 250 ºC. The position of reduction peak shifted to lower temperature with increasing the amount of Co. This indicated a weak interaction of copper oxide with alumina support. Owing to the Cu was impregnated on the Co-Al_2O_3 surface, the impregnated Cu could be attracted the Co particles than Al_2O_3 supported when increased Co loading. As the interaction between Cu and Co easily reduced than interaction between Cu and Al_2O_3. Then, It can be improved reducibility of catalyst. The cobalt oxide can be partially reduced from 30Cu/Cu-Al_2O_3 ctalysts. The second temperature range at 350 to 800 ºC assignted to the reduction of cobalt oxide to cobalt metal ($Co_3O_4 \rightarrow CoO \rightarrow Co$) and strong interaction between cobalt and alumina suppot as presents in TPR results of xCu-Al_2O_3.

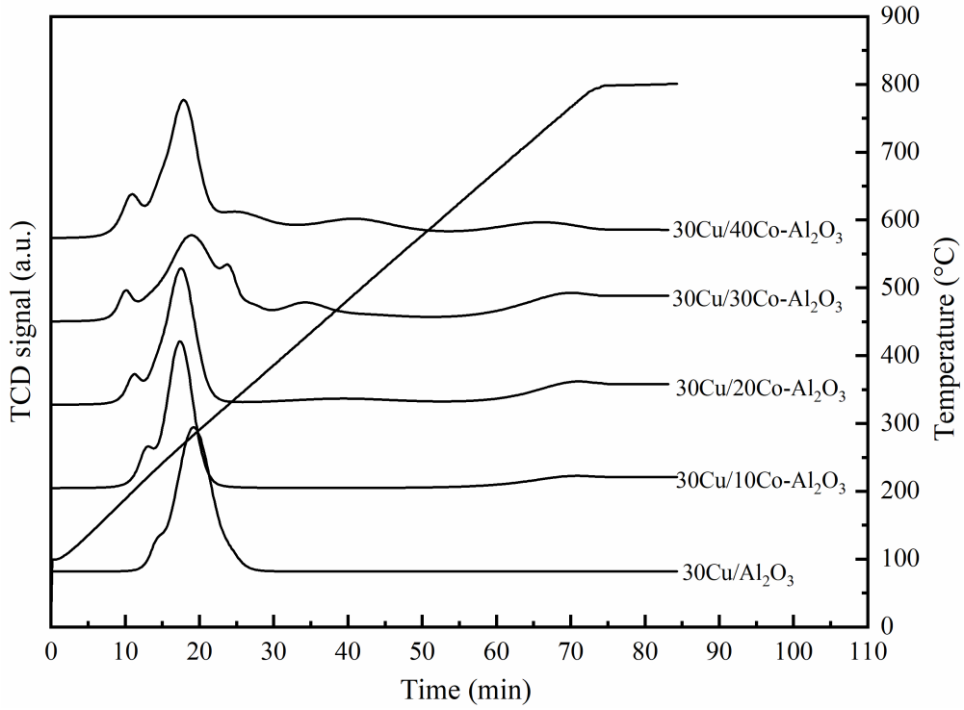

Figure 53 H_2-TPR patterns of the 30Cu/xCo-Al_2O_3 (x= 0, 10, 20, 30, and 40 wt% Co) catalysts.

8.2.2 X-ray photoelectron spectroscopy (XPS)

The chemical states and elements on region of the FSP-made Co-Al_2O_3 with different Co loading were characterized by XPS and XPS spectra were shown in Figure 54. The all sample show Co2p core level spectrum are Co $2p_{3/2}$ and $Co2p_{1/2}$. Normally, the Co_3O_4 presented two oxidation stages that are one Co^{2+} cation in tetrahedral and Co^{3+} cation in octahedral site ($(Co^{3+})_2(Co^{2+})O_4$). The binding energies of Co^{2+} and Co^{3+} have been reported, the Co^{2+} cation located at approximately 780.3 eV and Co^{3+} located at approximately 779.5 eV. For $CoAl_2O_4$ spinel structure, the Co^{2+} cations are tetrahedral site and Al^{3+} cations are octahedral site in lattice. The Co $2p_{3/2}$ peak of $CoAl_2O_4$ is higher binding energy than Co_3O_4, with the binding energy rang of 782 eV or higher (122, 123). The 10Co-Al_2O_3 sample observed the Co 2p3/2 level at 783.9 eV, assigned to Co^{2+} cation in tetrahedral site of $CoAl_2O_4$ structure. The Al 2p spectra centered at 76.9 eV, assigned to octahedral Al^{3+} cation (124). With increasing Co loading during FSP step, The $Co2p_{3/2}$ peak position was significantly shifted toward lower binding energy from 783.8 to 782.5 eV (as listed in Table 13). These results indicated that a lower Co loading in FSP step displayed intensive $CuAl_2O_4$ spinel phase.

Table 13 XPS data for Co 2p, O 1s, and Al 2p of the xCo-Al_2O_3 (x=10, 20, 30, and 40 wt% Co).

sample	**Co $2p_{3/2}$ (eV)**	**Co $2p_{1/2}$ (eV)**	**O1s(eV)**	**Al 2p (eV)**
10Co-Al_2O_3	783.9	800.2	533.5	76.9
20Co- Al_2O_3	783.7	799.5	533.2	76.6
30Co- Al_2O_3	782.1	797.3	532.4	75.4
40Co- Al_2O_3	782.5	798.1	532.4	76.1

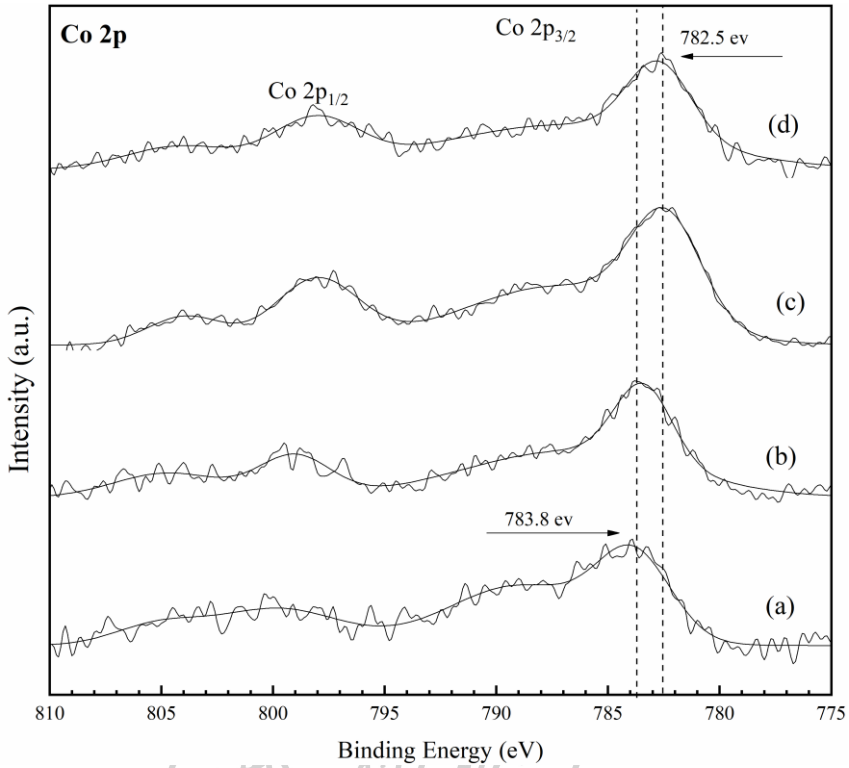

Figure 54 XPS spectra of Co 2p of the xCo-Al_2O_3 (x=10, 20, 30, and 40 wt%).

8.2.2 The copper metallic sites by N_2O decomposition

The N_2O decomposition results of 30Cu/xCo-Al_2O_3 (x = 0, 10, 20, 30, and 40 wt% Co) were presented in Figure 55. The appearance of Co on Cu/Al_2O_3 catalyst improved the number of copper active sites, which addition of 40 wt% Co on 30Cu/Al_2O_3 show the highest number of copper active sites. It can be attributed to the improved reducibility of catalyst leading to improve the number of active sites.

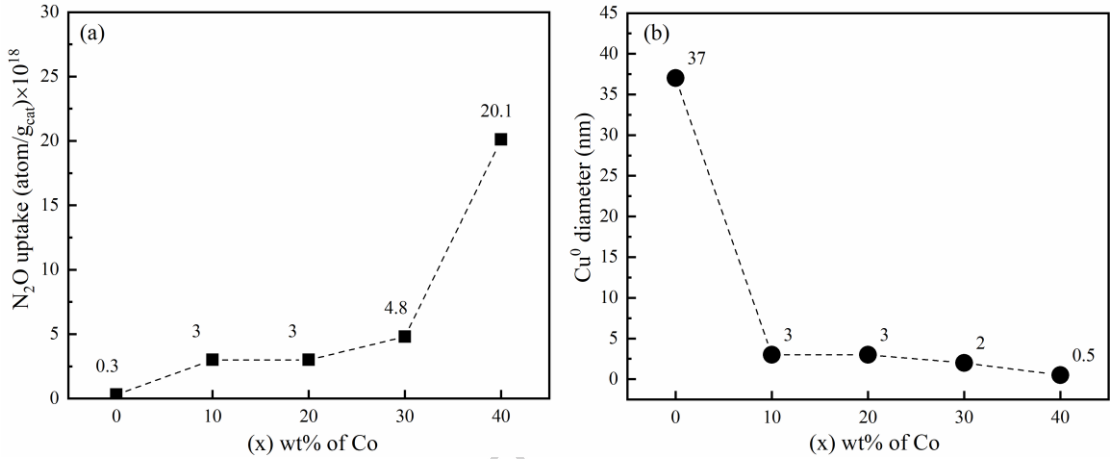

Figure 55 (a) N_2O chemisorption results of 30Cu/xCo-Al_2O_3 (x = 0, 10, 20, 30, and 40 wt% Co), (b) diameter of copper metallic size of 30Cu/xCo-Al_2O_3 (x = 0, 10, 20, 30, and 40 wt% Co) catalyst

8.3 Catalytic performance of Co inserted on copper-based catalysts

The activity and selectivity of the 30Cu/xCo-Al_2O_3, (x= 10, 20, 30, and 40 wt% Co) were represented in Figure 56. The 30Cu/Al_2O_3 catalyst exhibited 47 % of glycerol conversion and 42% of 1,2-PDO. When 10 to 30 wt% Co were added to 30Cu/Al_2O_3 during FSP process. The glycerol conversion was hardly unchanged but selectivity of 1,2-PDO decreased and acetol increased compared to 30Cu/Al_2O_3. Hydrogenolysis of glycerol to 1,2-Propandiol (1,2-PDO) reaction occurred through 2 steps, first, the glycerol dehydration on acid site to acetol and then its hydrogenation to 1,2-PDO on metal site. Form XPS and H_2-TPR results, the incorporated 10 to 30 wt% Co with Al_2O_3 presented high $CoAl_2O_4$ surface. It was possible that the loaded Cu on $CoAl_2O_4$ catalyst promoted the glycerol dehydration. When 40 wt% of Co was added on 30Cu/Al_2O_3, the glycerol conversion increased to 11 % and selectivity of 1,2-PDO up to 70 %. It speculated that the active site of 30Cu/40Co-Al_2O_3 were Cu and Co metal. The partial cobalt oxide can be reduced to cobalt metal under catalyst pretreatment condition before reaction test (300 ºC, 3h ,1 atm under H_2 flow). Which H_2 can be generated from aqueous phase reforming of glycerol on Co metal leading to promote selectivity of 1,2-PDO. Moreover, the cobalt metal as active sites for hydrogen in hydrogenation of acetol to 1,2-PDO (114). Thus, the role of 30Cu/40Co-Al_2O_3 is bimetallic catalyst.

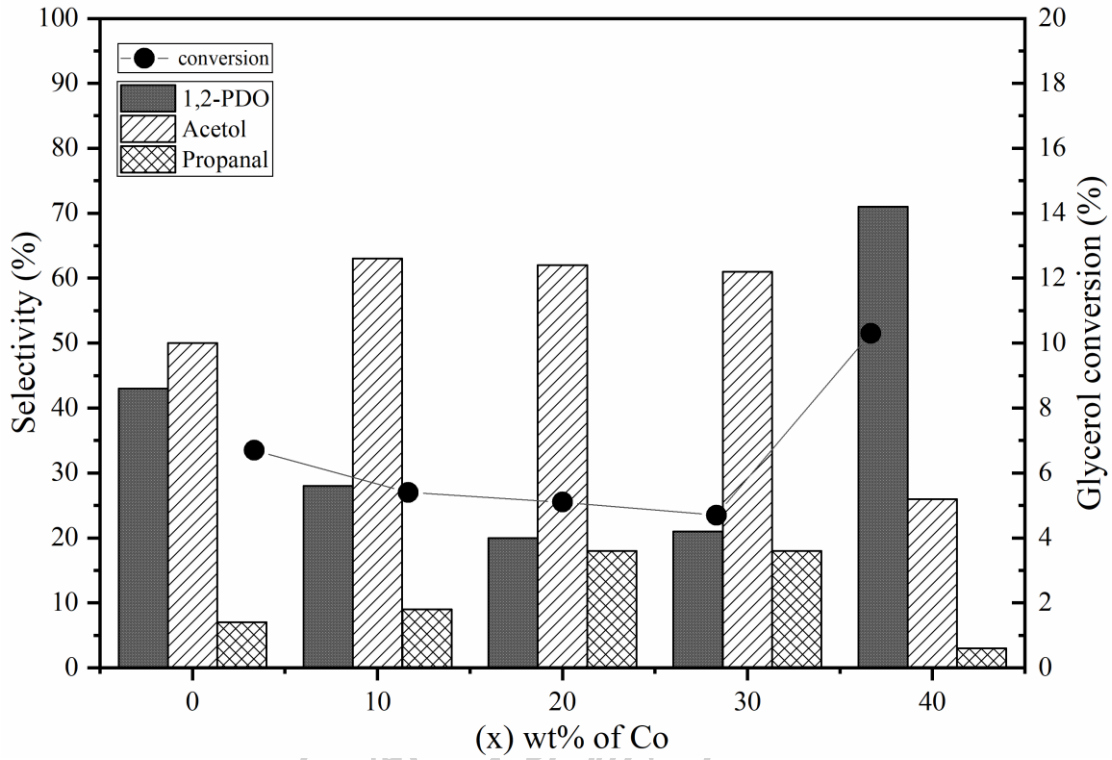

Figure 56 The activity and selectivity of the 30Cu/xCo-Al_2O_3, (x= 0, 10, 20, 30, and 40 wt% Co).

8.4 Conclusions

The Co inserting on 30Cu/Al_2O_3 catalyst during FSP method with different Co loading for glycerol hydrogenolysis reaction was investigated. When increased amount of Co on Cu/Al_2O_3 catalyst, the CuO crystallinity decreased. Addition Co on Cu/Al_2O_3 catalyst can decreased interaction between Cu and Al_2O_3 because the impregnated Cu interact with Co on Al_2O_3 surface that weak interaction than Cu with Al_2O_3, leading to increasing of reducibility and active site. The Co loading of 10 to 30 wt% Co showed poor glycerol conversion and selectivity of 1,2-PDO. While the Co loading of 40 wt% on catalyst showed the highest catalytic performance, because of the increased metal active site for acetol hydrogenation. Thus, the 30Cu/40Co-Al_2O_3 behave as bimetallic catalyst.

CHAPTER IX

COMPARISION OF METAL SPINEL SUPPORT ON COPPER-BASED CATALYSTS FOR GLYCEROL HYDROGENOLYSIS TO 1,2 PROPANEDIOL

The effect of the metal aluminate (MAl_2O_4, M = Cu, Zn, Fe, and Co) with different metal loading (10, 20, 30, and 40 wt% of metal) on Cu/Al_2O_3 for glycerol hydrogenolysis to 1,2-PDO were discussed in this chapter. The activity and selectivity of $30Cu/M\text{-}Al_2O_3$, (M= Cu, Zn, Fe, and Co) with different amounts of metal loading (10-40 wt% of M) were shown in Figure 57-60. For inserting a low amount of metal, the glycerol conversion hardly changed. The inserting of 10 wt% of Cu on $30Cu/Al_2O_3$ ($30Cu/10Cu\text{-}Al_2O_3$) catalyst exhibited the highest selectivity of 1,2-PDO (62%), the lowest selectivity of acetol (36%) and propanal (2%) when compared with the other metal as shown in Figure 57, For a high Cu inserting at 40 wt% of Cu, the acetol was mainly product and the 1,2-PDO selectivity was not detected, It was guessed that the glycerol molecules were rather adsorbed on Cu metal site than $CuAl_2O_4$ support. A low active metal sites were covered glycerol molecules or the produced acetol from glycerol dehydration reaction, there were not active site to hydrogen adsorption for hydrogenation step. While the inserting of Co at 10-30 wt% on $30Cu/Al_2O_3$ showed the lowest glycerol conversion and the lowest 1,2-PDO selectivity when compared with other metal at same content. The FSP-made Co-Al2O3 presented $CoAl_2O_4$, which high intensity of $CoAl_2O_4$ was observed at low Co loading. Jindou Hou et al. reported that the appearance of Al^{3+} locating on octahedral Co-Al spinel structure showed a strong Lewis acid site for NH_3 adsorption (125). It speculated that a high acid surface on catalyst prompted acetol production. For the inserting of Zn and Fe on Cu/Al_2O_3. The product distribution was rather similar. Which the 30 wt% of metal showed the highest selectivity of 1,2-PDO in both metals. In this case, the presence of $ZnAl_2O_4$ and $FeAl_2O_4$ on catalyst inhibited glycerol adsorption on support but promoted glycerol adsorption on metal. The N_2O decomposition results reported that the inserted Zn and Fe increased active site and Cu dispersion of surface. Thus, there was enough active sites for dehydration and

hydrogenation step. When 40 wt% of metal was added on $30Cu/Al_2O_3$ during FSP process. The $30Cu/40Co\text{-}Al_2O_3$ catalyst displayed the highest glycerol conversion and 1,2-PDO selectivity because of the increased active site for hydrogenation. The partial cobalt oxide can be reduced to Co metal under catalyst pretreatment and during reaction as a result active site increased. Therefore, the $30Cu/40Co\text{-}Al_2O_3$ behave as bimetallic catalyst.

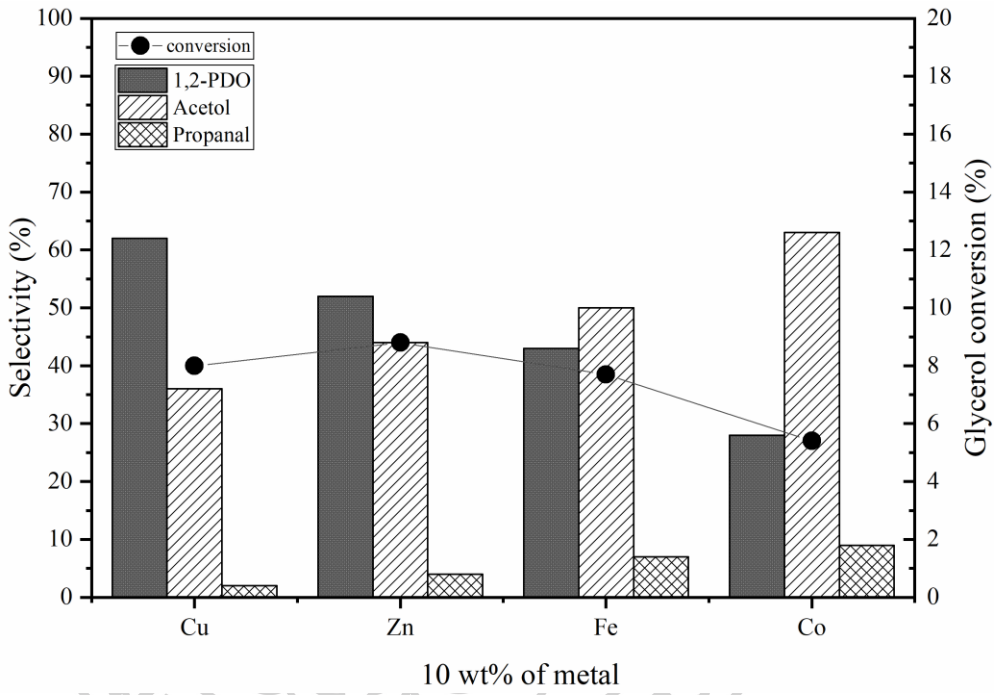

Figure 57 The activity and selectivity of $30Cu/10M\text{-}Al_2O_3$, (M= Cu, Zn, Fe and Co).

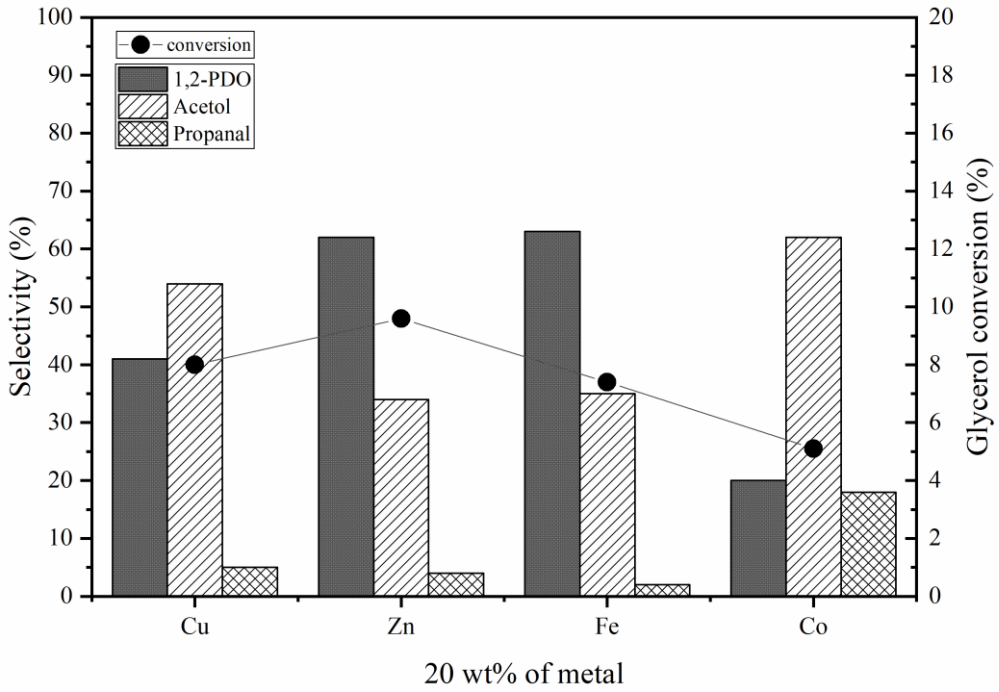

Figure 58 The activity and selectivity of 30Cu/20M-Al_2O_3, (M= Cu, Zn, Fe and Co).

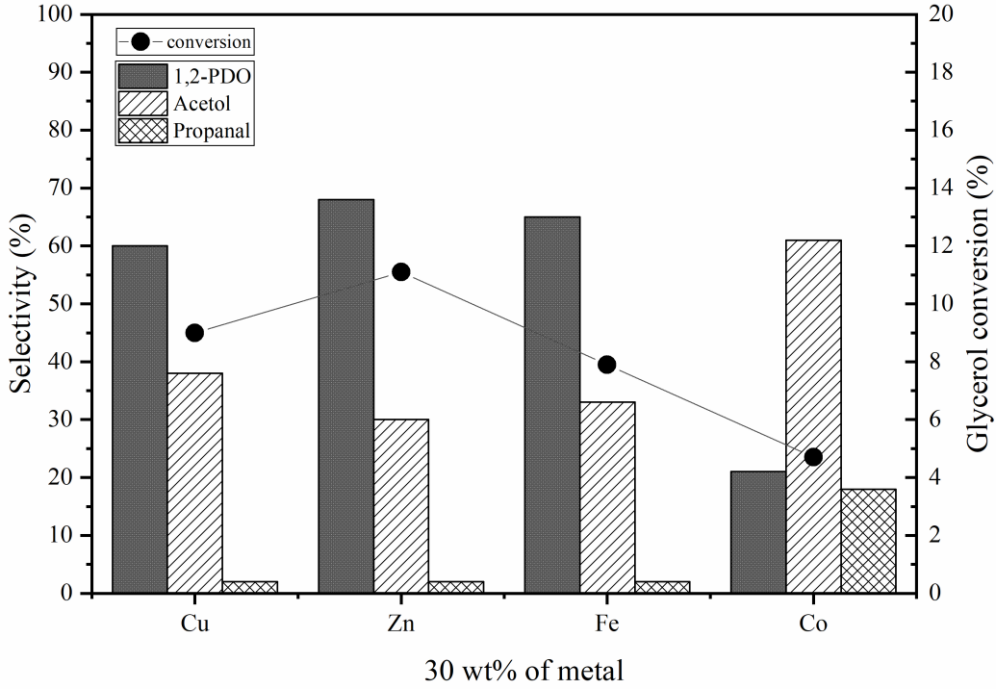

Figure 59 The activity and selectivity of 30Cu/30M-Al_2O_3, (M= Cu, Zn, Fe and Co).

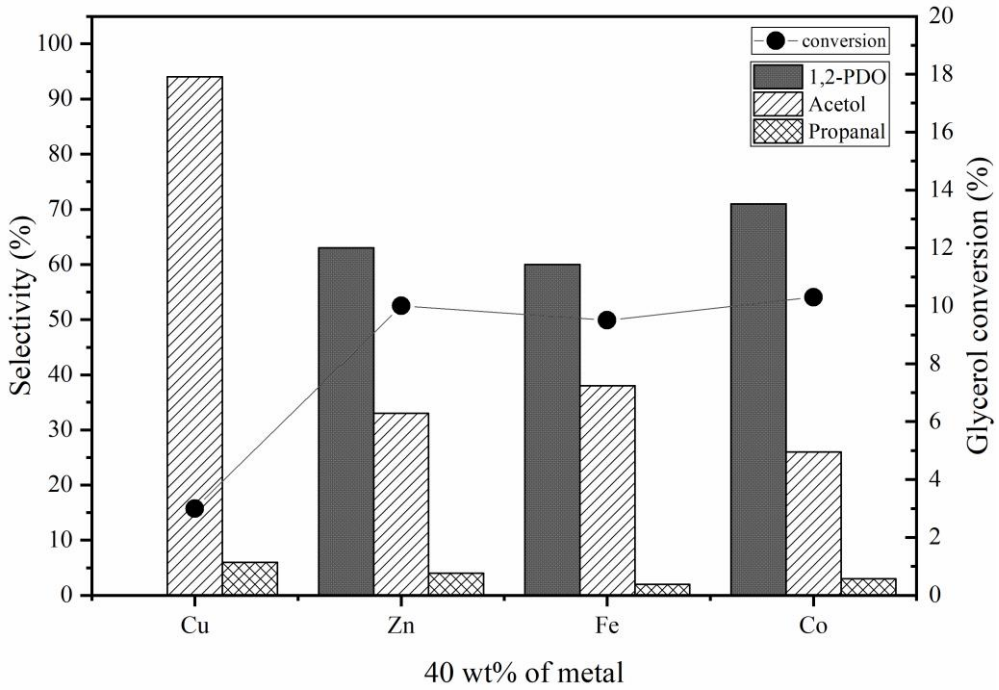

Figure 60 The activity and selectivity of 30Cu/40M-Al_2O_3, (M= Cu, Zn, Fe and Co)

CHAPTER X

SUMMARY

In this research, the type of metal aluminate spinel supports (M = Co, Zn, Fe) and amount of metal incorporated with Al_2O_3 (10 to 40 wt.% of metal) on Cu/Al_2O_3 for glycerol hydrogenolysis were investigated, the experimental conclusions were summarized as follows:

1. The optimum of metal loading with Al_2O_3 (the FSP-made $M\text{-}Al_2O_3$, M= Cu, Zn, Fe, and Co) on Cu based catalysts were the 10 wt% of Cu, 30 wt% of Zn, 30 wt% of Fe, and 40 wt.% of Co.

2. The presence of $CuAl_2O_4$, $ZnAl_2O_4$, and $FeAl_2O_4$ spinel on $30Cu/Al_2O_3$ catalyst inhibited glycerol adsorption on support but promoted adsorption of glycerol on Cu species. For $CoAl_2O_4$ phase promoted the glycerol dehydration step due to the high acidity on catalyst.

3. The FSP-made $M\text{-}Al_2O_3$ (M = Cu, Zn, Fe, and Co) on Cu based catalyst presented metal oxide and metal aluminate species. In case of Cu, Cu as a mono-active site. For Zn and Fe, metal oxide as a promoter on catalyst lead to the increased Cu dispersion and active sites. While Co participated with Cu for the utilization of active H_2 on hydrogenation that was Cu-Co bimetallic catalyst.

REFERENCES

1. Sun D, Yamada Y, Sato S. Efficient production of propylene in the catalytic conversion of glycerol. Applied Catalysis B: Environmental. 2015;174-175:13-20.
2. Rocha-Martin J, Acosta A, Berenguer J, Guisan JM, Lopez-Gallego F. Selective oxidation of glycerol to 1,3-dihydroxyacetone by covalently immobilized glycerol dehydrogenases with higher stability and lower product inhibition. Bioresour Technol. 2014;170:445-53.
3. Kumar S, Wee Y, Lee I, Jin Sun H, Zhao X, Xia S, et al. Stabilized glycerol dehydrogenase for the conversion of glycerol to dihydroxyacetone2015.
4. Ning X, Li Y, Yu H, Peng F, Wang H, Yang Y. Promoting role of bismuth and antimony on Pt catalysts for the selective oxidation of glycerol to dihydroxyacetone. Journal of Catalysis. 2016;335:95-104.
5. Namdeo A, Mahajani SM, Suresh AK. Palladium catalysed oxidation of glycerol—Effect of catalyst support. Journal of Molecular Catalysis A: Chemical. 2016;421:45-56.
6. Roncal T, Muñoz C, Lorenzo L, Maestro B, Díaz de Guereñu MdM. Two-step oxidation of glycerol to glyceric acid catalyzed by the Phanerochaete chrysosporium glyoxal oxidase. Enzyme and Microbial Technology. 2012;50(2):143-50.
7. Zhang C, Wang T, Liu X, Ding Y. Cu-promoted Pt/activated carbon catalyst for glycerol oxidation to lactic acid. Journal of Molecular Catalysis A: Chemical. 2016;424:91-7.
8. Hou M, Jiang H, Liu Y, Chen R. Role of initial water content in glycerol hydrogenolysis to 1,2-propanediol over Cu–ZnO catalyst. Reaction Kinetics, Mechanisms and Catalysis. 2017;122(2):1129-43.
9. Long W, Hao F, Xiong W, Liu P, Luo Ha. Modified sepiolite supported nickel and tungsten oxide catalysts for glycerol hydrogenolysis to 1,2-propanediol with high selectivity under mild conditions. Reaction Kinetics, Mechanisms and Catalysis. 2017;122(1):85-100.
10. Soares AVH, Salazar JB, Falcone DD, Vasconcellos FA, Davis RJ, Passos FB. A study of glycerol hydrogenolysis over Ru–Cu/Al_2O_3 and Ru–Cu/ZrO_2 catalysts. Journal of Molecular Catalysis A: Chemical. 2016;415:27-36.
11. Liu L, Ye XP. Simultaneous production of lactic acid and propylene glycol from glycerol using solid catalysts without external hydrogen. Fuel Processing Technology. 2015;137:55-65.
12. Granados-Reyes J, Salagre P, Cesteros Y. CaAl-layered double hydroxides as active catalysts for the transesterification of glycerol to glycerol carbonate. Applied Clay Science. 2016;132-133:216-22.
13. Teng WK, Ngoh GC, Yusoff R, Aroua MK. Microwave-assisted transesterification of industrial grade crude glycerol for the production of glycerol carbonate. Chemical Engineering Journal. 2016;284:469-77.
14. Ishak ZI, Sairi NA, Alias Y, Aroua MKT, Yusoff R. Production of glycerol carbonate from glycerol with aid of ionic liquid as catalyst. Chemical Engineering Journal. 2016;297:128-38.
15. Pinto BP, de Lyra JT, Nascimento JAC, Mota CJA. Ethers of glycerol and ethanol as bioadditives for biodiesel. Fuel. 2016;168:76-80.
16. Wykle RL, Snyder F. The glycerol source for the biosynthesis of alkyl glycerol ethers. Biochemical and Biophysical Research Communications. 1969;37(4):658-62.

17. Yuan Z, Xia S, Chen P, Hou Z, Zheng X. Etherification of Biodiesel-Based Glycerol with Bioethanol over Tungstophosphoric Acid To Synthesize Glyceryl Ethers. Energy & Fuels. 2011;25(7):3186-91.
18. Omata K, Matsumoto K, Murayama T, Ueda W. Direct oxidative transformation of glycerol to acrylic acid over Nb-based complex metal oxide catalysts. Catalysis Today. 2016;259:205-12.
19. Liu L, Wang B, Du Y, Zhong Z, Borgna A. Bifunctional $Mo_3VO_x/H_4SiW_{12}O_{40}/Al_2O_3$ catalysts for one-step conversion of glycerol to acrylic acid: Catalyst structural evolution and reaction pathways. Applied Catalysis B: Environmental. 2015;174-175:1-12.
20. Diallo MM, Mijoin J, Laforge S, Pouilloux Y. Preparation of Fe-BEA zeolites by isomorphous substitution for oxidehydration of glycerol to acrylic acid. Catalysis Communications. 2016;79:58-62.
21. Du Y, Wang C, Jiang H, Chen C, Chen R. Insights into deactivation mechanism of Cu–ZnO catalyst in hydrogenolysis of glycerol to 1,2-propanediol. Journal of Industrial and Engineering Chemistry. 2016;35:262-7.
22. Gandarias I, Arias PL, Requies J, Güemez MB, Fierro JLG. Hydrogenolysis of glycerol to propanediols over a Pt/ASA catalyst: The role of acid and metal sites on product selectivity and the reaction mechanism. Applied Catalysis B: Environmental. 2010;97(1):248-56.
23. Vasiliadou ES, Lemonidou AA. Parameters Affecting the Formation of 1,2-Propanediol from Glycerol over Ru/SiO_2 Catalyst. Organic Process Research & Development. 2011;15(4):925-31.
24. Wang S, Yin K, Zhang Y, Liu H. Glycerol Hydrogenolysis to Propylene Glycol and Ethylene Glycol on Zirconia Supported Noble Metal Catalysts. ACS Catalysis. 2013;3(9):2112-21.
25. Yu W, Zhao J, Ma H, Miao H, Song Q, Xu J. Aqueous hydrogenolysis of glycerol over Ni–Ce/AC catalyst: Promoting effect of Ce on catalytic performance. Applied Catalysis A: General. 2010;383(1):73-8.
26. Meher LC, Gopinath R, Naik SN, Dalai AK. Catalytic Hydrogenolysis of Glycerol to Propylene Glycol over Mixed Oxides Derived from a Hydrotalcite-Type Precursor. Industrial & Engineering Chemistry Research. 2009;48(4):1840-6.
27. Huang Z, Cui F, Kang H, Chen J, Xia C. Characterization and catalytic properties of the CuO/SiO_2 catalysts prepared by precipitation-gel method in the hydrogenolysis of glycerol to 1,2-propanediol: Effect of residual sodium. Applied Catalysis A: General. 2009;366(2):288-98.
28. Li X, Zhang B, Wu Q, Zhang C, Yu Y, Li Y, et al. A facile strategy for confining ZnPd nanoparticles into a ZnO@Al2O3 support: A stable catalyst for glycerol hydrogenolysis. Journal of Catalysis. 2016;337:284-92.
29. Salazar JB, Falcone DD, Pham HN, Datye AK, Passos FB, Davis RJ. Selective production of 1,2-propanediol by hydrogenolysis of glycerol over bimetallic Ru–Cu nanoparticles supported on TiO_2. Applied Catalysis A: General. 2014;482:137-44.
30. Miyazawa T, Kusunoki Y, Kunimori K, Tomishige K. Glycerol conversion in the aqueous solution under hydrogen over Ru/C + an ion-exchange resin and its reaction mechanism. Journal of Catalysis. 2006;240(2):213-21.

31. Vanama PK, Kumar A, Ginjupalli SR, Komandur VRC. Vapor-phase hydrogenolysis of glycerol over nanostructured Ru/MCM-41 catalysts. Catalysis Today. 2015;250:226-38.
32. Sánchez T, Salagre P, Cesteros Y, Bueno-López A. Use of delaminated hectorites as supports of copper catalysts for the hydrogenolysis of glycerol to 1,2-propanediol. Chemical Engineering Journal. 2012;179:302-11.
33. Liu C, Zhang C, Hao S, Sun S, Liu K, Xu J, et al. WOx modified Cu/Al2O3 as a high-performance catalyst for the hydrogenolysis of glucose to 1,2-propanediol. Catalysis Today. 2016;261:116-27.
34. Pandhare NN, Pudi SM, Biswas P, Sinha S. Vapor phase hydrogenolysis of glycerol to 1,2-propanediol over γ-Al_2O_3 supported copper or nickel monometallic and copper–nickel bimetallic catalysts. Journal of the Taiwan Institute of Chemical Engineers. 2016;61:90-6.
35. Zheng L, Xia S, Hou Z. Hydrogenolysis of glycerol over Cu-substituted hydrocalumite mediated catalysts. Applied Clay Science. 2015;118:68-73.
36. Huang Z, Liu H, Cui F, Zuo J, Chen J, Xia C. Effects of the precipitation agents and rare earth additives on the structure and catalytic performance in glycerol hydrogenolysis of Cu/SiO_2 catalysts prepared by precipitation-gel method. Catalysis Today. 2014;234:223-32.
37. Durán-Martín D, Granados ML, Fierro JLG, Pinel C, Mariscal R. Deactivation of CuZn Catalysts Used in Glycerol Hydrogenolysis to Obtain 1,2-Propanediol. Topics in Catalysis. 2017;60(15):1062-71.
38. Liu H, Liang S, Jiang T, Han B, Zhou Y. Hydrogenolysis of Glycerol to 1,2-Propanediol over Ru–Cu Bimetals Supported on Different Supports. CLEAN – Soil, Air, Water. 2011;40(3):318-24.
39. Dasari MA, Kiatsimkul P-P, Sutterlin WR, Suppes GJ. Low-pressure hydrogenolysis of glycerol to propylene glycol. Applied Catalysis A: General. 2005;281(1):225-31.
40. Xiao Z, Li C, Xiu J, Wang X, Williams CT, Liang C. Insights into the reaction pathways of glycerol hydrogenolysis over Cu–Cr catalysts. Journal of Molecular Catalysis A: Chemical. 2012;365:24-31.
41. Xiao Z, Ma Z, Wang X, Williams CT, Liang C. Effects of Synthetic Parameters on the Structure and Catalytic Performance of Cu−Cr Catalysts Prepared by a Non-Alkoxide Sol−Gel Route. Industrial & Engineering Chemistry Research. 2011;50(4):2031-9.
42. Kwak BK, Park DS, Yun YS, Yi J. Preparation and characterization of nanocrystalline $CuAl_2O_4$ spinel catalysts by sol–gel method for the hydrogenolysis of glycerol. Catalysis Communications. 2012;24:90-5.
43. Wolosiak-Hnat AM, Eugeniusz; Grzmil, Barbara. Influence of Parameters on Glycerol Hydrogenolysis over a Cu/Al_2O_3 Catalyst. Chemical Engineering & Technology. 2013;36(3):411-8.
44. Ragupathi C, Vijaya JJ, Kennedy LJ, Bououdina M. Nanostructured copper aluminate spinels: Synthesis, structural, optical, magnetic, and catalytic properties. Materials Science in Semiconductor Processing. 2014;24:146-56.
45. James T, Padmanabhan M, Warrier KGK, Sugunan S. $CuAl_2O_4$ formation and its effect on α-Al_2O_3 phase evolution on calcination of metal ion doped boehmite xerogels. Materials Chemistry and Physics. 2007;103(2):248-54.

46. Lv W, Liu B, Qiu Q, Wang F, Luo Z, Zhang P, et al. Synthesis, characterization and photocatalytic properties of spinel $CuAl_2O_4$ nanoparticles by a sonochemical method. Journal of Alloys and Compounds. 2009;479(1):480-3.
47. Faungnawakij K, Fukunaga T, Kikuchi R, Eguchi K. Deactivation and regeneration behaviors of copper spinel–alumina composite catalysts in steam reforming of dimethyl ether. Journal of Catalysis. 2008;256(1):37-44.
48. Hafshejani LD, Tangsir S, Koponen H, Riikonen J, Karhunen T, Tapper U, et al. Synthesis and characterization of Al_2O_3 nanoparticles by flame spray pyrolysis (FSP) — Role of Fe ions in the precursor. Powder Technology. 2016;298:42-9.
49. Høj M, Linde K, Hansen TK, Brorson M, Jensen AD, Grunwaldt J-D. Flame spray synthesis of $CoMo/Al_2O_3$ hydrotreating catalysts. Applied Catalysis A: General. 2011;397(1):201-8.
50. Strobel R, Baiker A, Pratsinis S. Aerosol flame synthesis of catalysts.457-80.
51. Mekasuwandumrong O, Phothakwanpracha S, Jongsomjit B, Shotipruk A, Panpranot J. Influence of flame conditions on the dispersion of Pd on the flame spray-derived Pd/TiO_2 nanoparticles. Powder Technology. 2011;210(3):328-31.
52. Chaisuk C, Boonpitak P, Panpranot J, Mekasuwandumrong O. Effects of Co dopants and flame conditions on the formation of Co/ZrO_2 nanoparticles by flame spray pyrolysis and their catalytic properties in CO hydrogenation. Catalysis Communications. 2011;12(10):917-22.
53. Xiao Z, Wang X, Xiu J, Wang Y, Williams CT, Liang C. Synergetic effect between Cu^0 and Cu^+ in the Cu-Cr catalysts for hydrogenolysis of glycerol. Catalysis Today. 2014;234:200-7.
54. Wang S, Liu H. Selective hydrogenolysis of glycerol to propylene glycol on Cu–ZnO catalysts. Catalysis Letters. 2007;117(1):62-7.
55. Vila F, López Granados M, Ojeda M, Fierro JLG, Mariscal R. Glycerol hydrogenolysis to 1,2-propanediol with $Cu/\gamma\text{-}Al_2O_3$: Effect of the activation process. Catalysis Today. 2012;187(1):122-8.
56. Pagliaro M. Glycerol: The Platform Biochemical of the Chemical Industry (2013): Simplicissimus; 2013.
57. Roy D, Subramaniam B, Chaudhari RV. Aqueous phase hydrogenolysis of glycerol to 1,2-propanediol without external hydrogen addition. Catalysis Today. 2010;156(1):31-7.
58. Vasiliadou ES, Lemonidou AA. Kinetic study of liquid-phase glycerol hydrogenolysis over Cu/SiO_2 catalyst. Chemical Engineering Journal. 2013;231:103-12.
59. Mane RB, Rode CV. Continuous Dehydration and Hydrogenolysis of Glycerol over Non-Chromium Copper Catalyst: Laboratory-Scale Process Studies. Organic Process Research & Development. 2012;16(5):1043-52.
60. Wang F, Dubois J-L, Ueda W. Catalytic performance of vanadium pyrophosphate oxides (VPO) in the oxidative dehydration of glycerol. Applied Catalysis A: General. 2010;376(1):25-32.
61. Yuan Z, Wang L, Wang J, Xia S, Chen P, Hou Z, et al. Hydrogenolysis of glycerol over homogenously dispersed copper on solid base catalysts. Applied Catalysis B: Environmental. 2011;101(3):431-40.

62. Balaraju M, Rekha V, Prasad PSS, Devi BLAP, Prasad RBN, Lingaiah N. Influence of solid acids as co-catalysts on glycerol hydrogenolysis to propylene glycol over Ru/C catalysts. Applied Catalysis A: General. 2009;354(1):82-7.
63. Gallegos-Suarez E, Pérez-Cadenas M, Guerrero-Ruiz A, Rodriguez-Ramos I, Arcoya A. Effect of the functional groups of carbon on the surface and catalytic properties of Ru/C catalysts for hydrogenolysis of glycerol. Applied Surface Science. 2013;287:108-16.
64. Alhanash A, Kozhevnikova EF, Kozhevnikov IV. Gas-phase dehydration of glycerol to acrolein catalysed by caesium heteropoly salt. Applied Catalysis A: General. 2010;378(1):11-8.
65. Chai S-H, Wang H-P, Liang Y, Xu B-Q. Sustainable production of acrolein: Preparation and characterization of zirconia-supported 12-tungstophosphoric acid catalyst for gas-phase dehydration of glycerol. Applied Catalysis A: General. 2009;353(2):213-22.
66. Atia H, Armbruster U, Martin A. Dehydration of glycerol in gas phase using heteropolyacid catalysts as active compounds. Journal of Catalysis. 2008;258(1):71-82.
67. Maris EP, Davis RJ. Hydrogenolysis of glycerol over carbon-supported Ru and Pt catalysts. Journal of Catalysis. 2007;249(2):328-37.
68. Sun D, Yamada Y, Sato S, Ueda W. Glycerol hydrogenolysis into useful C3 chemicals. Applied Catalysis B: Environmental. 2016;193:75-92.
69. Guo L, Zhou J, Mao J, Guo X, Zhang S. Supported Cu catalysts for the selective hydrogenolysis of glycerol to propanediols. Applied Catalysis A: General. 2009;367(1):93-8.
70. Yuan Z, Wang J, Wang L, Xie W, Chen P, Hou Z, et al. Biodiesel derived glycerol hydrogenolysis to 1,2-propanediol on Cu/MgO catalysts. Bioresour Technol. 2010;101(18):7088-92.
71. Hirunsit P, Luadthong C, Faungnawakij K. Effect of alumina hydroxylation on glycerol hydrogenolysis to 1,2-propanediol over Cu/Al_2O_3: combined experiment and DFT investigation. RSC Advances. 2015;5(15):11188-97.
72. Yun YS, Park DS, Yi J. Effect of nickel on catalytic behaviour of bimetallic Cu-Ni catalyst supported on mesoporous alumina for the hydrogenolysis of glycerol to 1,2-propanediol. Catalysis Science & Technology. 2014;4(9):3191-202.
73. Wu Z, Mao Y, Song M, Yin X, Zhang M. Cu/boehmite: A highly active catalyst for hydrogenolysis of glycerol to 1,2-propanediol. Catalysis Communications. 2013;32:52-7.
74. Tan H, Hedhill MN, Wang Y, Zhang J, Li K, Sioud S, et al. One-pot synthesis Of $Cu/ZnO/ZnAl_2O_4$ catalysts and their catalytic performance in glycerol hydrogenolysis. Catalysis Science & Technology. 2013;3(12):3360-70.
75. Durán-Martín D, Ojeda M, Granados ML, Fierro JLG, Mariscal R. Stability and regeneration of $Cu–ZrO_2$ catalysts used in glycerol hydrogenolysis to 1,2-propanediol. Catalysis Today. 2013;210:98-105.
76. Mane RB, Ghalwadkar AA, Hengne AM, Suryawanshi YR, Rode CV. Role of promoters in copper chromite catalysts for hydrogenolysis of glycerol. Catalysis Today. 2011;164(1):447-50.
77. Mueller R, Jossen R, Kammler HK, Pratsinis SE, Akhtar MK. Growth of zirconia particles made by flame spray pyrolysis. AIChE Journal. 2004;50(12):3085-94.

78. Jang HD, Chang H, Suh Y, Okuyama K. Synthesis of SiO_2 nanoparticles from sprayed droplets of tetraethylorthosilicate by the flame spray pyrolysis. Current Applied Physics. 2006;6:e110-e3.
79. Torabmostaedi H, Zhang T, Foot P, Dembele S, Fernandez C. Process control for the synthesis of ZrO_2 nanoparticles using FSP at high production rate. Powder Technology. 2013;246:419-33.
80. Ishizawa H, Sakurai O, Mizutani N, Kato M. Homogeneous Y_2O_3-Stabilized ZrO2 Powder by Spray Pyrolysis Method1986.
81. Yuan FL, Chen CH, Kelder EM, Schoonman J. Preparation of zirconia and yttria-stabilized zirconia (YSZ) fine powders by flame-assisted ultrasonic spray pyrolysis (FAUSP). Solid State Ionics. 1998;109(1):119-23.
82. Seok Lee J, Kumar P, Gupta S, Hwan Oh M, Ranade M, Singh R. Enhanced Luminescence Properties of YAG : Ce^{3+} Nanophosphor Prepared by Flame Spray Pyrolysis2010. K25-K9 p.
83. Engel SR, Koegler AF, Gao Y, Kilian D, Voigt M, Seeger T, et al. Gas phase temperature measurements in the liquid and particle regime of a flame spray pyrolysis process using O2-based pure rotational coherent anti-Stokes Raman scattering. Appl Opt. 2012;51(25):6063-75.
84. Lee S, Schneider K, Schumann J, Mogalicherla AK, Pfeifer P, Dittmeyer R. Effect of metal precursor on $Cu/ZnO/Al_2O_3$ synthesized by flame spray pyrolysis for direct DME production. Chemical Engineering Science. 2015;138:194-202.
85. Cho K, Chang H, Kil DS, Park J, Jang HD, Sohn HY. Mechanisms of the Formation of Silica Particles from Precursors with Different Volatilities by Flame Spray Pyrolysis. Aerosol Science and Technology. 2009;43(9):911-20.
86. Li Y, Shen J, Hu Y, Qiu S, Min G, Song Z, et al. General Flame Approach to Chainlike MFe_2O_4 Spinel (M = Cu, Ni, Co, Zn) Nanoaggregates for Reduction of Nitroaromatic Compounds. Industrial & Engineering Chemistry Research. 2015;54(40):9750-7.
87. Tada S, Larmier K, Büchel R, Copéret C. Methanol synthesis via CO_2 hydrogenation over $CuO–ZrO_2$ prepared by two-nozzle flame spray pyrolysis. Catalysis Science & Technology. 2018;8(8):2056-60.
88. Dreyer JAH, Grossmann HK, Chen J, Grieb T, Gong BB, Sit PHL, et al. Preferential oxidation of carbon monoxide over $Pt–FeO_x/CeO_2$ synthesized by two-nozzle flame spray pyrolysis. Journal of Catalysis. 2015;329:248-61.
89. Choi SH, Ko YN, Lee J-K, Park BK, Kang YC. Core–shell-structure $Ag–BaTiO_3$ composite nanopowders prepared directly by flame spray pyrolysis. Materials Chemistry and Physics. 2013;140(1):266-72.
90. Hembram K, Sivaprakasam D, Rao TN, Wegner K. Large-scale manufacture of ZnO nanorods by flame spray pyrolysis. Journal of Nanoparticle Research. 2013;15(2):1461.
91. Yu J, Zhang Z, Dallmann F, Zhang J, Miao D, Xu H, et al. Facile synthesis of highly active Rh/Al_2O_3 steam reforming catalysts with preformed support by flame spray pyrolysis. Applied Catalysis B: Environmental. 2016;198:171-9.
92. Pisduangdaw S, Panpranot J, Chaisuk C, Faungnawakij K, Mekasuwandumrong O. Flame sprayed tri-metallic $Pt–Sn–X/Al_2O_3$ catalysts (X = Ce, Zn, and K) for propane dehydration. Catalysis Communications. 2011;12(12):1161-5.

93. Tok A, Boey F, Zhao X. Novel Synthesis of Al_2O_3 Nano-Particles by Flame Spray Pyrolysis. Journal of Materials Processing Technology - J MATER PROCESS TECHNOL. 2006;178:270-3.
94. Volanti DP, Keyson D, Cavalcante LS, Simões AZ, Joya MR, Longo E, et al. Synthesis and characterization of CuO flower-nanostructure processing by a domestic hydrothermal microwave. Journal of Alloys and Compounds. 2008;459(1):537-42.
95. Hannemann S, Grunwaldt J-D, Lienemann P, Günther D, Krumeich F, Pratsinis SE, et al. Combination of flame synthesis and high-throughput experimentation: The preparation of alumina-supported noble metal particles and their application in the partial oxidation of methane. Applied Catalysis A: General. 2007;316(2):226-39.
96. Papp A, Molnár Á, Mastalir Á. Catalytic investigation of Pd particles supported on MCM-41 for the selective hydrogenations of terminal and internal alkynes. Applied Catalysis A: General. 2005;289(2):256-66.
97. Lira Eı, L´opez C, Oropeza F, Bartolini Mo, Alvarez J, Goldwasser M, et al. HMS mesoporous silica as cobalt support for the Fischer–TropschSynthesis: Pretreatment, cobalt loading and particle size effects. Journal of Molecular Catalysis A Chemical. 2008;281:146-53.
98. Alothman Z. A Review: Fundamental Aspects of Silicate Mesoporous Materials2012. 2874-902 p.
99. Kalderis D, Kotti M, Méndez A, Gascó G. Characterization of hydrochars produced by hydrothermal carbonization of rice husk2014.
100. Tarot M-L, Barreau M, Duprez D, Lauga V, Iojoiu E, Courtois X, et al. Influence of the Sodium Impregnation Solvent on the Deactivation of Cu/FER-Exchanged Zeolites Dedicated to the SCR of NO_x with NH_3. Catalysts. 2017;8:3.
101. Hinrichsen O, Genger T, Muhler M. Chemisorption of N_2O and H_2 for the Surface Determination of Copper Catalysts. Chemical Engineering & Technology. 2000;23(11):956-9.
102. Kant A, He Y, Jawad A, Li X, Rezaei F, Smith JD, et al. Hydrogenolysis of glycerol over Ni, Cu, Zn, and Zr supported on H-beta. Chemical Engineering Journal. 2017;317:1-8.
103. Stringhini FM, Foletto EL, Sallet D, Bertuol DA, Chiavone-Filho O, Nascimento CAOd. Synthesis of porous zinc aluminate spinel ($ZnAl_2O_4$) by metal-chitosan complexation method. Journal of Alloys and Compounds. 2014;588:305-9.
104. Mostafaei A, Zolriasatein A. Synthesis and characterization of conducting polyaniline nanocomposites containing ZnO nanorods. Progress in Natural Science: Materials International. 2012;22(4):273-80.
105. Naqvi SM. Structural and optical properties of chromium doped zinc oxide nanoparticles synthesized by sol-gel method2014.
106. Fukushima J, Hayashi Y, Takizawa H. Structure and magnetic properties of $FeAl_2O_4$ synthesized by microwave magnetic field irradiation. Journal of Asian Ceramic Societies. 2013;1(1):41-5.
107. Nilsson M, Jansson K, Jozsa P, Pettersson LJ. Catalytic properties of Pd supported on $ZnO/ZnAl_2O_4/Al_2O_3$ mixtures in dimethyl ether autothermal reforming. Applied Catalysis B: Environmental. 2009;86(1):18-26.
108. Wang C, Jiang H, Chen C, Chen R, Xing W. Solvent effect on hydrogenolysis of glycerol to 1,2-propanediol over Cu–ZnO catalyst. Chemical Engineering Journal. 2015;264:344-50.

109. Zieliński J, Zglinicka I, Znak L, Kaszkur Z. Reduction of Fe_2O_3 with hydrogen. Applied Catalysis A: General. 2010;381(1):191-6.
110. Munteanu G, Ilieva L, Andreeva D. Kinetic parameters obtained from TPR data for α-Fe_2O_3 and Au/α-Fe_2O_3 systems. Thermochimica Acta. 1997;291:171–7.
111. Tiernan M, Barnes P, Parkes G. Reduction of Iron Oxide Catalysts: The Investigation of Kinetic Parameters Using Rate Perturbation and Linear Heating Thermoanalytical Techniques. Journal of Physical Chemistry B - J PHYS CHEM B. 2000;105.
112. Akula V, Aluha J, Mogano D, Scurrell M. The gold–ruthenium–iron oxide catalytic system for the low temperature water–gas-shift reaction: The examination of gold–ruthenium interactions. Applied Catalysis A: General. 2003;245:149-58.
113. Rojanapipatkul S, Jongsomjit B. Synthesis of cobalt on cobalt-aluminate via solvothermal method and its catalytic properties for carbon monoxide hydrogenation. Catalysis Communications. 2008;10(2):232-6.
114. Yun YS, Park DS, Yi J. Effect of nickel on catalytic behaviour of bimetallic Cu–Ni catalyst supported on mesoporous alumina for the hydrogenolysis of glycerol to 1,2-propanediol. Catalysis Science & Technology. 2014;4(9):3191-202.
115. Mauriello F, Vinci A, Espro C, Gumina B, Musolino MG, Pietropaolo R. Hydrogenolysis vs. aqueous phase reforming (APR) of glycerol promoted by a heterogeneous Pd/Fe catalyst. Catalysis Science & Technology. 2015;5(9):4466-73.
116. Gröhn AJ, Pratsinis SE, Wegner K. Fluid-particle dynamics during combustion spray aerosol synthesis of ZrO_2. Chemical Engineering Journal. 2012;191:491-502.
117. Teoh W, Setiawan R, Grunwaldt J-D, Amal R, Pratsinis S. Ru-Doped Cobalt−Zirconia Nanocomposites by Flame Synthesis: Physicochemical and Catalytic Properties. Chemistry of Materials - CHEM MATER. 2008;20.
118. Jacobs G, Das TK, Zhang Y, Li J, Racoillet G, Davis BH. Fischer–Tropsch synthesis: support, loading, and promoter effects on the reducibility of cobalt catalysts. Applied Catalysis A: General. 2002;233(1):263-81.
119. Li J, Zhan X, Zhang Y, Jacobs G, Das T, Davis BH. Fischer–Tropsch synthesis: effect of water on the deactivation of Pt promoted Co/Al_2O_3 catalysts. Applied Catalysis A: General. 2002;228(1):203-12.
120. Jacobs G, Ji Y, Davis BH, Cronauer D, Kropf AJ, Marshall CL. Fischer–Tropsch synthesis: Temperature programmed EXAFS/XANES investigation of the influence of support type, cobalt loading, and noble metal promoter addition to the reduction behavior of cobalt oxide particles. Applied Catalysis A: General. 2007;333(2):177-91.
121. Mo X, Tsai Y-T, Gao J, Mao D, Goodwin JG. Effect of component interaction on the activity of Co/CuZnO for CO hydrogenation. Journal of Catalysis. 2012;285(1):208-15.
122. Jacobs G, Chaney JA, Patterson PM, Das TK, Davis BH. Fischer–Tropsch synthesis: study of the promotion of Re on the reduction property of Co/Al_2O_3 catalysts by in situ EXAFS/XANES of Co K and Re LIII edges and XPS. Applied Catalysis A: General. 2004;264(2):203-12.
123. Álvarez-Docio CM, Reinosa JJ, Del Campo A, Fernández JF. Investigation of thermal stability of 2D and 3D $CoAl_2O_4$ particles in core-shell nanostructures by Raman spectroscopy. Journal of Alloys and Compounds. 2019;779:244-54.

124. Duan X, Pan M, Yu F, Yuan D. Synthesis, structure and optical properties of CoAl2O4 spinel nanocrystals. Journal of Alloys and Compounds. 2011;509(3):1079-83.
125. Hou J, Luo W, Luo S, Lin C, Liu P, Liao X, et al. Facile synthesis of CuMAl (M = Cr, Mn, Zn, and Co) with highly dispersed Cu and tailorable surface acidity for efficient 2-methylpyrazine synthesis. RSC Advances. 2017;7(77):48662-9.

APPENDIXS

Appendix A

Calculation of crystallite size of copper oxide

The crystallite size of copper oxide calculated by broadened profile width of experimental of XRD using Scherrer equation

$$\text{Crystallite size} = \frac{(K.\lambda)}{B.\cos\theta}$$

Where , K = Crystallite-shape factor (0.9)

λ = Wavelength of X-ray, 1.5418 A° for CuKα

θ = Observed peak angle (degree)

B = X-ray diffraction broadening (radian) calculated by Warren equation

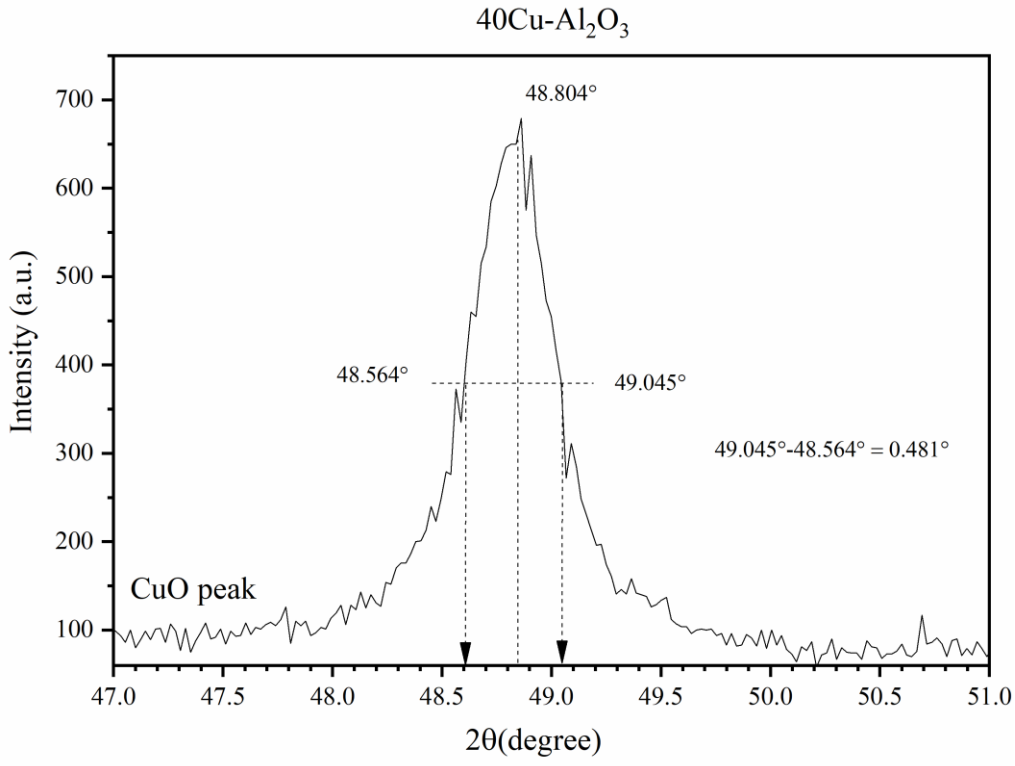

Figure 61 The half-height width of CuO at 48.804º of 40Cu-Al_2O_3 sample.

The half-height width of CuO at 48.804º = 0.481 (from Figure 57)

$= \quad 0.481 \times \frac{¶}{180}$

$= \quad 0.00839$ radian

Where, $2\theta = 48.80^{o}$

$\theta = 24.402^{o}$

$\lambda = 1.5418$ A°

Crystallite size $= \frac{(0.9. \times 1.5418)}{0.00839. \cos 24.402}$

$= \quad 181.64$ A^{o} =18.16 nm

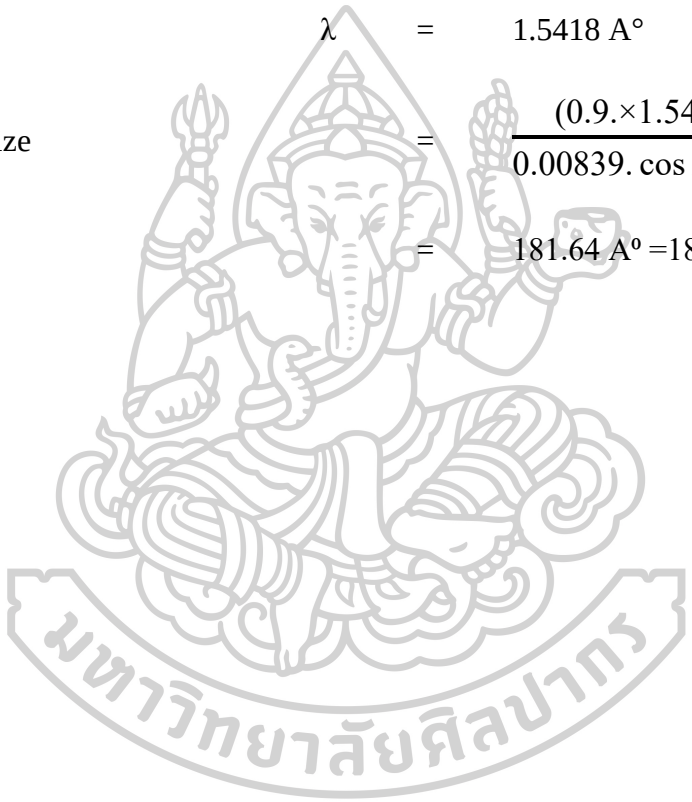

Appendix B

Calculation for N_2O chemisorption

The molecules of N_2O adsorbed on copper surface was decomposed to nitrogen and chemisorbed oxygen atom, and then the copper surface was covered with oxygen species according to reaction ($N_2O+2Cu_s \rightarrow (Cu_s - O - Cu_s) + N_2$). The Cu_s is a declarative copper surface atom and assumption adsorption stoichiometry is 2 :1 for $Cu_s : O_{ads}$. The N_2O consumption and N_2 production peak after decomposition reaction were separated by porapak Q column.

I. Calculation of volume of Active Gas Injected

$$V_{inj}(STP) = V_{sry} \times \frac{T_{std}}{T_{amb}} \times \frac{P_{amb}}{P_{std}} \times \frac{A}{100}$$

Where, V_{sry} = syringe volume injected (cm^3)

T_{amb} = ambient temperature (◦C)

T_{std} = standard temperature (273 K)

P_{amb} = ambient pressure (mmHg)

P_{std} = standard pressure (760 mmHg)

A = % active gas in gas mixture

II. Calculating volume Chemisorbed

$$V_{ads}(STP, cm^3/gm) = \frac{V_{inj}}{m} \times \sum_{i=1}^{n} \left[1 - \frac{A_i}{A_f}\right]$$

Where, V_{inj} = volume injected (cm^3)

m = mass of sample (gm)

A_i = area of peak i

A_f = area of last peak

III. Active Metal Surface Area

A_m (m^2/gm sample) =
[total number of surface area metal atoms]×[cross section area of active metal]

$$A_m \text{ (m}^2\text{/gm sample)} = \left[\left(n \times \frac{V_{ads}}{V_g}\right) \times N_A\right] \times a$$

Where n = stoichiometry factor

V_{ads} = volume adsorbed (cm^3/gm)

V_g = molar volume of the gas at STP (22414 cm^3/mol)

N_A = Avogadro's number (6.023×10^{23} molecules/mol)

a = cross -sectional area of active metal atom

มหาวิทยาลัยศิลปากร

Appendix C

ICP results

Table 14 ICP data of metal ($M\text{-}Al_2O_3$, M= Cu, Zn, Fe, and Co).

Catalysts		ICP (wt% of metal)
$Cu\text{-}Al_2O_3$	$10Cu\text{-}Al_2O_3$	11.0
	$20Cu\text{-}Al_2O_3$	19.5
	$30Cu\text{-}Al_2O_3$	32.6
	$40Cu\text{-}Al_2O_3$	42.6
$Zn\text{-}Al_2O_3$	$10Zn\text{-}Al_2O_3$	11.7
	$20Zn\text{-}Al_2O_3$	20.9
	$30Zn\text{-}Al_2O_3$	32.7
	$40Zn\text{-}Al_2O_3$	42.6
$Fe\text{-}Al_2O_3$	$10Fe\text{-}Al_2O_3$	10.7
	$20Fe\text{-}Al_2O_3$	18.1
	$30Fe\text{-}Al_2O_3$	29.3
	$40Fe\text{-}Al_2O_3$	36.4
$Co\text{-}Al_2O_3$	$10Co\text{-}Al_2O_3$	11.4
	$20Co\text{-}Al_2O_3$	19.7
	$30Co\text{-}Al_2O_3$	29.2
	$40Co\text{-}Al_2O_3$	35.6

Appendix D

Temperature Programmed reduction (TPR) results

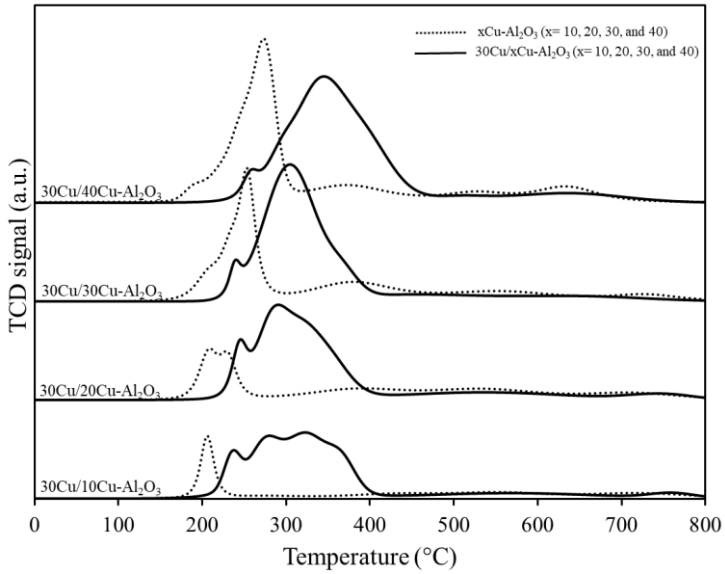

Figure 62 TPR pattern of $xCu\text{-}Al_2O_3$ and $30Cu/xCu\text{-}Al_2O_3$ (x = 10, 20, 30, and 40 wt% Cu.

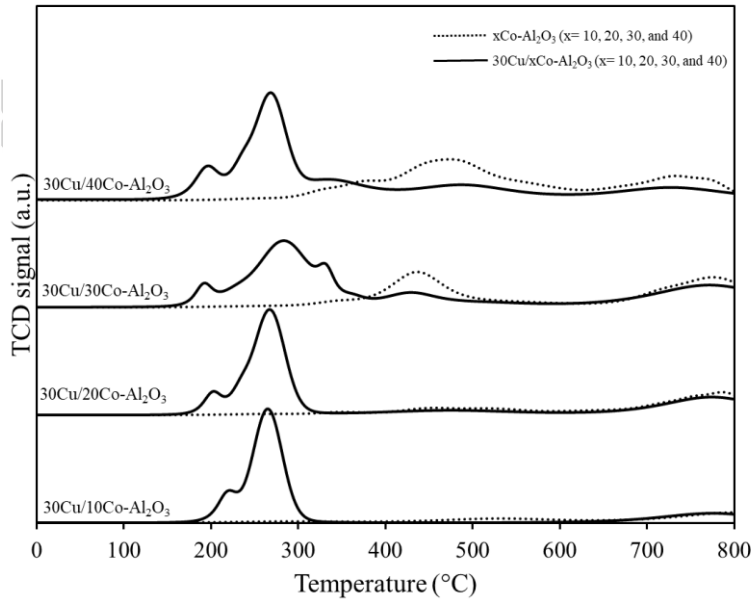

Figure 63 TPR pattern of $xCo\text{-}Al_2O_3$ and $30Cu/xCo\text{-}Al_2O_3$ (x = 10, 20, 30, and 40 wt% Co).

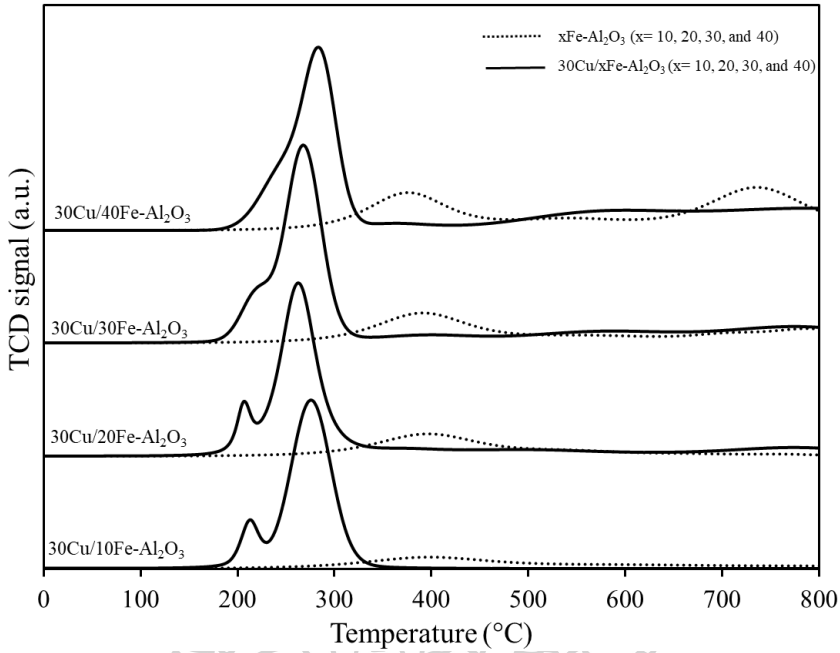

Figure 64 TPR pattern of $xFe\text{-}Al_2O_3$ and $30Cu/xFe\text{-}Al_2O_3$ (x = 10, 20, 30, and 40 wt% Fe).

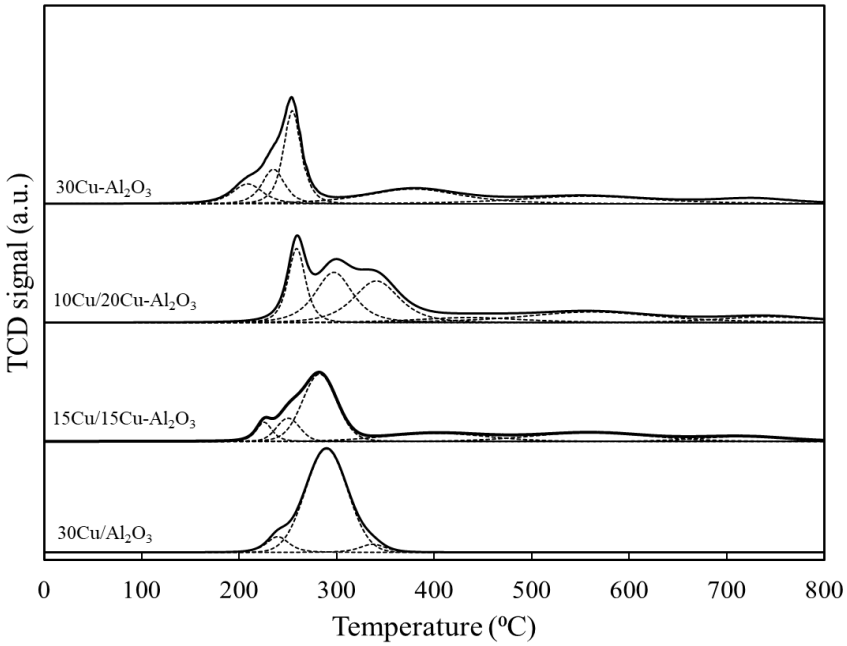

Figure 65 TPR pattern of $aCu/bCu\text{-}Al_2O_3$ catalyst (a+b = 30 wt% Cu).

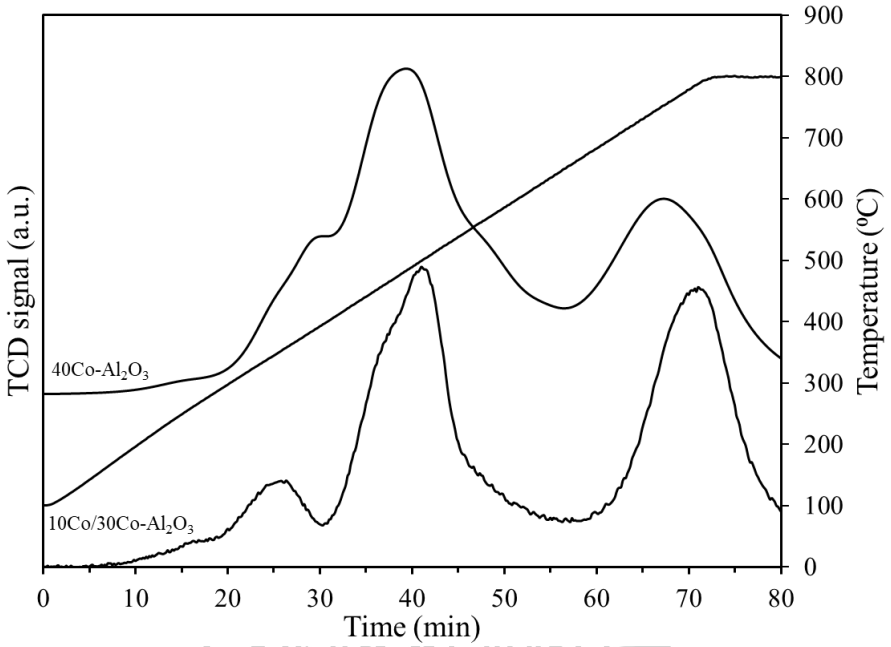

Figure 66 TPR pattern of 10Co/30Co-Al_2O_3 40Co-Al_2O_3 catalysts.

มหาวิทยาลัยศิลปากร

Appendix E

Catalytic performance for glycerol hydrogenolysis reaction

Table 15 The activity and selectivity of the 30Cu/xCu-Al_2O_3 (x = 0, 10, 20, 30, and 40 wt% Cu).

Activity	Cu (wt %)				
	0	**10**	**20**	**30**	**40**
Glycerol conversion (%)	7	8	8	9	3
Selectivity (%)					
1,2-PDO	42	62	41	60	0
Acetol	51	36	54	38	94
Propanol	7	2	5	2	6

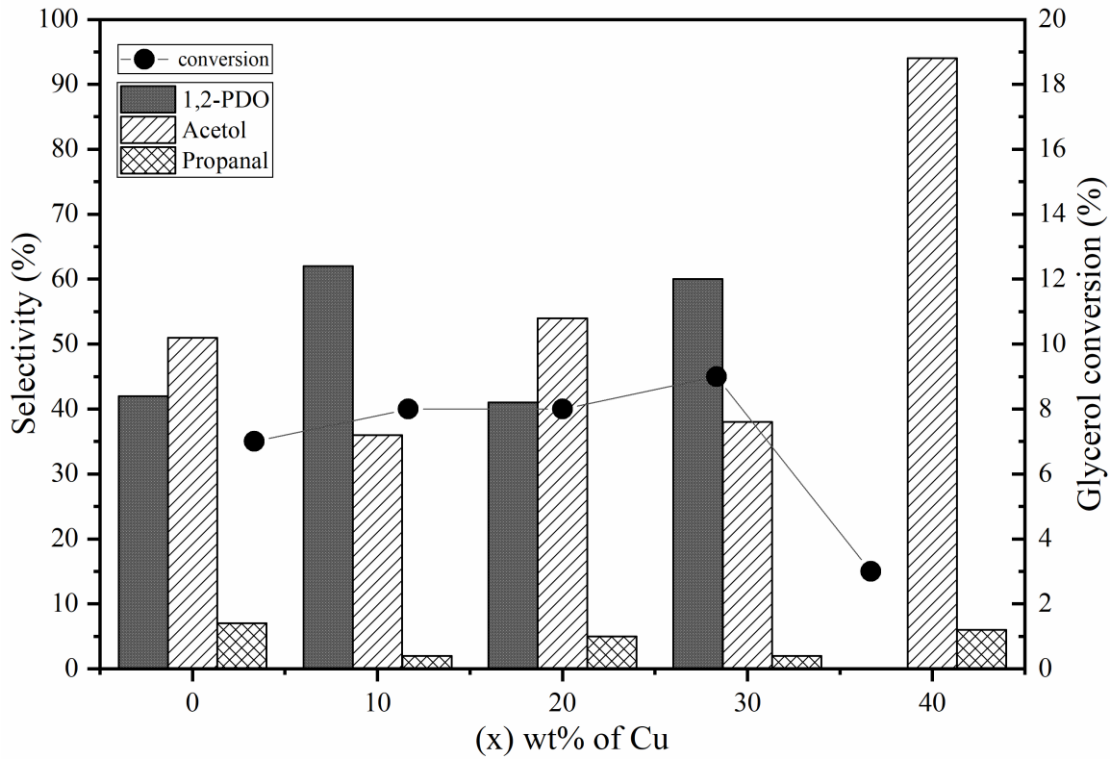

Figure 67 The activity and selectivity of the 30Cu/xCu-Al_2O_3 (x = 0, 10, 20, 30, and 40 wt% Cu).

Table 16 The activity and selectivity of the of the aCu/bCu-Al_2O_3 (a+b = 30 wt% Cu) catalyst.

Activity	Catalysts			
	30Cu/Al_2O_3	**15Cu/15Cu-Al_2O_3**	**10Cu/20Cu-Al_2O_3**	**30Cu-Al_2O_3**
Glycerol conversion (%)	7	6	8	10
Selectivity (%)				
1,2-PDO	42	20	35	37
Acetol	51	76	62	61
Propanol	7	4	3	2

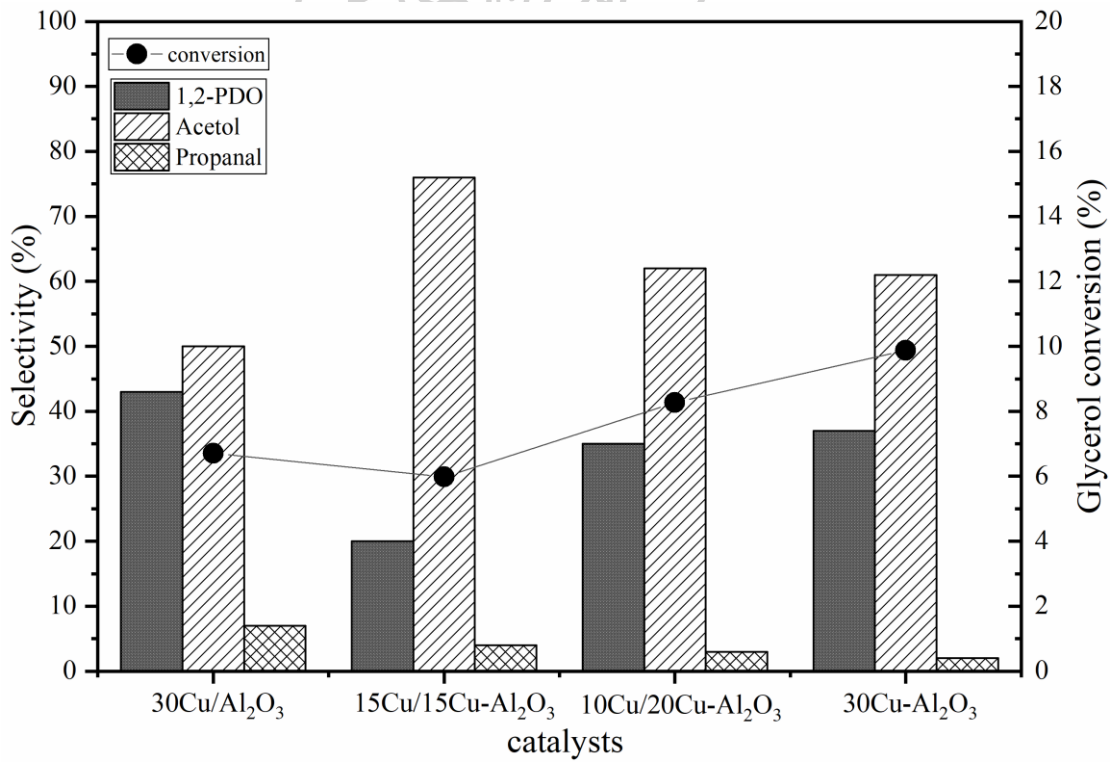

Figure 68 The activity and selectivity of the aCu/bCu-Al_2O_3 (a+b = 30 wt% Cu) catalyst.

Table 17 The activity and selectivity of the of the 30Cu/Al_2O_3 catalyst with different reaction time.

Activity	Time (h)			
	3	**6**	**9**	**12**
Glycerol conversion (%)	7	8	10	12
Selectivity (%)				
1,2-PDO	42	45	55	52
Acetol	51	45	33	30
Propanol	7	10	12	18

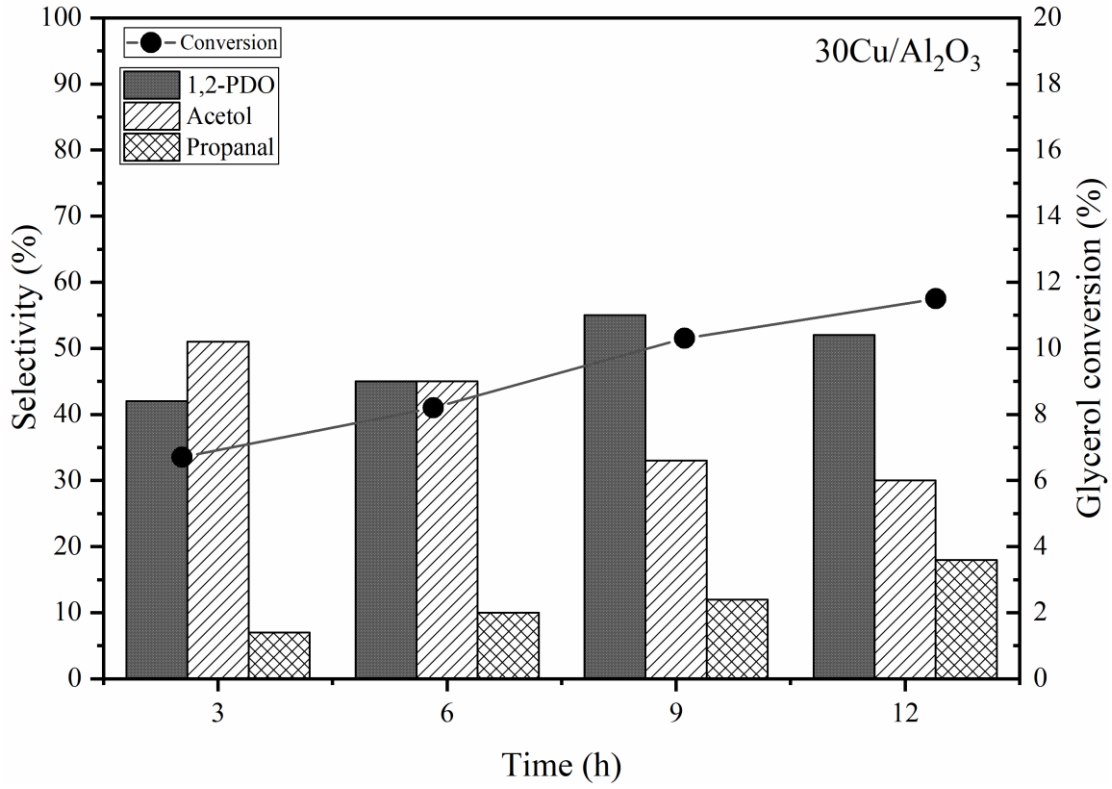

Figure 69 The activity and selectivity of the 30Cu/Al_2O_3 catalyst with different reaction time.

Table 18 The activity and selectivity of the 30Cu/xZn-Al_2O_3 (x = 0, 10, 20, 30, and 40 wt% Zn).

Activity	**Zn (wt %)**				
	0	**10**	**20**	**30**	**40**
Glycerol conversion (%)	7	9	10	11	10
Selectivity (%)					
1,2-PDO	42	52	62	68	63
Acetol	51	44	34	30	33
Propanol	7	4	4	2	4

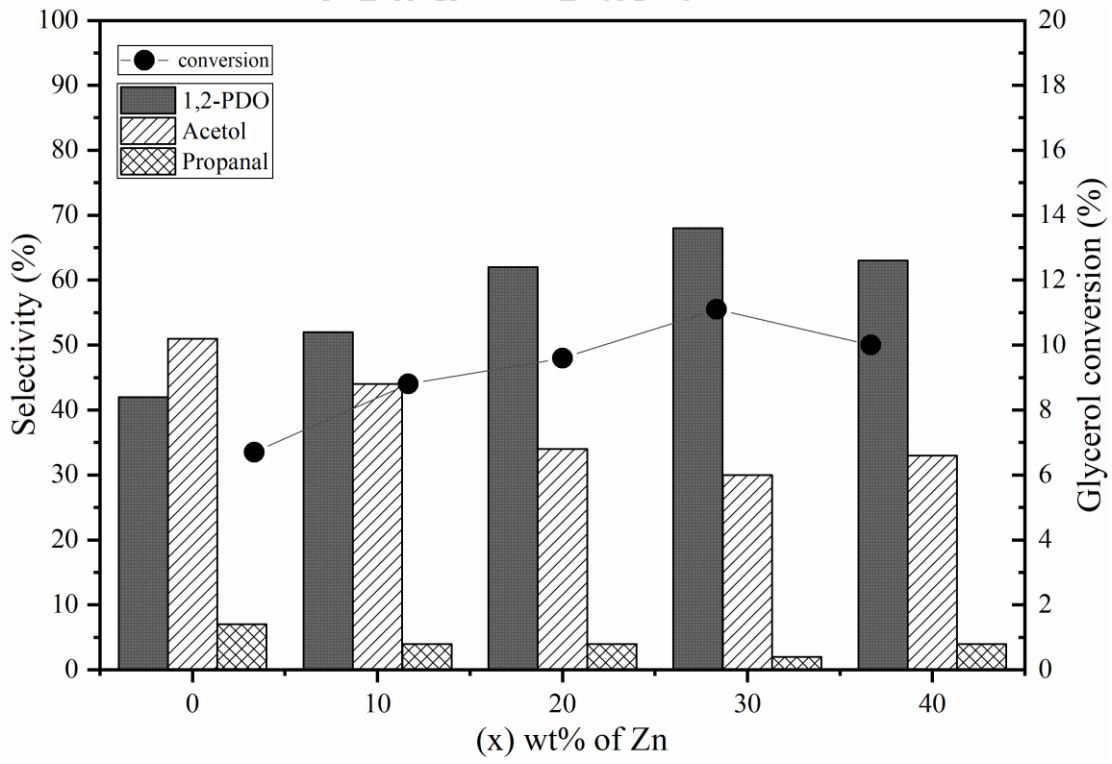

Figure 70 The activity and selectivity of the 30Cu/xZn-Al_2O_3 (x = 0, 10, 20, 30, and 40 wt% Zn).

Table 19 The activity and selectivity of the 30Cu/30Zn-Al_2O_3 with different reaction time.

Activity	**Time (h)**				
	1	**3**	**3**	**7**	**9**
Glycerol conversion (%)	7	11	12	13	13
Selectivity (%)					
1,2-PDO	62	68	66	71	71
Acetol	38	30	31	27	25
Propanol	0	2	3	2	4

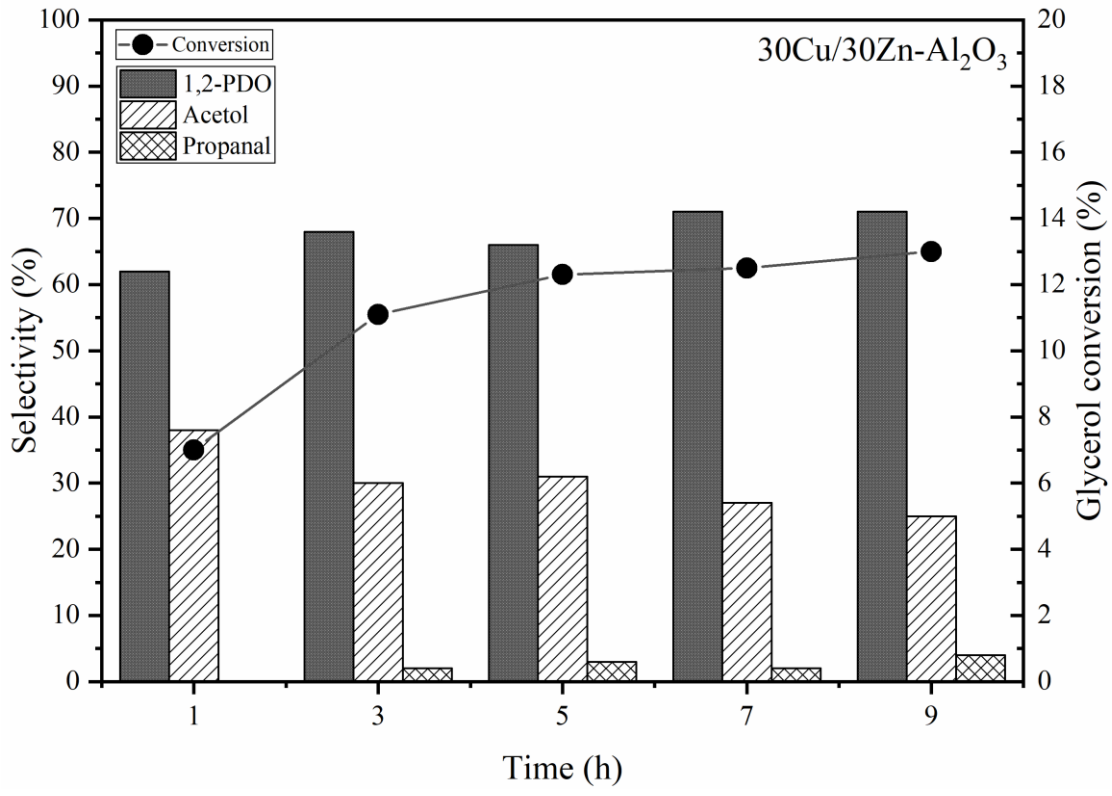

Figure 71 The activity and selectivity of the 30Cu/30Zn-Al_2O_3 with different reaction time.

Table 20 The activity and selectivity of the 30Cu/xFe-Al_2O_3 (x = 0, 10, 20, 30, and 40 wt% Fe).

Activity	**Fe (wt %)**				
	0	**10**	**20**	**30**	**40**
Glycerol conversion (%)	7	8	7	8	10
Selectivity (%)					
1,2-PDO	42	43	63	65	60
Acetol	51	50	35	33	38
Propanol	7	7	2	2	2

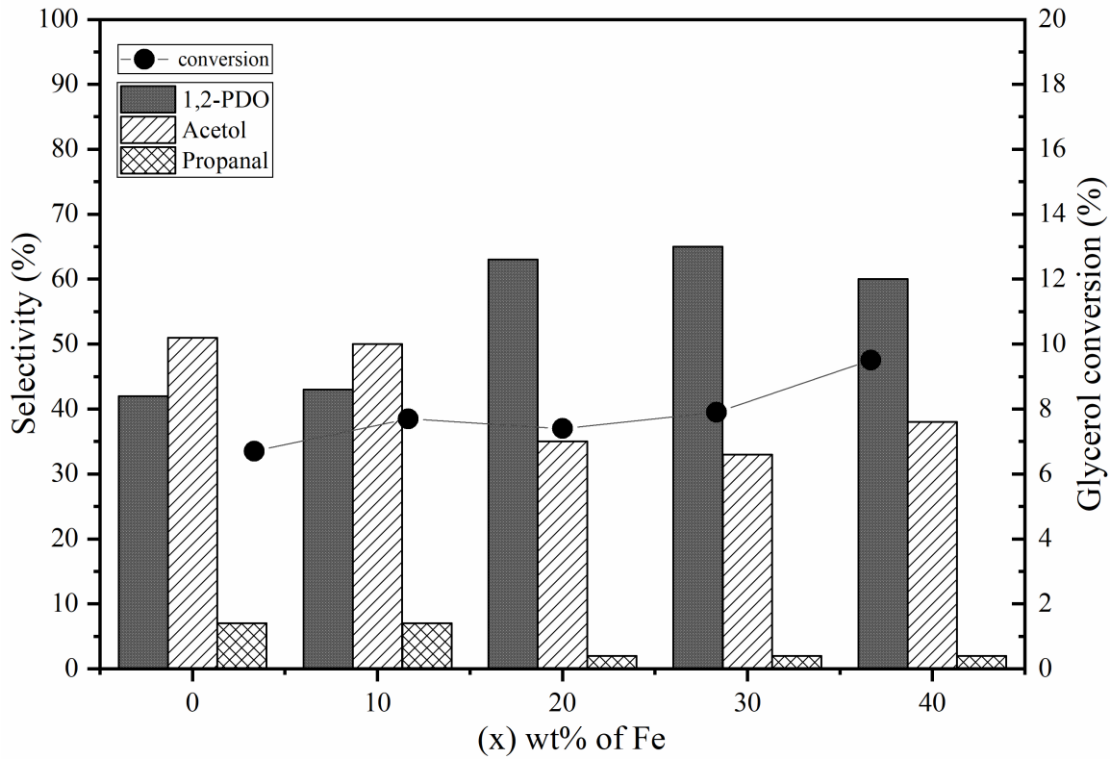

Figure 72 The activity and selectivity of the 30Cu/xFe-Al_2O_3 (x = 0, 10, 20, 30, and 40 wt% Fe).

Table 21 The activity and selectivity of the 30Cu/xCo-Al_2O_3 (x = 0, 10, 20, 30, and 40 wt% Co).

Activity	**Co (wt %)**				
	0	**10**	**20**	**30**	**40**
Glycerol conversion (%)	7	5	5	5	10
Selectivity (%)					
1,2-PDO	42	28	20	21	71
Acetol	51	63	62	61	26
Propanol	7	9	18	18	3

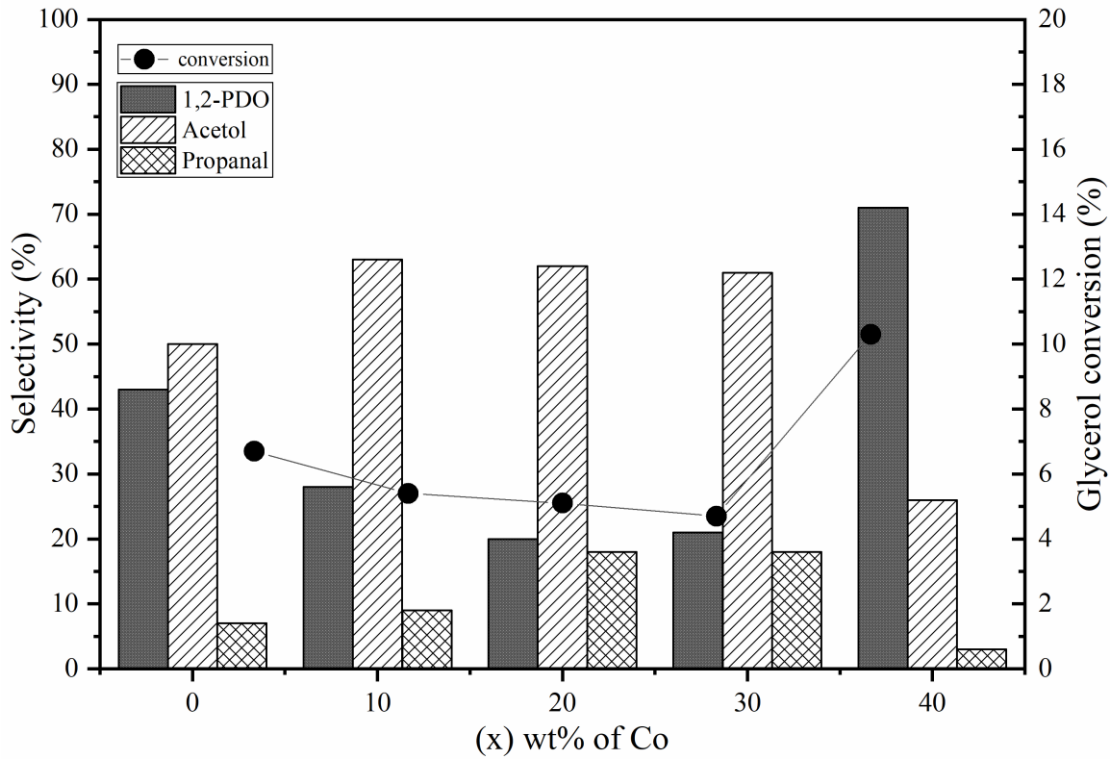

Figure 73 The activity and selectivity of the 30Cu/xCo-Al_2O_3 (x = 0, 10, 20, 30, and 40 wt% Co).

Table 22 The activity and selectivity of the 40Co-Al_2O_3 and 10Co/30Co-Al_2O_3 catalysts.

Activity	**Catalysts**	
	40Co-Al_2O_3	**10Co/30Co-Al_2O_3**
Glycerol conversion (%)	5	9
Selectivity (%)		
1,2-PDO	35	51
Acetol	58	45
Propanol	7	4

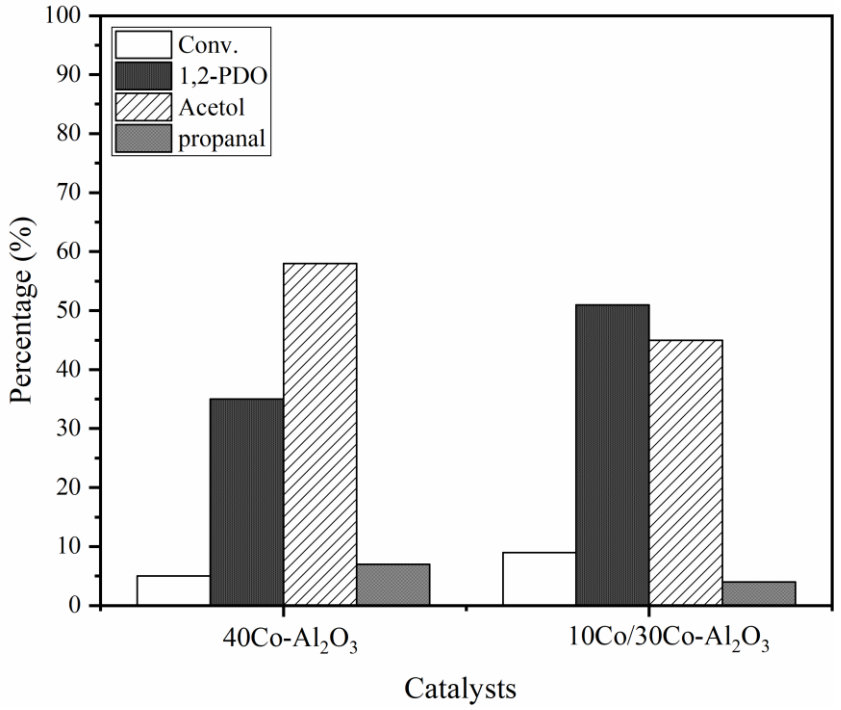

Figure 74 The activity and selectivity of the 40Co-Al_2O_3 and 10Co/30Co-Al_2O_3 catalysts.

VITA

NAME	Charuwan
DATE OF BIRTH	17 November 1987
PLACE OF BIRTH	Nakhon Pathom
INSTITUTIONS ATTENDED	Department of Chemical Engineering, Silpakorn University, B. Eng. Department of Chemical Engineering, Silpakorn University, M. Eng.
HOME ADDRESS	25/3 M.3 T. Wangtaku A.Meung , Nakhon Pathom 73000